# In-beam $\gamma$-ray spectroscopy of two-step fragmentation reactions at relativistic energies — The case of $^{36}$Ca

Inaugural-Dissertation
zur
Erlangung des Doktorgrades
der Mathematisch-Naturwissenschaftlichen Fakultät
der Universität zu Köln

vorgelegt von
Pieter Doornenbal
aus Groß-Gerau

Köln, 2007

| | |
|---|---|
| Berichterstatter: | Prof. Dr. Peter Reiter<br>Prof. Dr. Jan Jolie |
| Tag der mündlichen Prüfung: | 23.10.2007 |

# Abstract

A two-step fragmentation experiment has been performed at GSI with the RISING setup. It combines the fragment separator FRS, which allows for the production of radioactive heavy ions at relativistic energies, with a high resolution $\gamma$-spectrometer. This combination offers unique possibilities for nuclear structure investigations like the test of shell model predictions far from stability. Within the present work the question if the $N = 14(16)$ shell stabilisation in $Z = 8$ oxygen isotopes and the $N = 20$ shell quenching in $^{32}$Mg are symmetric with respect to the isospin projection quantum number $T_z$ has been addressed.
New $\gamma$-ray decays were found in the neutron deficient $^{36}$Ca and $^{36}$K by impinging a radioactive ion beam of $^{37}$Ca on a secondary $^{9}$Be target. The fragmentation products were selected with the calorimeter telescope CATE and the emitted $\gamma$-rays were measured with Ge Cluster, MINIBALL, and BaF$_2$ HECTOR detectors.
For $^{36}$Ca the $2_1^+ \rightarrow 0_{g.s.}^+$ transition energy was determined to be 3015(16) keV, which is the heaviest $T = 2$ nucleus from which $\gamma$-spectroscopic information has been obtained so far. A comparison between the experimental $2_1^+$ energies of $^{36}$Ca and its mirror nucleus $^{36}$S yielded a mirror energy difference of $\Delta E_M = -276(16)$ keV.
In order to understand the large $\Delta E_M$ value, the experimental single-particle energies from the $A = 17$, $T = 1/2$ mirror nuclei were taken and applied onto modified isospin symmetric USD interactions in shell model calculations. These calculations were in agreement with the experimental result and showed that the experimental single-particle energies may account empirically for the one body part of Thomas-Ehrman and/or Coulomb effects.
A method to extract the lifetime of excited states in fragmentation reactions was investigated. Therefore, the dependence between the lifetime of an excited state and the average de-excitation velocity and trajectory of the nuclei in relativistic fragmentation experiments has been studied. Known lifetime values in $^{34}$Cl could be confirmed and new values were found for $^{36}$K.

# Kurzzusammenfassung

Ein zweistufiges Fragmentationsexperiment wurde an der GSI mit dem RISING-Aufbau durchgeführt. Dieser Aufbau verbindet den Fragment-Separator FRS zur Herstellung von instabilen, relativistischen Schwerionen mit einem hochauflösenden $\gamma$-Spektrometer und bietet daher einzigartige Möglichkeiten, die Struktur exotischer Kerne z.B. im Rahmen des Schalenmodells zu studieren. In dieser Arbeit wurde die Frage, ob die Stabilisierung der Schale bei $N = 14(16)$ für $Z = 8$ Sauerstoff-Isotope und das Verschwinden des $N = 20$ Schalenabschlusses in $^{32}$Mg unterhalb der $Z = 14, 16$ Unterschalen in Bezug auf die z-Komponente $T_z$ der Isospin-Quantenzahl $T$ symmetrisch sind, untersucht.

Neue $\gamma$-Zerfälle konnten in den neutronenarmen $^{36}$Ca und $^{36}$K gefunden werden, indem ein radioaktiver $^{37}$Ca Strahl auf ein sekundäres $^{9}$Be Target traf. Die dabei auftretenden Fragmentationsprodukte wurden mit dem Kalorimeter-Teleskop CATE identifiziert, während $\gamma$-Strahlen mit Ge-Cluster-, Ge-MINIBALL- und BaF$_2$-HECTOR-Detektoren gemessen wurden.

Im Falle von $^{36}$Ca wurde die $2_1^+ \rightarrow 0_{g.s.}^+$ Übergangsenergie auf 3015(16) keV bestimmt. Dies ist der schwerste $T = 2$ Kern, von dem bislang $\gamma$-spektroskopische Informationen gewonnen werden konnten. Ein Vergleich der experimentellen $2_1^+$ Energien von $^{36}$Ca und seinem Spiegelkern $^{36}$S ergab einen Wert von $\Delta E_M = -276(16)$ keV für die Spiegelkern-Energiedifferenz $\Delta E_M$.

Um diesen großen $\Delta E_M$-Wert zu verstehen, wurden die experimentellen Einteilchenenergien der $A = 17$, $T = 1/2$ Spiegelkerne herangezogen und in Schalenmodellrechnungen auf modifizierte isospin-symmetrische USD-Wechselwirkungen angewendet. Diese Rechnungen stimmten mit dem experimentellen Befund eines großen $\Delta E_M$-Wertes überein und zeigten, dass die experimentellen Einteilchenenergien empirisch durch Thomas-Ehrman- und/oder Coulomb-Effekte erklärt werden können.

Eine Methode zur Bestimmung von Lebensdauern angeregter Kernzustände in Fragmentationsreaktionen wurde untersucht. Dazu wurde die Abhängigkeit zwischen der Lebensdauer und der durchschnittlichen Geschwindigkeit bzw. Richtung der Schwerionen während des Zerfalls bei relativistischen Energien studiert. Bekannte Lebensdauerwerte in $^{34}$Cl konnten bestätigt werden, während in $^{36}$K neue Werte gefunden wurden.

# Contents

# List of Figures

# List of Tables

# 1 Introduction

Within the last 30 years new fundamental principles of the composition of matter have been revealed that led to the development of a standard model of particles and interactions. Within this model quarks and leptons are the fundamental building blocks of matter. Interactions between them are accomplished via bosons and field quantas. This model allows for a reduction of the numerous observed attributes of particles to a few simple structures.

Going from these smallest entities to bigger structures, matter can be described in different levels. A higher form of condensation is established by the atomic nucleus, in which a many-body system of protons and neutrons is formed via the strong interaction. But also the weak and electromagnetic interactions play a role in the atomic nucleus. Nuclei again are a building block for atoms, which in turn build molecules, solid states bodies, and so on. Each of these levels obeys its own physical laws.

For nuclear structure physics different models are applied to describe the observed phenomenons of nuclei. This is necessary because even with the exact knowledge of the underlying interaction in a nucleus the observed phenomenons cannot be calculated with todays computational limits, except for the lightest nuclei. Therefore, alternative approaches have to be made to describe the nuclei. Herein lies the importance of the different models: nuclear models result from the selection of a suitable basis that allows for the description of certain aspects of a many-body system but neglect others.

A very important and successful approach is the nuclear shell model in which the different states of a nucleus are calculated similarly as the electron levels in atomic shells, where the state of an electron depends on its different quantum numbers. At first, it seems quite surprising that this approach holds also for the nuclear shell model. In contrast to an atomic shell, where the electrons circulate in a central potential, the nucleons inside a many-body system interact with each other and form their own potential in which they are located. But it can be shown that the interaction of one nucleon with all neighbours can be approximated by a static central potential in which the nucleons move as independent particles [1]. Impacts between different nucleons can be neglected because in the ground state (g.s.) all low lying levels have to be occupied and the Pauli principle forbids the nucleons changes of quantum numbers. This is the basis of the shell model that permits to calculate energy levels for a single nucleon (or very few) in an average potential. On the basis of this model many properties of the nuclei in the ground state and low-lying excited states can be understood. Many excited states, however, can only be explained with the excitation of many nucleons of the nucleus. In these collective models the excitation of many nucleons create two mechanisms which are responsible for the existence of excited states: A vibration of the nuclear surface and a rotational motion of a statically deformed nucleus.

The advent of radioactive ion beam (RIB) facilities has given a boost on nuclear structure physics research. The RIBs give access to nuclear structure studies over a wide area of the chart of nuclides and allow for the study of nuclei with extreme proton-to-neutron ratios. This permits to investigate entirely new nuclear topics as, for example, exotic nuclear shapes, the limits of nuclear existence and the modification of shell structure, and magic numbers far from stability. But also the field of nuclear astrophysics can benefit from RIBs, as supernova explosions, neutron stars, and $\gamma$-ray bursters all involve reactions with nuclei that do not naturally occur on the earth.

A very successful method to produce RIBs is the In-Flight Separation (IFS) technique. A combination of magnetic, electric fields and atomic processes is used to separate the ions of interest from other isotopes produced in the reaction (projectile fragmentation or induced fission) before they are either stopped or striking on a secondary target. The former case enables isomeric and $\beta$-delayed $\gamma$-ray spectroscopy, while the latter utilises Coulomb excitation or secondary fragmentation and transfer reactions at intermediate and relativistic energies for in-beam $\gamma$-ray spectroscopy [2, 3].

Within the present work the question if the $N = 14(16)$ shell stabilisation in $Z = 8$ oxygen isotopes and the $N = 20$ shell quenching in $^{32}$Mg are symmetric with respect to the isospin projection quantum number $T_z$ has been addressed. Therefore, an experiment that aimed for the measurement of excited states at the proton-dripline, especially the $2^+_1 \rightarrow 0^+_{g.s.}$ decay in $^{36}$Ca, was performed with the RISING setup [4] at GSI. RISING combines the fragment separator FRS [5], which utilises the IFS technique, with a $\gamma$-ray detector array of high efficiency and energy resolution.

In-beam $\gamma$-ray spectroscopy with unstable secondary ion beams is an experimental challenge due to the low beam intensity, which is typically five to seven orders of magnitude lower than stable beam currents. At relativistic beam energies this technique is applicable only at the GSI accelerator facility and started with high resolution Ge detectors recently in 2003 with the new RISING detector array. Gamma-ray detection is hampered by large Doppler effects and background caused by electromagnetic background radiation and unwanted nuclear interactions. Special precautions have to be taken into consideration besides the $\gamma$-ray detection. The reaction channels need to be unambiguously identified. At the secondary target both the incoming and outgoing particles have to be measured in mass $A$ and charge $Z$ and their trajectory determined. A detailed description of the particle separation and identification before the secondary target with the FRS and after the secondary target with the calorimeter telescope CATE [6] is given in Ch. 3. The $\gamma$-ray detector array is described in Ch. 4 and includes simulations of the array's performance under different experimental conditions. The results of the performed in-beam $\gamma$-ray spectroscopy experiment are presented in Ch. 5 and discussed in Ch. 6 within the framework of shell model calculations. Ch. 7 presents the possibilities to measure lifetimes of excited states in fragmentation reactions. But before drawing the attention to these topics, a detailed motivation for $\gamma$-spectroscopic studies of $^{36}$Ca is given in the next chapter.

# 2 Motivation

The existence of a nuclear shell structure was not predicted by theoretical considerations. Instead, experimental evidence for shell closures analogue to noble gas configurations in atomic physics motivated in the 1940s the phenomenological potentials [7, 8, 9, 10, 11, 12] that could reproduce the experimental evidence. The essential difference to atomic structure is caused by the absence of a dominating central potential that is given by the charge of the protons. In nuclear physics the potential is instead exclusively generated by the nucleon-nucleon (*NN*) interaction. This interaction is governed by the strong force and, neglecting the Coulomb force, the proton and neutron are regarded as two states of the same particle, the nucleon. This assumption is the basis of the isospin formalism, which distinguishes the nucleons by the isospin projection quantum number $T_z$. In nuclear structure physics the isospin projection quantum number is given by $T_z = -1/2$ for a proton and $T_z = +1/2$ for a neutron. $T_z$ is the z-component of the total isospin $T$. For a nucleus with $A$ nucleons the $T_z$ values add algebraically, while the $T$ values are deduced from the isospin vectors of the individual nucleons:

$$T_z = \sum_{i=1}^{A} T_{z_i} \text{ and } \vec{T} = \sum_{i=1}^{A} \vec{T}_i. \tag{2.1}$$

Nuclei with the proton and neutron number interchanged are called mirror nuclei. Due to the charge symmetry in nuclear forces mirror nuclei are expected to have almost identical nuclear properties. Small differences originate from the isospin symmetry breaking Coulomb force.

The most significant experimental evidence for nuclear shell structure is the existence of magic numbers. If the number of protons or neutrons match the magic number, the nucleus is particularly stable. To be more precise, magic nuclei are characterised by (i) a high total binding energy (*BE*), (ii) a high energy necessary to remove a single nucleon, (iii) high energies of low-lying excited states, and (iv) a higher number of stable isotopes (isotones) with the same proton (neutron) magic number in comparison to neighbouring elements or isotones in the Segré chart. The lower magic numbers are symmetric in proton and neutron numbers, namely for nucleon numbers $N_n = 2$, 8, 20, 28, 50, and 82. The magic number 126 has been identified only for neutrons. Theoretically, additional magic numbers are predicted for the heaviest nuclei at 114 for protons and 184 for neutrons. These numbers are waiting to be confirmed experimentally in the research field of superheavy elements [13]. Nuclei are called doubly magic if the neutron and the proton nucleon number are both magic. The experimental observables for shell structure are now discussed in detail.

## 2.1 Experimental Signatures for Shell Structure

### 2.1.1 Binding Energies

Nuclear separation energies, defined as $S_n(Z,N) = BE(Z,N) - BE(Z,N-1)$ for neutrons and accordingly for protons ($S_p$), show discontinuities for nucleon numbers matching the magic numbers, as illustrated in Fig. 2.1 for neutrons. The second separation energy difference

$$\delta_{2n}(Z,N) = S_{2n}(Z,N+2) - S_{2n}(Z,N), \tag{2.2}$$

calculated from the binding energies

$$S_{2n}(Z,N) = BE(Z,N) - BE(Z,N-2) \tag{2.3}$$

and accordingly $\delta_{2p}$ and $S_{2p}$ mark the most sensitive and direct signature for (sub)shell closures and thus shell model behaviour [14]. Therefore, $\delta_{2n}$ and $\delta_{2p}$ show a distinct peak for closed shell nuclei, its height being proportional to the shell gap. However, a basic change of the underlying nuclear structure, as quadrupole or octupole correlations, can severely distort $\delta$ because the binding energies of three nuclei are involved in Eq. 2.2.

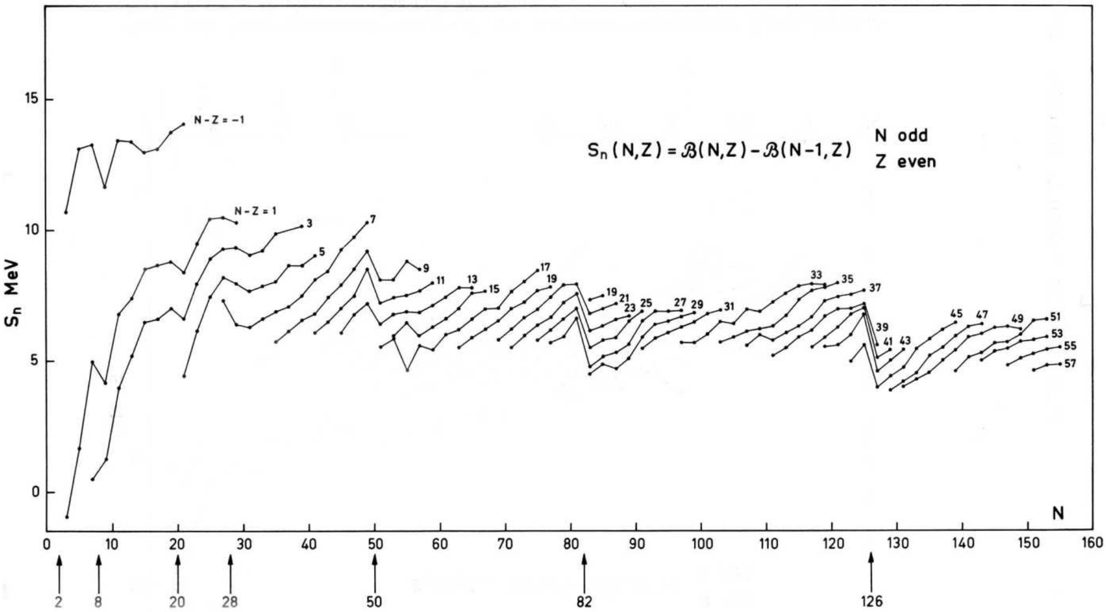

**Figure 2.1:** The neutron separation energies $S_n$ as a function of the neutron number. The figure is taken from Ref. [1].

### 2.1.2 Excitation Energies of Even-Even Nuclei

The energy required to excite the nuclear ground state of a nucleus is a very sensitive measure of its stability. Considering the pairing effect, all even-even nuclei have a vanishing total angular momentum and an even parity in the ground state ($I^{\pi} = 0^{+}$), and generally a first excited state of $I^{\pi} = 2^{+}$. For nuclei with the proton and neutron numbers $6 \leq N,Z \leq 22$ the energy values of the $I^{\pi} = 2^{+}$ states are displayed in Fig. 2.2. It is clearly visible that the excitation energies exhibit dramatic maxima when the nuclei are doubly magic. This becomes immediately evident, considering that a lot of energy is necessary to overcome large shell gaps in order to form particle-hole (p-h) states with the superior shell. Furthermore, it has to be noted that the $2_1^+$ energies gradually decrease with increasing nuclear mass number $A$, which can be ascribed to the increase of nuclear size.

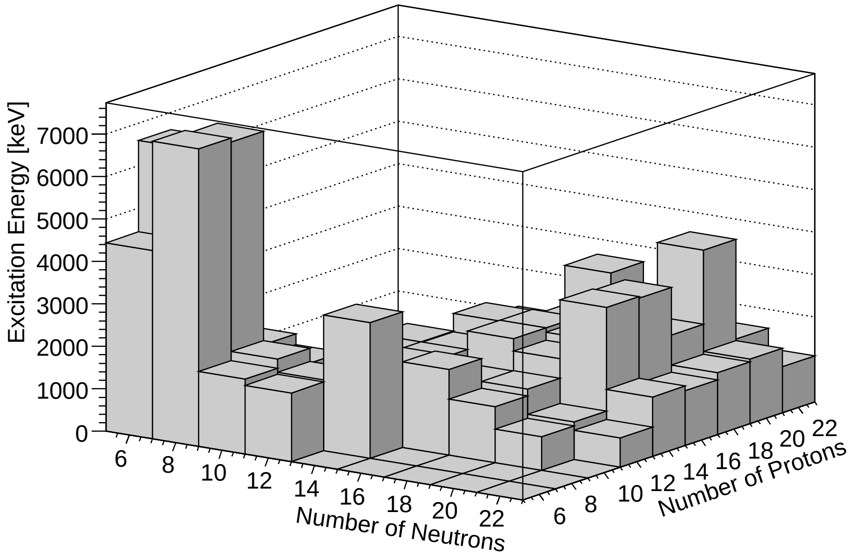

**Figure 2.2:** Excitation energies of $2_1^+$ states for even-even nuclei between $6 \leq N, Z \leq 22$. The data are taken from Ref. [15, 16].

### 2.1.3 Transition Rates of Excited Nuclei

Excited states have a lifetime $\tau$ and decay exponentially. Thus, the number of nuclei $N$ remaining in the excited state is a function of the time $t$:

$$N = N_0 e^{-t/\tau}, \tag{2.4}$$

where $N_0$ is the number of initially excited nuclei. The half-life $T_{1/2}$ is defined as the time for which half of the excited states decayed: $N = N_0/2$. With $e^{-t/\tau} = 1/2 \rightarrow t/\tau = \ln 2$ this leads to $T_{1/2} = \tau \ln 2$.

The transition rate between the initial state $|i\rangle$ and the final state $|f\rangle$ can be calculated in perturbation theory from Fermi's *Golden Rule* [17]:

$$w_{f \leftarrow i} = \frac{2\pi}{\hbar} |\langle f | H_{int} | i \rangle|^2 \rho_f \tag{2.5}$$

where $H_{int}$ is an operator of the time dependent interaction and $\rho_f$ the density of the final states. Introducing the notation $T_{fi}(\lambda l)$ for the transition rate of the type $\lambda$, where $\lambda$ can either be $E$ for electric or $M$ for magnetic transitions, the above equation can be transformed for the transition rate of photons into [17]:

$$T_{fi}(\lambda l) = \frac{8\pi(l+1)}{l((2l+1)!!)^2} \frac{k^{2l+1}}{\hbar} |\langle f|\hat{\Omega}_{l\mu}(\lambda)|i\rangle|^2, \tag{2.6}$$

where $\hat{\Omega}_{l\mu}(\lambda)$ is a generalised multipole transition operator and $k = E_\gamma/\hbar c$.

The projections $m$ of the nuclear angular momenta only matter if experiments with polarised beams and/or targets are performed. Thus, the transition rates have to be averaged over the initial projection $m_i$ and summed over the final projection $m_f$. This is done by the utilisation of reduced matrix elements which are defined as [17]:

$$B(\lambda l, I_i \rightarrow I_f) = \frac{1}{2I_i+1} \sum_{m_i,m_f} |\langle f|\hat{\Omega}_{l\mu}(\lambda)|i\rangle|^2, \tag{2.7}$$

and yields for the reduced transition probability:

$$B(\lambda l, I_i \rightarrow I_f) = \frac{1}{2I_i+1} |\langle f||\hat{\Omega}_{l}(\lambda)||i\rangle|^2. \tag{2.8}$$

The final transition rate for the emission of a photon then becomes [17]:

$$T_{fi}(\lambda l) = \frac{8\pi(l+1)}{l((2l+1)!!)^2} \frac{k^{2l+1}}{\hbar} B(\lambda l, I_i \rightarrow I_f). \tag{2.9}$$

Very often the reduced transition probabilities are related to an estimation of the excitation strength of a single nucleon [18]. These estimations are given in Weisskopf units [W.u.] and are defined as:

$$B_{W.u.}(El) = \frac{1}{4\pi} \left(\frac{3}{l+3}\right)^2 R^{2L} e^2 \; [\mathrm{e}^2\mathrm{fm}^{2l}] \tag{2.10}$$

and

$$B_{W.u.}(Ml) = \frac{10}{\pi} \left(\frac{3}{l+3}\right)^2 R^{2l-2} \mu_N^2 \; [\mu_N^2 \mathrm{fm}^{2l-2}], \tag{2.11}$$

with the nuclear mean radius $R = 1.2 \cdot A^{-1/3}$ fm, the elementary charge $e$ and the nuclear magneton $\mu_N$. Because it was assumed that only a single nucleon participated in the transition, large experimental $B(\lambda l, I_i \rightarrow I_f)$ values compared to the Weisskopf estimation indicate a collective nature of the transition.

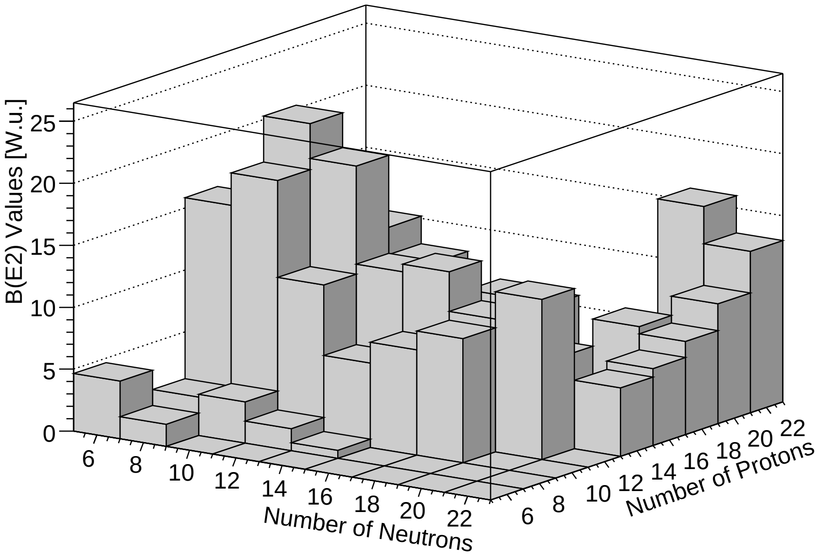

**Figure 2.3:** B($E2$) values [W.u.] of $2_1^+$ states for even-even nuclei between $6 \leq N, Z \leq 22$. The data are taken from Ref. [15].

For even-even nuclei the B($E2; 2_1^+ \rightarrow 0_{g.s.}^+$) value is of particular interest. They are displayed in Fig. 2.3 for the region $6 \leq N, Z \leq 22$. Here, the systematics are inverse to the $2_1^+$ energies. Along the magic numbers the transition probabilities are reduced, signifying that only very few nucleons are involved in the $2_1^+$ excitation.

## 2.2 The Nuclear Shell Model

The nuclear shell model is based on the Schrödinger equation for single-particle states:

$$H\psi_i(r) = \varepsilon_i \psi_i(r) \tag{2.12}$$

$$\left(-\frac{\hbar^2}{2m}\nabla^2 + V(r)\right)\psi_i(r) = \varepsilon_i \psi_i(r), \tag{2.13}$$

with a given effective potential $V(r)$. The form of the potential has to reflect the experimental evidence that the density within a heavy nucleus is nearly constant and reaches rapidly zero beyond the surface [19]. Nuclear potentials used for the shell model are (i) the Woods-Saxon potential [20] and (ii) the potential of the harmonic oscillator (HO). The Woods-Saxon potential has the form:

$$V(r) = -\frac{V_0}{1+e^{r-R/a}}, \tag{2.14}$$

with typical parameters $V_0 \approx 50$ MeV for the potential depth, a radius of $R = r_0\ A^{1/3}$, $r_0 = 1.2$ fm, and a surface thickness of $a \approx 0.5$ fm. The harmonic oscillator potential has the form:

$$V(r) = \frac{1}{2} m\omega^2 r^2, \tag{2.15}$$

with the typical parameter $\hbar\omega \approx 41\ A^{-1/3}$ MeV. The latter potential has the advantage of analytical wavefunctions. With these two potentials the lower magic numbers up to $N_n = 20$ can be reproduced, as seen on the left side of Fig. 2.4, but the higher numbers are not reproduced. In Fig. 2.4 the levels of the harmonic oscillator potential are indicated by the total oscillator quantum number $N_{HO}$ and the parity $\pi = (-1)^{N_{HO}}$ (odd for negative parity and even for positive parity). For the Woods-Saxon potential the orbits are labelled by the radial quantum number $n_r$ and the orbital angular momentum quantum number $l$.

It was the great merit of M. Goeppert-Mayer [10] and independent of her O. Haxel, J.H.D. Jensen, and H.E. Suess [9] to reproduce all of the observed magic numbers by adding a relatively strong spin-orbit (SO) term of the form $C(r)\vec{l}\cdot\vec{s}$ to the nuclear potential, where $\vec{s}$ is the intrinsic spin of the nucleons. With the total angular momentum $\vec{j} = \vec{l} + \vec{s}$ the following splitting is obtained for $\vec{l}\cdot\vec{s}$:

$$\begin{aligned} \vec{l}\cdot\vec{s} &= \frac{1}{2}(\vec{j}^2 - \vec{l}^2 - \vec{s}^2) = \frac{1}{2}\Big(j(j+1) - l(l+1) - \frac{3}{4}\Big) && (2.16)\\ &= \frac{1}{2} l \text{ for } j = l + \frac{1}{2} && (2.17)\\ &= -\frac{1}{2}(l+1) \text{ for } j = l - \frac{1}{2}. && (2.18) \end{aligned}$$

An often used form of $C(r)$ is the derivative of the average $U(r)$ potential. Hence, $C(r)$ can be expressed as:

$$C(r) = V_{ls} \cdot r_0^2 \cdot \frac{1}{r}\frac{\partial U(r)}{\partial r}, \tag{2.19}$$

where the strength of the spin-orbit potential is given by the constant $V_{ls}$. For the energy splitting $\Delta E$ between states of $j = l + 1/2$ and $j = l - 1/2$ one obtains $\Delta E \sim l + (l+1) =$

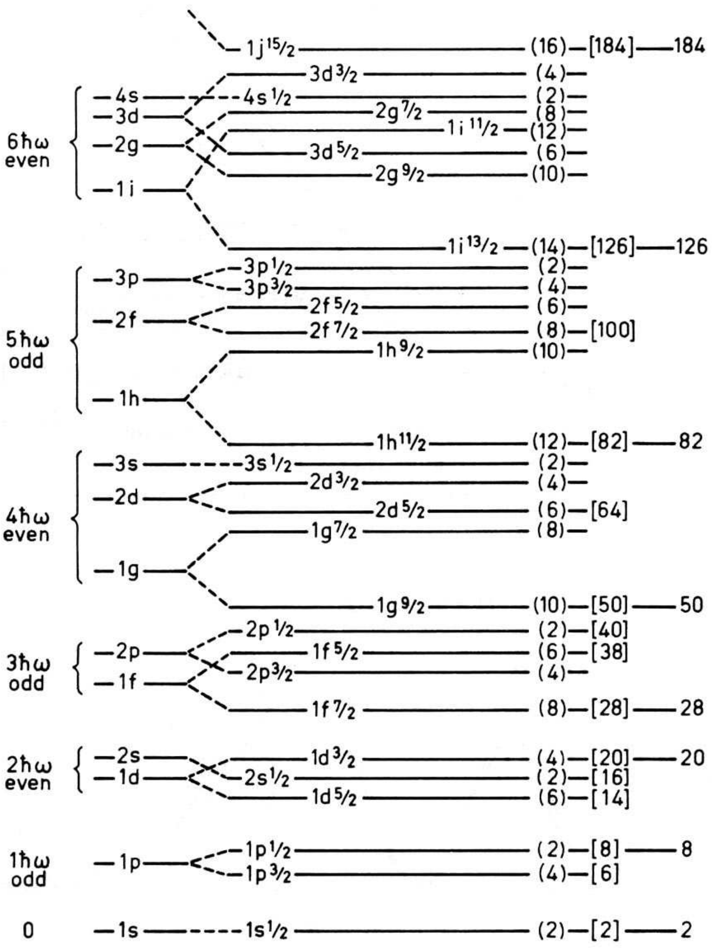

**Figure 2.4:** Sequence of one-particle orbits in the shell model for a simple harmonic oscillator (far left), a Wood-Saxon potential without (left), and with a spin-orbit splitting (middle). The numbers on the right are the nucleon numbers corresponding to the completion of a major shell. The radial quantum number $n_r$ in the figure counts the node at $r = 0$ and is therefore different from the convention used elsewhere in the present work ($1s_{1/2}$ for the lowest level compared to $0s_{1/2}$). The figure is taken from Ref. [10].

$2l + 1$. Hence, the spin-orbit splitting increases with angular momentum $l$. As shown in the middle of Fig. 2.4, the spin-orbit splitting reorders the levels and different gaps emerge. The degeneracy of each orbit $(2j + 1)$, referred to as sub-shell, is given in parenthesis. In the brackets the total nucleon number obtained by summing all lower levels is shown. Finally, the nucleon numbers for the completion of a major shell, i.e. a group of sub-shell lying close in energy, are given on the far right. It must be pointed out that the figure is only of schematic quality. Due to the Coulomb force the ordering for neutrons and protons is slightly different and also changes as a function of nuclear size.

Experimental results have shown that also two-body and three-body forces have to be considered in the theoretical framework of the nuclear shell model. If one limits the interaction to be two-body, the Hamiltonian can be expressed as a sum of kinetic energy ($T$) and potential energy ($V$) given by:

$$H = T + V = \sum_{i=1}^{A} \frac{\vec{p}_i^{\,2}}{2m_i} + \sum_{i>k=1}^{A} V_{ik}(\vec{r}_i - \vec{r}_k). \tag{2.20}$$

To solve this Hamiltonian a common one-body nucleon potential $U_i$ is introduced that splits the Hamiltonian into the independent particle Hamiltonian $H_0$ and the residual interaction Hamiltonian $H_{res}$:

$$\begin{aligned} H &= \sum_{i=1}^{A} \left[ \frac{\vec{p}_i^{\,2}}{2m_i} + U_i(\vec{r}) \right] + \sum_{i>k=1}^{A} V_{ik}(\vec{r}_i - \vec{r}_k) - \sum_{i=1}^{A} U_i(\vec{r}) && (2.21) \\ H &= H_0 + H_{res}. && (2.22) \end{aligned}$$

The idea behind this notation is to find a potential $U(r)$ that approximates the effects of the two-body interactions of Eq. 2.20 so that $H_{res}$ is a small perturbation for a system of nearly independent nucleons orbiting in a common mean field potential described by $H_0$. The solutions of the Schrödinger equation with $H_0$ are the nucleon single-particle energies (SPE) in a central potential.

For a configuration of two particles in the orbitals $j_1$ and $j_2$ coupling to the total angular momentum $J$ the residual interaction $V_{12}$ between the two particles induces an energy shift of:

$$\Delta E(j_1, j_2; J) = \langle j_1, j_2; JM | V_{12} | j_1, j_2; JM \rangle. \tag{2.23}$$

Thus, the residual interaction splits the energy degeneracy in $J$ for the $(j_1, j_2; J)$ multiplet of states. Including orbital scatterings the residual interaction Hamiltonian $H_{res}$ can be represented as a matrix, which contains such two-body matrix elements (TBME) in the form $\langle j_1, j_2 | V | j_3, j_4 \rangle_{JT}$ for a scalar interaction $V$ and all possible combinations of $j_i$ coupling to the total angular momentum $J$. The TBME are further distinguished for isospin $T = 0$ and $T = 1$ cases.

For most cases in stable nuclei it is expected that the large energy separations between different blocks of orbits given by the magic numbers remain valid with the residual interaction. Hence, for a given nucleus the orbits are filled according to the one-body nucleon potential and only the higher filled orbitals and the empty orbitals just above are affected by the residual interaction.

The study of the effects of the residual interaction is subject to very elaborate and extensive numerical nuclear shell model calculations [21, 22]. Due to computational restrictions these calculations cannot take into account all orbitals and the single-particle orbits have to be divided into three parts, which is also called the vertical truncation:

- Inert core. These orbits are always fully occupied.
- Valence space. These orbits are available to valence particles. The orbits are occupied according to the residual interaction and are the model space of a shell model calculation.
- External space. Not considered higher lying orbits that are never occupied.

Within a model space the occupation number of a given set of particles can be restricted (horizontal truncation) or restrictions according to the importance of the configuration can be applied [22, 23].

The basic inputs to most shell model calculations are the SPE and the TBME of the residual interaction. Several possibilities exist to obtain the SPE. The first option is to extract the SPE from an empirical globally adjusted central potential of e.g. Woods-Saxon, harmonic oscillator or folded Yukawa [24] type. Alternatively, the SPE are extracted from the experimental single particle (hole) states in the neighbouring nuclei of a doubly closed shell ($CS$) nucleus

$$\varepsilon_{j_i} = BE(CS \pm 1; I = j) - BE(CS; g.s.), \tag{2.24}$$

where $I$ is the total angular momentum of a nuclear state. For small model spaces it is also possible to apply a $\chi^2$ fit to determine the SPE from experimental binding and excitation energies belonging to the model space.

A $\chi^2$ fit to experimental data can also be applied to determine the TBME of the residual interaction. Such fits may take the renormalised G matrix [25] based upon modern $NN$ interactions [26] as a starting point to calculate the wave functions and energies for all energy levels under consideration. Because the energy eigenvalues $E_{J_i^\pi}$ of the Schrödinger equation for the residual Hamiltonian $H_{res}$ are functions of the SPE and TBME:

$$H_{res}\Psi_{J_i^\pi} = E_{J_i^\pi}\Psi_{J_i^\pi}, \tag{2.25}$$

the SPE and TBME can be adjusted in an iterative procedure until a convergence in the $E_{J_i^\pi}$ relative to the corresponding experimental values is achieved.

The *sd* shell contains the nuclei between $^{16}$O and $^{40}$Ca with $8 \leq N, Z \leq 20$. For this model space the SPE ($0d_{5/2}$, $1s_{1/2}$, and $0d_{3/2}$) and the TBME ($\langle j_1, j_2|V|j_3, j_4\rangle_{JT}$ with $j_i \in (0d_{5/2}, 1s_{1/2}, 0d_{3/2})$) were obtained by applying such an iterative fit, yielding the isospin symmetric USD interaction [27].

### 2.2.1 Shell Structure of Exotic *sd* Shell Nuclei

In the past the theoretical research on the shell model concentrated predominantly on nuclei in the vicinity of the line of $\beta$-stability. In these nuclei the magic numbers are established and the nuclear shell structure is well understood by using the Woods-Saxon potential including a spin-orbit splitting. For future investigations, employing spectroscopic informations on radioactive nuclei, the burning question will be: Are the magic numbers valid also for very exotic nuclei which will come within experimental reach or will new magic numbers appear?

The first example of dramatic changes in the structure of shell model nuclei was observed in the *sd* shell by going from stable to neutron rich nuclei close to the drip-line. In nine nuclei forming the "island of inversion" extra binding energy is gained by the deformation associated with particle hole-excitations across the $N = 20$ shell gap [28]. Additional experimental evidence was found for example in $^{32}$Mg in terms of a low-lying $2_1^+$ level [29] and a large B($E2; 0_{g.s}^+ \rightarrow 2_1^+$) value [30, 31, 32].

A second case is the neutron rich $^{22}$O. Here, the first excited $2^+$ state was measured to be 3199(8) keV [33, 34]. This high excitation energy is almost twice as high as the $2_1^+$ states in the adjacent $N = 10, 12$ nuclei, indicating the presence of a $N = 14$ (sub)shell closure. This observation is again supported by the measured B($E2; 0_{g.s}^+ \rightarrow 2_1^+$) value deduced from an intermediate energy Coulomb excitation experiment [34]. In $^{24}$O no $\gamma$-ray decaying states could be observed [35]. This nonobservation of any $\gamma$-ray transition provides evidence for a high lying $2_1^+$ state above the neutron separation energy of $S_n = 3.7(4)$ MeV [15] and is another indication for a new (sub)shell closure of $N = 16$ nuclei far from stability.

In the shell model calculations performed by Utsuno *et al.* [36] the experimental $2_1^+$ levels and the $\mathrm{B}(E2; 0_{g.s}^+ \rightarrow 2_1^+)$ values in the vicinity of $^{32}$Mg have been reproduced using the *sd* shell as well as the $0f_{7/2}$ and $1p_{3/2}$ orbitals as model space. Furthermore, the evolution of so-called effective single particles energies (ESPE) was investigated along the chain of $N = 20$ isotones. The ESPE are defined for an occupied orbit as the separation energy of this orbit and for an unoccupied as the gain in binding energy by putting a nucleon into this orbit. The ESPE are evaluated from the monopole part of the residual interaction, which is defined as [36, 37]:

$$V_{j_1 j_2}^T = \frac{\sum_J (2J+1)\langle j_1, j_2 | V | j_1, j_2 \rangle_{JT}}{\sum_J (2J+1)}, \tag{2.26}$$

and represent mean effects from other nucleons on a nucleon in a specific single-particle orbit. In Fig. 2.5 the gap between $0d_{3/2}$ and $0f_{7/2}$ is quite large for $^{40}$Ca ($Z = 20$) down to $^{34}$Si ($Z = 14$), but decreases for lower $Z$ values, opening the gap between $1s_{1/2}$ and $0d_{3/2}$ and making $N = 16$ a magic number for $^{24}$O. The reduced gap between $0d_{3/2}$ and $0f_{7/2}$

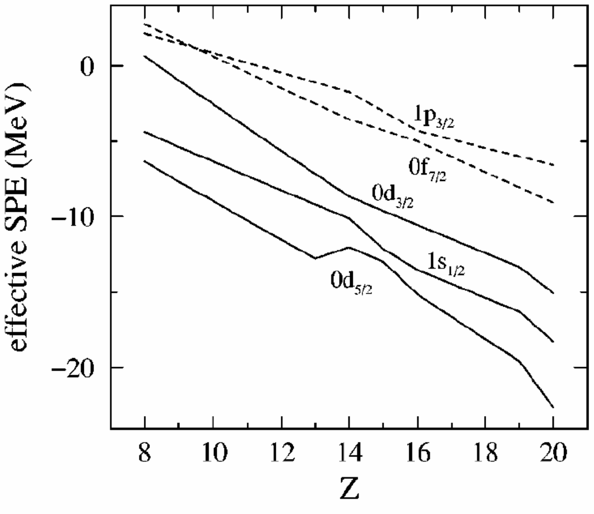

**Figure 2.5:** Effective neutron single-particle energies for $N = 20$ isotopes as a function of proton number. Due to the strong attractive $T = 0$ monopole interaction the ESPE go down alltogether with increasing $Z$. The figure is taken from Ref. [36].

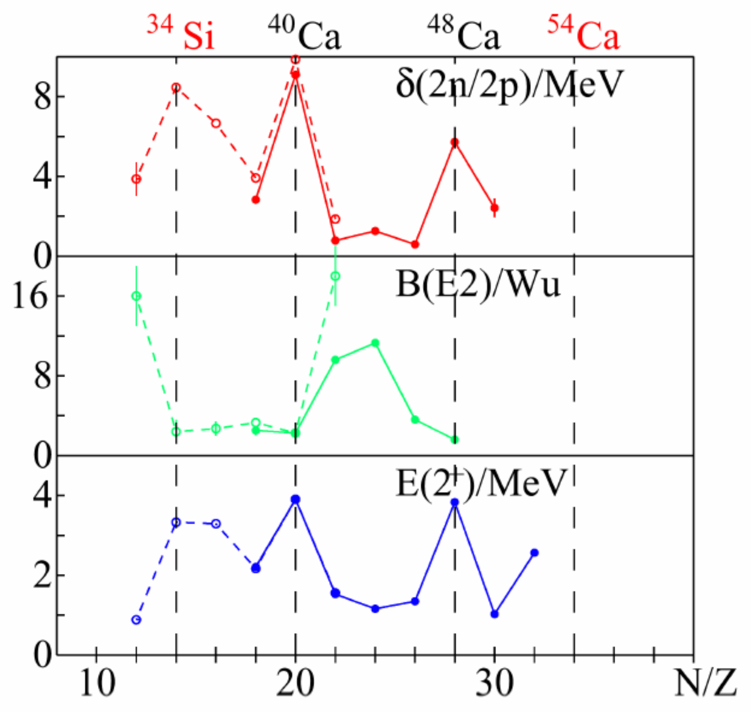

**Figure 2.6:** Shell structure signatures for even-even $N = 20$ isotones (dashed line) and $Z = 20$ isotopes (solid line). The figure is taken from Ref. [14].

in $^{32}$Mg allows for an intruder configuration which dominates the ground state with $2p2h$ neutron excitations to the $pf$ shell [28, 36].

It has been pointed out in Ref. [38] that the driving force behind this evolution of magic numbers is the $(\sigma \cdot \sigma)(\tau \cdot \tau)$ part of the $NN$ interaction, where $\sigma$ denotes the spin and $\tau$ the isospin, respectively. This part has large matrix elements for the spin-flip isospin-flip processes $\pi j_> \rightarrow \mu j_<$ and vice versa, where $\pi$ and $\mu$ denote the proton and neutron, respectively, while $j_> = l + 1/2$ and $j_< = l - 1/2$. Thus, removing protons from the $0d_{5/2}$ shell shifts the neutron $0d_{3/2}$ shell upwards due to their strong attractive monopole $T = 0$ interaction.

As various shell model investigations of the shell structure evolution around the "island of inversion" preserved full isospin symmetry [36, 39, 40, 41, 42] the scenario is expected to be symmetric with respect to the isospin projection quantum number $T_z$ and may only slightly be affected by decreasing neutron binding energies [43, 44]. It can be verified with experimental measurements. In Fig. 2.6 the experimentally known second differences of the binding energies $\delta_{2n}$ and $\delta_{2p}$, respectively, the $\mathrm{B}(E2; 2_1^+ \rightarrow 0_{g.s.}^+)$ and the $E2_1^+$ values are displayed for $N = 20$ and $Z = 20$ nuclei. For the mirror pair $^{38}$Ca and $^{38}$Ar the mirror energy difference between the first excited excited $2^+$ state, defined as $\Delta E_M = E_x(I, T_z = -T) - E_x(I, T_z = +T)$, is positive ($\Delta E_M = 39$ keV). This is expected for a hole configuration due to the different Coulomb repulsion in the $0^+$ ground state and the excited state. However, the lighter proton-rich Ca nuclei are situated closer to the proton dripline as their corresponding mirror nuclei to the neutron dripline due to the different Coulomb repulsion. This may destroy the $T_z$ symmetry. Crucial experimental information can therefore be deduced from a $\gamma$-spectroscopic measurement of $^{36}$Ca; $2_1^+$ – $^{36}$S; $2_1^+$, the heaviest $T = 2$ mirror nuclei studied so far.

# 3 Production, Selection, and Identification of Unstable Nuclei for RISING

At GSI all heavy ion acceleration processes start with the linear accelerator UNILAC [45]. This device can be used to deliver stable beams from hydrogen to uranium up to energies of 11.4 *A* MeV. For higher energies, needed in experiments using the IFS technique, a UNILAC beam bunch is fed into the heavy ion synchrotron SIS [46], where it can be accelerated up to final energies of 1 to 4.5 *A* GeV, depending on the element number. The stable beam is extracted from the SIS and focused on a primary reaction target placed at the entrance of the FRS. Two reaction mechanisms, projectile fragmentation and induced fission, are used in order to produce beams of unstable nuclei. The nuclei of interest are then separated and identified before they strike on a secondary target. The generated reaction channels are identified with the calorimeter telescope CATE.

In this chapter the particle production, selection, and identification part of the RISING setup is explained on the basis of a $^{37}$Ca secondary beam used to populate exotic nuclei close to the proton dripline using the two-step fragmentation technique. In this experiment a primary beam of $^{40}$Ca at an energy of 420 *A* MeV and an average intensity of $3 \times 10^8$ particles per second impinges on a 4007 mg/cm$^2$ thick $^9$Be primary target. Out of the fragmentation products $^{37}$Ca is selected and strikes on a 700 mg/cm$^2$ thick $7 \times 7$ cm$^2$ secondary $^9$Be target with an energy of 195.7 *A* MeV. The in-beam $\gamma$-ray spectroscopy experiment is performed at the secondary target.

## 3.1 Projectile Fragmentation

When heavy ions penetrate a target different reaction mechanisms can occur, depending on the beam velocity. The energy region below 20 *A* MeV is dominated by Coulomb scatterings, transfer reactions, and fusion evaporation. For high energies, however, the reactions are regarded as being "pure" fragmentations [47]. The fragmentation process consists of two steps, which occur on two distinctly different time scales. Fig. 3.1 shows a schematic view of the two-step process that is well described by the abrasion-ablation model [48].

In the first step, which has a time scale of several $10^{-23}$ s, the beam collides on the target and abrades nucleons. These nucleons, called participants, belong to the geometrically overlapping parts between projectile and target. The nucleons outside of the interacting zone, called the spectator, continue their travel but gain an excitation energy that is in a first approximation proportional to the number of abraded nucleons. This excitation energy stems from the excess of surface energy due to the shape change of the abraded fragment. In a second step, the ablation phase, the prefragment de-excites by evaporating neutrons, protons, or light particles, by fissioning, and finally emission of $\gamma$-rays. The characteristic time scale for the emission of particles varies between $\sim 10^{-16}$ s for an excitation energy of 10 MeV and $\sim 10^{-21}$ s at 200 MeV.

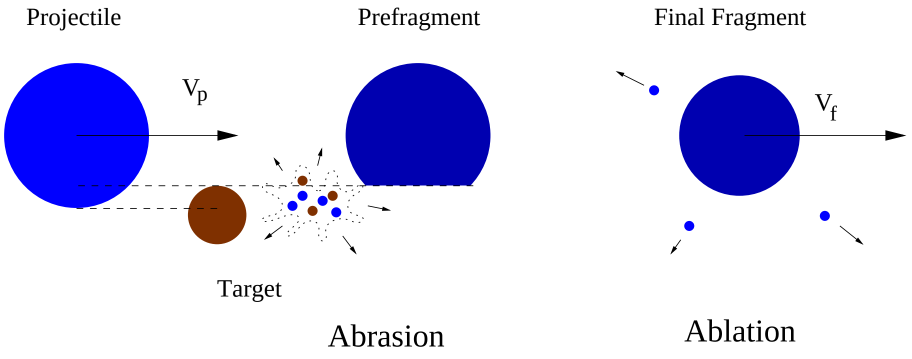

**Figure 3.1:** Illustration of the fragmentation process. See text for details.

With the fragmentation process a parallel momentum spread is introduced into the previously monoenergetic beam. One approach by Goldhaber [47] to quantify this spread is based on the Fermi momentum of the removed nucleons:

$$\sigma_{||}^2 = \sigma_0^2 \frac{A_F(A_P - A_F)}{A_P - 1}. \tag{3.1}$$

In this equation $A_P$ and $A_F$ denote the mass of projectile and fragment, respectively. $\sigma_0$ is a fit parameter which has been determined experimentally to 90 MeV/c [47]. The spread in momentum due to the fragmentation reaction can also be described with other models [49, 50, 51], but they all yield comparable results for fragmentation reactions at high energies.

Along with the parallel momentum spread goes a reduction of the mean velocity by the factor $\frac{v_F}{v_P}$, where $v_P$ and $v_F$ denote the velocity of the projectile and fragment, respectively. This can easily be pictured by the fact that stripped off nucleons have to overcome the nuclei's binding energy. A simple model that quantifies the reduction in heavy ion velocity is given by Borrel *et al.* [52] and yields:

$$\frac{v_F}{v_P} = \sqrt{1 - \frac{B_n(A_P - A_F)}{A_F E_P}}. \tag{3.2}$$

In this equation $E_P$ is the projectile's energy and $B_n = 8$ MeV the energy necessary to ablate one nucleon. Besides this model further descriptions are available [49, 51, 53], all leading to similar results for few nucleon knockouts.

The rate of a specific fragment produced in the primary target can be calculated from

$$\text{fragments } [\text{s}^{-1}] = \text{target nuclei } [\text{cm}^{-2}] \cdot \text{beam intensity } [\text{s}^{-1}] \cdot \text{cross section } [\text{cm}^{+2}],$$

where the cross sections of the fragmentation reactions can be taken from the EPAX parameterisation [54, 55] that is based on experimental data. For any given projectile target combination a vast spectrum of different fragments is produced and the cross-section for the isotope of interest is generally small to the competing cross-sections of other reaction channels. Therefore, the heavy ions of interest must be separated with the FRS from unwanted reaction residues before they can be used for secondary reaction experiments. In the separation process not all fragments of interest are transmitted to the secondary target due to the momentum and angular acceptance of the FRS. Further losses are due to

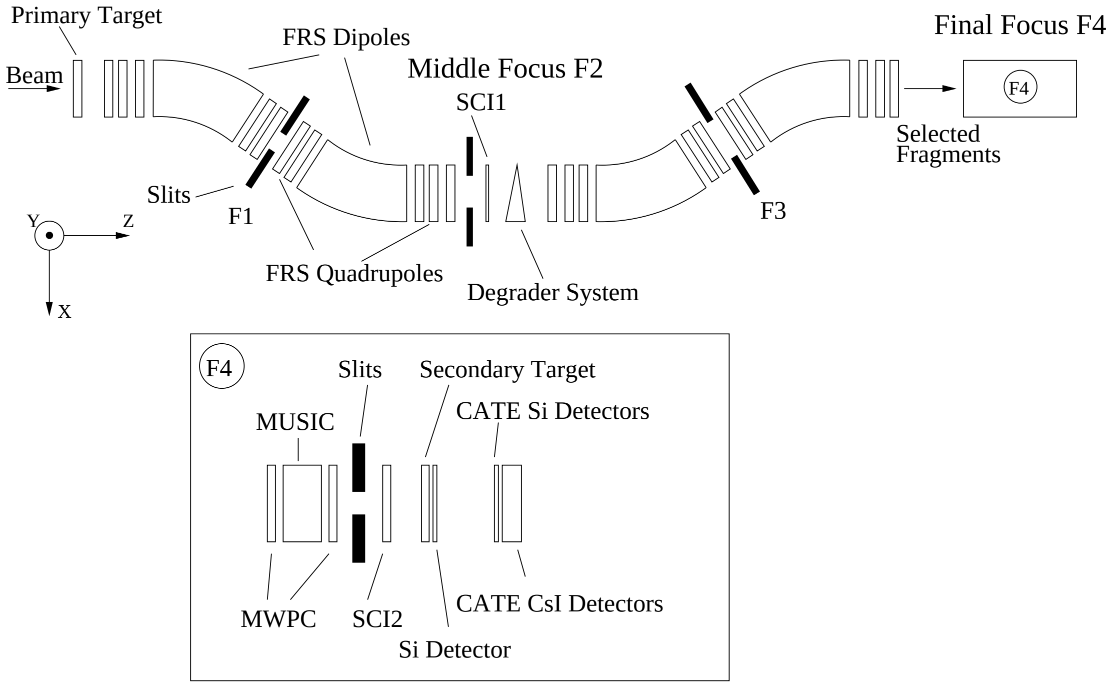

**Figure 3.2:** Schematic layout of the particle selection and identification used in RISING. The FRS selects and identifies the fragments reaching the final focus. The CATE array identifies the reaction channels after the secondary target. The particle identification detector setup consists of two multiwire proportional counters (MWPC), two scintillation detectors (SCI1 and SCI2), and an ionisation chamber (MUSIC) for the FRS part, while CATE consists of Si and CsI detectors. After the secondary target another Si detector is mounted. In addition, slits are available at each focal plane (F1-F4).

reactions with material inserted into the beam line that is necessary for the separation process and for the particle identification. Hence, transmission losses of the FRS have to be included to obtain the beam rate on the secondary target.

## 3.2 Heavy Ion In-Flight Separation and Identification with the FRS

The fragment separator FRS, shown in Fig. 3.2, is a high resolution zero-degree spectrometer that consists mainly of four 30° dipole magnets and a set of quadrupoles before and after each dipole. The total length of the FRS is 74 m for heavy ions moving along the central trajectory. Due to geometrical constraints the FRS has a longitudinal-momentum

| | |
|---|---|
| Dispersion (cm/%) | $D_{TA-F2}$ = –6.474<br>$D_{F2-F4}$ = 7.239 |
| Acceptance | Momentum: $\Delta p/p = \pm 1$ %<br>Angle: $\Delta\vartheta = \pm 10$ mrad |
| Magnetic Rigidity<br>Resolving power | $B\rho_{max} = 18$ Tm<br>$B\rho/\Delta B\rho = 1600$ |

**Table 3.1:** FRS parameters when used in the achromatic mode. See text for details.

acceptance of $\Delta p/p = \pm 1$ % and an angular acceptance of $\Delta\vartheta = \pm 10$ mrad. The main characteristics of the FRS are summarised in Tab. 3.4.

The first two dipole magnets of the FRS serve as a first filter of the projectile fragments. In the middle focal plane a specially shaped degrader is placed which allows a second filter with the remaining two dipole magnets. This $B\rho$–$\Delta E$–$B\rho$ method allows an ideal separation of the nucleus of interest. In the following sections a general presentation of the FRS is given. A deeper insight is provided by Ref. [5].

### 3.2.1 The $B\rho$–$\Delta E$–$B\rho$ Method

The motion of heavy ions with the charge $q$ and the momentum $p = mv$ in a homogeneous magnetic field $B$ is described by the Lorentz force:

$$\frac{d}{dt}(m \cdot \vec{v}) = \vec{F}_{Lorentz} \equiv q \cdot \vec{v} \times \vec{B}. \tag{3.3}$$

For the FRS, the magnetic field is perpendicular to the heavy ions‘ momenta and the Lorentz force is set to compensate the centrifugal force:

$$F_{Lorentz} = \frac{mv^2}{\rho}, \tag{3.4}$$

with $\rho$ being the bending radius of the trajectory. Furthermore, the energies are relativistic, so the momentum transforms to $p = \beta\gamma Auc$ with the velocity $\beta = \frac{v}{c}$, the Lorentz-factor $\gamma = \sqrt{1/(1-\beta^2)}$, the speed of light $c$, and the atomic mass unit $u$. If the heavy ions are fully stripped ($q = Ze$), this leads to:

$$\frac{A}{Z} = \frac{B\rho e}{\beta\gamma uc}. \tag{3.5}$$

The FRS separates the fragmentation products in three stages. In the first stage, the first pair of dipole magnets selects heavy ions according to their magnetic rigidity. As the bending radius for the dipole magnets is fixed to $\rho = 11.25$ m and the velocity $\beta c$ is approximately the same for all fragments at the output of the target, the $B$-field applied to the magnets determines the selected $A/Z$ range within the acceptance of the magnets.

The central image plane of the FRS (middle focus) is dispersive. This means that heavy ions with different magnetic rigidity $B\rho$ pass the middle focus at different X-positions. The distance ΔX between two individual heavy ions is proportional to their relative difference in magnetic rigidity $\Delta B\rho/B\rho$:

$$\Delta X = D \cdot \frac{\Delta B\rho}{B\rho}, \tag{3.6}$$

where $D$ is the constant of proportionality called dispersion. From the primary target to the middle focus the dispersion is $D_{TA-F2} = -6.474$ cm/%. Thus, the accepted $B\rho$ range can be reduced if X-position slits are inserted. If two fragments with the same magnetic rigidity enter the dipoles at the same position but with a different angle, they exit the dipoles at a different position. The quadrupoles before and after every dipole magnet are necessary to eliminate this angular dependence.

The fragments that reach the middle focus have to penetrate through a 3 mm thick scintillator and a degrader system [56]. The thereby occurring energy loss is the second stage of the separation procedure. The degrader system consists of three different parts: A set of plane plates, a wedge-shaped disc degrader pair, and a wedge-shaped plate degrader pair, all displayed in Fig. 3.3. The ladder and the wedges present the homogeneous parts of the degrader, i.e. their thickness is independent of the X-position. With the wedges any thickness between 270 and 6750 mg/cm$^2$ of aluminium can be set up, while the ladder consists of several aluminium blocks of a fixed thickness. If the degrader disc is used, another 737 mg/cm$^2$ of aluminium are inserted into the beam line. By changing its slope, that is by rotating it along the beam axis, different ion optical settings can be achieved. In the monoenergetic mode, the degrader system is set to compensate the momentum spread of a selected fragment in the target. As a result, the second pair of dipole magnets bents all fragments the same way and the spatial distribution at the final focal plane remains the same as at the intermediate focal plane.

In the RISING fast beam campaign the selected fragments have to strike on a secondary target at the final focal plane. Therefore, the fragments are focused on a small spot at the

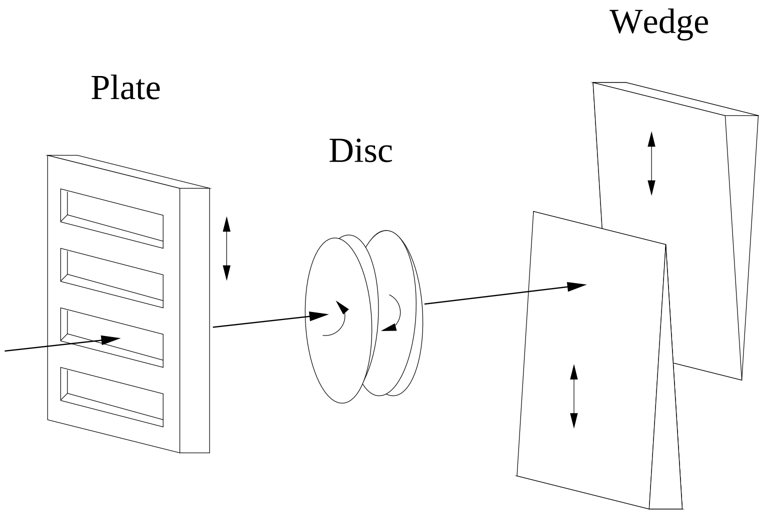

**Figure 3.3:** Schematic view of the FRS degrader system. See text for details.

secondary target position. This is achieved by putting the degrader in the achromatic mode. Thus, the momenta of the selected fragments are decreased due to the energy loss in the degrader and the scintillator SCI1 by a constant factor so that the fragments of interest are refocused on the centre of the secondary target.

In the third stage, the $B\rho$ of the second pair of dipole magnets is set according to the energy loss of the fragment of interest in the scintillator SCI1 and degrader system. Thereby, fragmentation products which have a different energy loss (which results in a different $B\rho$) are separated if they lay outside the acceptance of the dipole magnets. The amount of unwanted fragments reaching the secondary target can be further reduced by inserting slits in front of SCI2.

### 3.2.2 Simulations of Different FRS Conditions

Changing the primary beam energy, primary target thickness, and degrader thickness varies the secondary beam energy and rate on the secondary target as well as the purity of the beam cocktail. In order to find the optimum condition for the $^{37}$Ca secondary beam, Monte Carlo based simulations of the FRS have to be performed with the LISE++ [57] programme. Two values are chosen as primary $^{9}$Be target thicknesses, 2526 and 4007 mg/cm$^{2}$, respectively. The secondary beam energy striking on the secondary target influences directly the $\gamma$-ray detection energy resolution and efficiency of the RISING setup.

| Beam Energy [*A* MeV] | Target Thickness [mg/cm$^2$] | Degrader Thickness [mg/cm$^2$] | Secondary Beam Energy [*A* MeV] | $^{37}$Ca Rate | $^{37}$Ca Purity [%] |
|---|---|---|---|---|---|
| 440 | 4007 | 4650 | 130 | 0.75 | 100 |
| 360 | 4007 | 1300 | 150 | 0.79 | 84 |
| 380 | 4007 | 900 | 200 | 1.00 | 82 |
| 420 | 4007 | 2300 | 200 | 0.97 | 78 |

**Table 3.2:** Simulated $^{37}$Ca secondary beam rate and purity for secondary beam energies of 130, 150, and 200 *A* MeV striking on the secondary target. The secondary beam rate is normalised to the highest simulated rate.

Details on this subject are shown in the next chapter. Three different secondary beam energies are chosen for the simulations, namely 130, 150, and 200 *A* MeV. The primary beam energy and degrader thicknesses are varied accordingly. All slits are kept open except for the slits in front of SCI2, which are set to ± 35 mm. The settings that give the highest $^{37}$Ca secondary beam rates for the three secondary beam energies are displayed in Tab. 3.2.

For a secondary beam energy of 200 *A* MeV the highest rate is obtained for a primary beam energy of 380 *A* MeV and a primary target of thickness of 4007 mg/cm$^2$. However, this implies the use of a thin degrader at the middle focus and therewith a high amount of unwanted fragments reaching the final focus area hit the slits in front of SCI2. To separate these fragments already at an earlier stage, a primary beam energy of 420 *A* MeV and a degrader thickness of 2.3 g/cm$^2$ is chosen for the experiment. Decreasing the secondary beam energy to 150 or 130 *A* MeV results in the loss of $^{37}$Ca secondary beam rates of more than 20 %.

A more detailed simulation is performed with the MOCADI [58] programme that also includes the effective thicknesses of the primary target, the SCI1, and the degrader system which are deduced from energy-loss measurements during the calibration process of the FRS. From this simulation the $^{37}$Ca secondary beam reaches the middle focal plane at an energy of 309 *A* MeV ($B\rho$ = 5.05 Tm) and the final focal plane area with an energy of 222 *A* MeV ($B\rho$ = 4.20 Tm) before penetrating through the material. The $^{37}$Ca secondary beam energy in front of the secondary target is 195.7 *A* MeV.

### 3.2.3 The FRS Particle Identification Detectors

The particles that reach the final focal plane of the FRS are identified on an event-by-event basis by their specific parameters: Position and velocity ($\beta$) yield together with the applied $B$-field the mass to charge ratio $A/Z$, while an energy loss measurement yields the nuclear charge of the nuclei. A precise $\beta$ and position measurement of the fragments is also necessary to achieve a good energy resolution after the Doppler correction of detected $\gamma$-rays.

For the particle identification different detectors are used in the experiment: The X-position of a fragment is deduced with the scintillator SCI1 at the middle focal plane and with a Si detector and the multiwire proportional counters MWPCs [59] at the final focal plane. The velocity is determined by a time-of-flight (TOF) measurement between the intermediate and final focal plane (flight path: 37 m) with the two scintillators SCI1 and SCI2. The energy loss of the fragments is measured in the multi sampling ionisation chamber MUSIC [60]. This information provides unambiguous particle identification in mass and charge in front of the secondary target.

The working principles of the detectors are described in the following sections. Prior to identifying different fragments in the FRS, the scintillators and the MUSIC detector are calibrated with stable primary beam at different $\beta$ values. This is achieved by selecting different initial beam energies and by putting material of different thicknesses into the beamline, as shown in Tab. 3.3. The $\beta$ values are obtained by energy loss calculations with the programme ATIMA [61] and include the material inserted into the beam line through the degrader.

| Beam | Energy [$A$ MeV] | Inserted Matter | $\beta$ |
|---|---|---|---|
| $^{48}$Ca | 600 | SCI1 (3 mm thickness) | 0.7912 |
| $^{48}$Ca | 350 | SCI1, 5.4 g/cm$^2$ degrader | 0.5758 |
| $^{48}$Ca | 350 | SCI1 | 0.6816 |
| $^{48}$Ca | 160 | SCI1 | 0.5027 |
| $^{40}$Ca | 389.87 | 4 g/cm$^2$ target, SCI1, 2.3 g/cm$^2$ degrader | 0.5610 |

**Table 3.3:** Stable primary beam used to calibrate MUSIC and TOF. The $\beta$ values are calculated with the ATIMA programme and include all material inserted into the beam through the degrader.

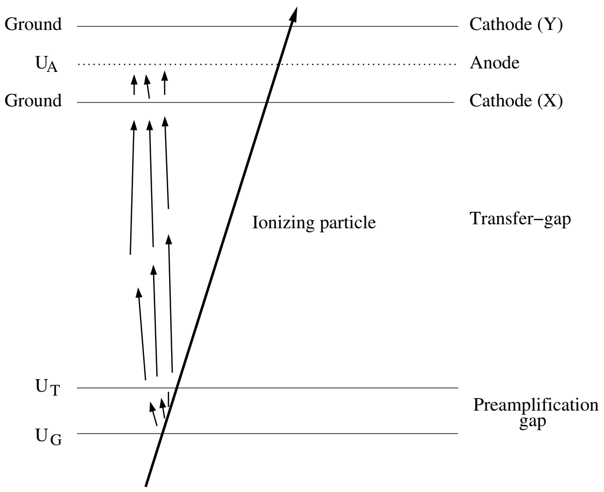

**Figure 3.4:** Schematic layout of a multi sampling ionisation chamber MWPC. See text for details.

### The Multi Wire Proportional Counter MWPC

The multi wire proportional counters MWPCs [59] are used (i) to centre the primary beam on the optical axis after inserting target, degrader, and SCI1, (ii) to calibrate the position sensitivity of the SCI1, and (iii) to calibrate and correct the position dependence of the MUSIC energy signals. The two MWPCs used at the final focal plane are also used to track the secondary beam in front of the secondary target.

The MWPCs have a front size of 20 × 20 $\mathrm{cm}^2$, a thickness of 10 cm, and are filled with a mixture of 80 % Ar and 20 % $\mathrm{CO}_2$ at atmospheric pressure. A schematic layout of the MWPCs is given in Fig. 3.4. The cathodes X and Y consist of 50 $\mu$m thick gold-plated tungsten wires with a pitch of 1 mm, mounted in vertical and horizontal directions, respectively. The planar anode is mounted in between the cathodes at an angle of 45° with respect to the two cathode planes and consists of 20 $\mu$m thick gold-plated tungsten wires with a pitch of 2 mm. The spacing between each plane is 5 mm. In addition, a planar electrode structure consisting of two meshes labelled $G$ and $T$ and a spacing of 6 mm is added. Voltages applied to these detectors are: $U_G$ = –10 kV, $U_T$ = –2.6 kV, and $U_A$ = +2.5 to +3.7 kV, while the cathodes are kept on ground potential.

**Position determination with the MWPCs** When a charged particle passes through the detector it produces an electron avalanche at the preamplification gap. The avalanche drifts through the transfer-gap to the first cathode plane. Finally, the avalanche reaches the anode plane and a second amplification occurs. Thereby, a positive charge is induced at the adjacent cathode positions and propagates along the wires. Since the cathode wires are connected with each other via delays of 4 ns to create a delay line, signals from both ends of these delay lines are amplified and fed into the stop input of a time-to-digital converter (TDC), while the anode marks the TDC Start signal. Thus, the measured time difference between both ends determines the coordinate position of the particle with the formulae:

$$X = a_{X_0} + a_{X_1} \frac{X_L - X_R}{2}, \tag{3.7}$$

$$Y = a_{Y_0} + a_{Y_1} \frac{Y_U - Y_D}{2}, \tag{3.8}$$

where $X_L$, $X_R$, $Y_U$, $Y_D$ are the four TDC channels from the left, right, up, and down side of the MWPC. The offsets $a_{X_0}$ and $a_{Y_0}$ are determined by putting narrow slits in front of the MWPCs or after the detector if the trigger is coming from a detector positioned after these slits. Only slits to determine the X-offset are available in most cases, but this represents the far more important coordinate to calibrate the FRS detectors and material thicknesses. The calibration factors $a_{X_1}$ and $a_{Y_1}$ depend on the delay lines and the TDC range used. The TDCs used in the present experiment have a range of 1200 ns spread over 4096 channels. The readout distance of the wires is 2 mm and the delays are 4 ns each. This leads to a calibration factor of 0.1465 mm/channel. To obtain more precise values, the values from a TDC calibration are taken as calibration factors.

### The $\Delta E$ Detector MUSIC

To determine the charge of the incoming nuclei reaching the final focal plane, the multi sampling ionisation chamber MUSIC [60] is used. This chamber consists of a cathode, a Frisch grid, and eight independent anode strips, as shown in Fig. 3.5. The active volume of the MUSIC detector covers a surface area of 100 × 200 $\text{mm}^2$ and a length of 400 mm. The MUSIC detector is operated with a constant gas flow of pure $CF_4$ at atmospheric pressure and at room temperature.

When the heavy ions penetrate the MUSIC chamber, the counting gas inside the detector generates a cloud of electrons along the heavy ions' trajectories. These electrons drift to the anode strips and are read out by a combination of charge sensitive preamplifiers

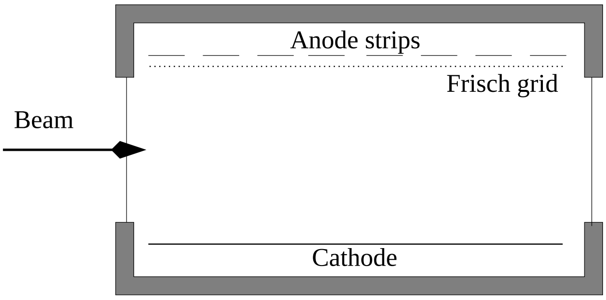

**Figure 3.5:** Schematic layout of the multi sampling ionisation chamber MUSIC. See text for details.

and shapers. The detected charge is proportional to the energy loss at each strip. The total energy loss is extracted from the geometrical average $\overline{\Delta E_{tot}} = \sqrt[8]{\Delta E_1 \cdots \Delta E_8}$ of the individual energy losses.

**Determination of the the fragments' nuclear charge $Z$ from MUSIC** The energy loss measured in the MUSIC detector at high velocities for fragments with the atomic number $Z$ can be associated with the Bethe formula for the stopping power of particles [62]:

$$-\frac{dE}{dx} = \frac{4\pi}{m_e c^2} \frac{\tilde{Z} Z^2 N_a \rho}{\tilde{A} \beta^2} \left( \frac{e^2}{4\pi\varepsilon_0} \right) \left[ ln \left( \frac{2 m_e c^2 \beta^2}{I(1-\beta^2)} \right) - \beta^2 \right]. \tag{3.9}$$

In this formula $\tilde{Z}$, $\tilde{A}$, $\rho$, and $I$ denote the atomic number, mass, density, and mean excitation potential of the absorbing material, $m_e$ the mass of the electron, and $N_a$ the Avogadro Number.

For particles being slowed down in the same absorber material the stopping power can be expressed as:

$$-\frac{dE}{dx} = Z^2 f(\beta), \tag{3.10}$$

where $f(\beta)$ depends solely on the velocity. As a consequence, $f(\beta)$ can be measured for the primary beam with the atomic number $Z_p$ and then scaled to energy loss values $\frac{dE_f}{dx}$ of fragments with the atomic number $Z_f$ if the $f(\beta)$ value is the same:

$$-\frac{dE_f}{dx}(\beta) = -\frac{Z_f^2}{Z_p^2} \frac{dE_p}{dx}(\beta). \tag{3.11}$$

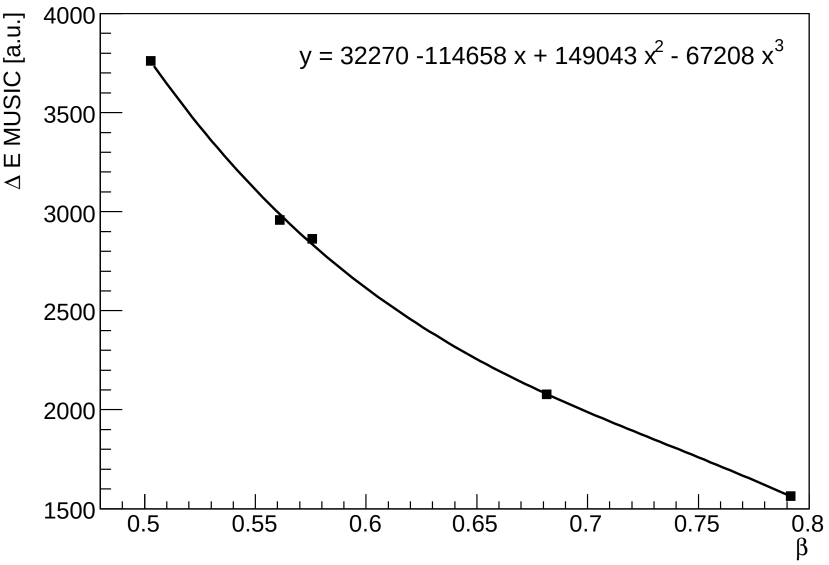

**Figure 3.6:** Calibration of the MUSIC energy loss with primary beam as a function of $\beta$. The five $\beta$ values correspond to calculated energies after passing the inserted material at the middle focal plane.

Thus, in the FRS calibration process the energy loss function is measured for the primary beam settings given in Tab. 3.3. The measured energy losses $\Delta E_p$ are fitted for high velocities in the range $0.5 \leq \beta \leq 0.8$ to a polynomial function of $\beta$:

$$\Delta E_p = a_0 + a_1\beta + a_2\beta^2 + a_3\beta^3. \tag{3.12}$$

The result is shown in Fig. 3.6, where the different $\beta$ values are taken from ATIMA energy loss calculations given in Tab. 3.3.

The fit function is used to determine the charge $Z_f$ of the secondary beam in the experiment, as shown in Fig. 3.7. When the energy loss $\Delta E_f$ of the fragments and their velocity is measured, $Z_f$ is deduced from:

$$Z_f = Z_p \sqrt{\frac{\Delta E_f}{a_0 + a_1\beta + a_2\beta^2 + a_3\beta^3}}. \tag{3.13}$$

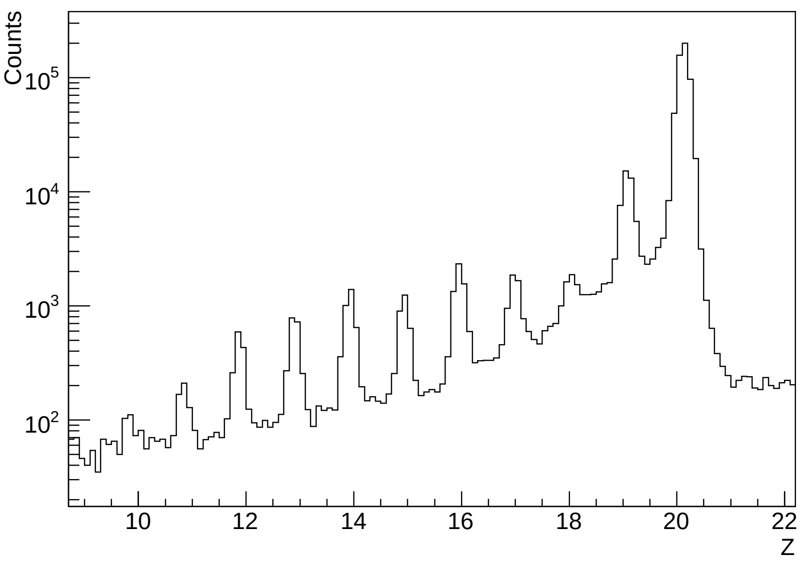

**Figure 3.7:** Reconstructed $Z$ values of the secondary beam reaching the final focus of the FRS. See text for details.

### The Scintillators SCI1 and SCI2

The combination of the two scintillators SCI1 and SCI2 is used to determine the time-of-flight of heavy ions between the middle and final focal plane and their position at these two points. The organic scintillation material used in the experiment is plastic of the type BC4200 (Bicron corporation). This scintillation material provides a fast signal rise time (500 ps) and a high light output. Both scintillators cover the whole active areas of the according focal planes. Due to the higher velocities in the intermediate focal plane, a thicker detector is chosen for SCI1 (3 mm compared to 0.5 mm for SCI2).

For SCI2 the light emitted to each side of the scintillators is detected by fast photomultipliers. For SCI1 only the X-position information is provided due to the lack of space at the intermediate focal plane. The anode signals of the photomultipliers are fed into constant fraction discriminators (CFD). The output of the CFD is put to time to amplitude converters (TAC) and used as start and stop signals. Finally, the TAC signals for the TOF and the position measurements are put into analogue-to-digital converters (ADC). By measuring the time difference between two opposite sides of the detectors a precise position information of the heavy ions penetrating the scintillators is obtained. The electronic scheme is plotted in Fig. 3.8.

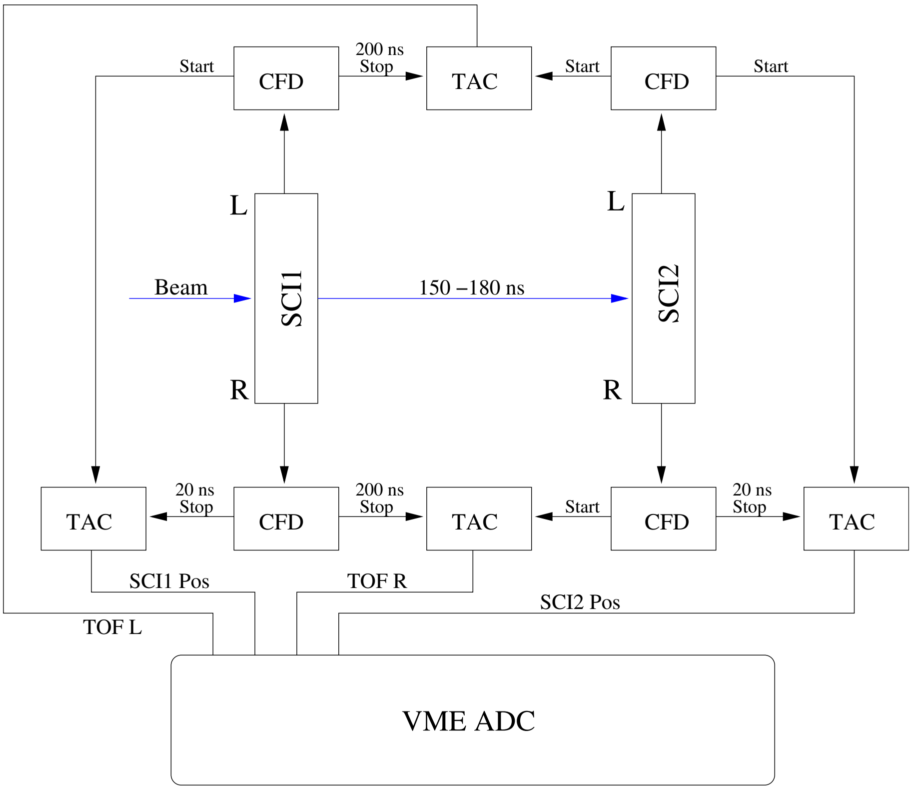

**Figure 3.8:** Electronic scheme of the scintillators SCI1 and SCI2 used to determine the position at the intermediate and final focal point and the time-of-flight between both. See text for details.

**Position information** As many position sensitive detectors are placed at the final focal plane which yield more precise information on the heavy ions' positions, only the scintillator placed at the the intermediate focal plane gives relevant position information. The measured time difference signal of this scintillator have to be associated with a known position information. Therefore, during the SCI1 position calibration process two MWPCs are inserted into the beamline before and after the SCI1 at the middle focus. The position calibration coefficients are determined by defocussing the beam and fitting a two-dimensional spectrum between the tracked beam position from the MWPCs and the time difference measured with the SCI1, as shown in Fig. 3.9. The X-position resolution of 7 mm (FWHM) for the SCI1 is obtained by setting narrow gates on the measured SCI1 position and fitting the corresponding tracked beam position of the two MWPCs.

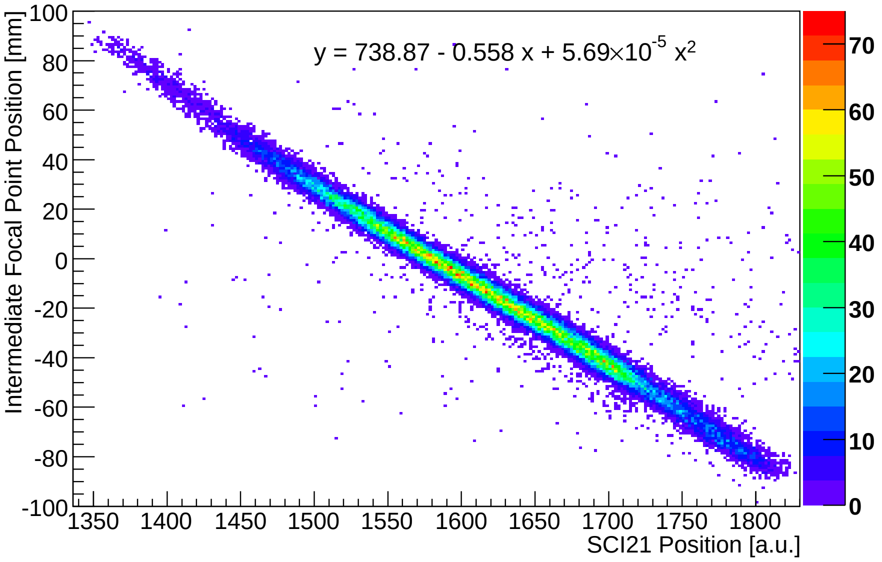

**Figure 3.9:** Position Calibration of SCI1 with the reconstructed position of two MWPCs.

**Time of flight information** The time of flight (TOF) of the fragments in the FRS is obtained by measuring the time differences between SCI1 and SCI2. Fragments that do not move along the central optical axis may yield a different TOF information compared to the ideal trajectory although their velocity ($\beta$) is the same. To compensate this, the final TOF is given by taking the arithmetic average of two measurements, the TOF gained from the two left (TOF$_L$) and the two right (TOF$_R$) photomultipliers, respectively. The intrinsic TOF resolution with these plastic detectors is in the range of 250 ps (FWHM) which is sufficient to distinguish different isotopes in the calcium region.

In the experiment the scintillator SCI2 triggers the data acquisition system at the time $T_2$ (if it is in coincidence with a $\gamma$-ray from one of the three $\gamma$-ray detector branches). Hence, the time signal $T_1$ from SCI1 has to be delayed by the time $\Delta T$ to arrive after the trigger signal from SCI2 in the TAC. Therefore, the measured time-of-flight $TOF_m$ has the form

$$TOF_m = T_1 + \Delta T - T_2. \tag{3.14}$$

However, the real time of flight of the heavy ion is given by the path distance $d$ ($\approx$37 m) between the two scintillators divided by the velocity $v$ of the heavy ion:

$$TOF_{real} = \frac{d}{v} = T_2 - T_1 = \Delta T - TOF_m. \tag{3.15}$$

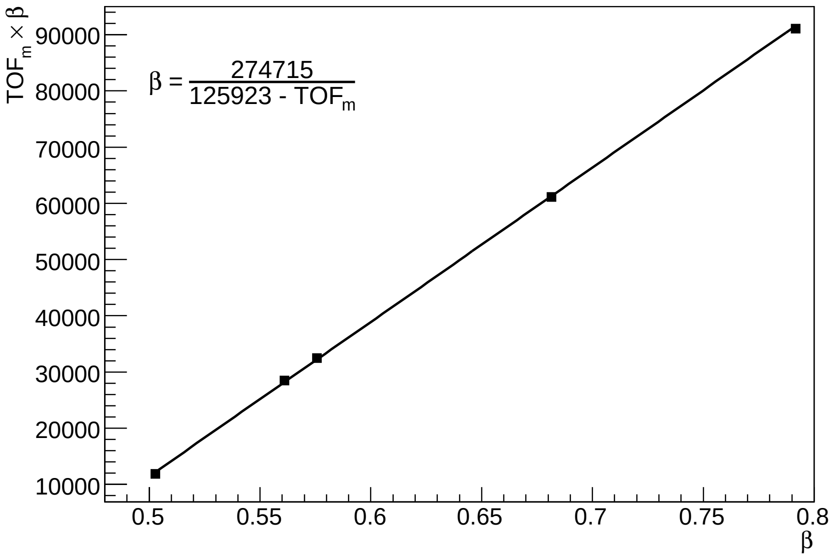

**Figure 3.10:** TOF$_m$ calibration as a function of $\beta$. The five $\beta$ values correspond to calculated energies after passing the inserted material at the middle focal plane.

Multiplying this by $\beta$ and dissolving to $TOF_m\beta$ yields:

$$TOF_m \cdot \beta = \Delta T\beta - \frac{d}{c}. \tag{3.16}$$

The offset $\Delta T$ has to be adjusted so that all fragments reaching the final focus are in the range of the TOF measurement. For the time-of-flight calibration $TOF_m$ is determined for the $\beta$ values given in Tab. 3.3. The product $TOF_m \cdot \beta$ is plotted as a function of $\beta$, displayed in Fig. 3.10, and fitted with the polynomial

$$TOF_m \cdot \beta = a_0 + a_1\beta, \tag{3.17}$$

where the coefficients $a_0$ and $a_1$ represent the experimental variables $\frac{d}{c}$ and $\Delta T$, respectively.

### 3.2.4 Particle Identification Before the Secondary Target

Particles that traverse the second stage of the FRS on the optical axis have the same magnetic rigidity as the dipole magnets. However, after the fragmentation reaction a momentum spread occurs for the secondary beam. Thus, most trajectories deviate from the optical axis. Since the X-positions $X_2$ and $X_4$ of the fragments are measured at the middle and the final focus, the magnetic rigidity $B\rho_{corr}$ is reconstructed by the formula:

$$B\rho_{corr} = B\rho_0 \left(1 - \frac{X_4 - V_{F2-F4}X_2}{D_{F2-F4}}\right), \tag{3.18}$$

where $B\rho_0$ corresponds to the magnetic rigidity of a central trajectory along the optical axis, $D_{F2-F4}$ to the dispersion and $V_{F2-F4} = 1.12$ to the magnification between the middle and final focus, respectively. Combined with the $\beta$ information from the TOF measurement, the mass-to-charge $\frac{A}{Z}$ ratio can be deduced:

$$\frac{A}{Z} = \frac{e}{cu}\frac{B\rho}{\beta\gamma} = \frac{e}{cu}\frac{B\rho_0}{\beta\gamma}\left(1 - \frac{X_4 - V_{F2-F4}X_2}{D_{F2-F4}}\right). \tag{3.19}$$

There are two options to extract the $X_4$ correction parameter: (i) A reconstruction from the two MWPCs position measurements or (ii) by the position measured with the Si detector mounted directly after the target. The $A/Z$ ratio for calcium fragments is shown in Fig. 3.11 for both cases. It demonstrates that the Si detector yields a better $A/Z$ resolution and thus a more accurate position determination at the focal plane.

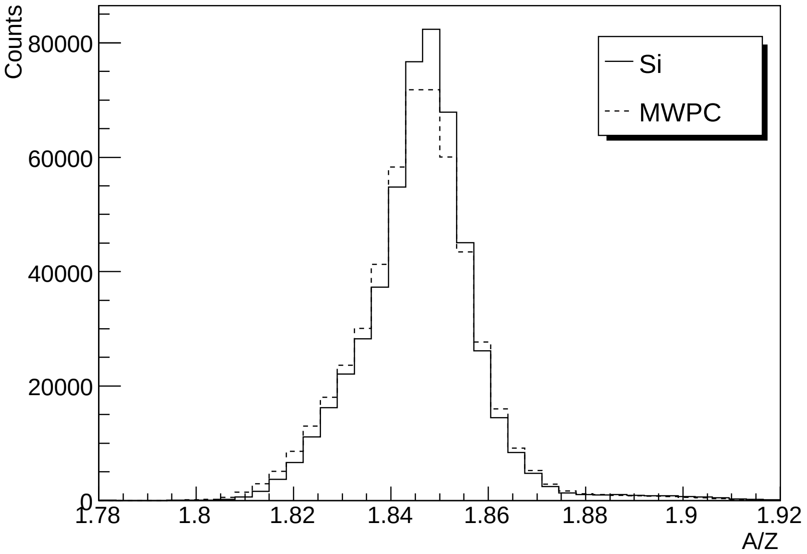

**Figure 3.11:** Mass to charge ratio $A/Z$ obtained for calcium ions with the position information from the Si detector at the target position (solid line) and from the two MWPCs in the final focus area (dashed line).

The particle identification plot of heavy ions that reach the secondary target is shown in Fig. 3.12. About 85 % of all ions are identified as $^{37}$Ca and also a high amount of $^{36}$K is observed. The experimental conditions for the $^{37}$Ca secondary beam are summarised in Tab. 3.4.

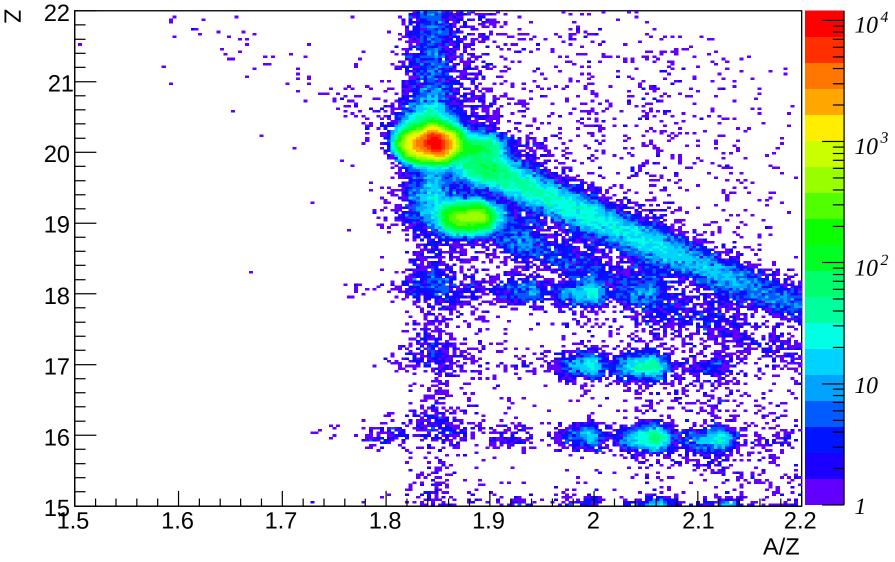

**Figure 3.12:** Two-dimensional $Z$ versus $A/Z$ particle identification plot before the secondary target. About 85 % of all ions are identified as $^{37}$Ca.

| | |
|---|---|
| Primary beam | $^{40}$Ca |
| Primary beam energy ($A$ MeV) | 420 |
| Primary beam intensity (s$^{-1}$) | $3\times10^8$ |
| Primary target thickness | 4007 mg/cm$^2$ $^9$Be |
| Al degrader thickness | 2310 mg/cm$^2$ |
| Secondary beam intensity at middle focus (s$^{-1}$) | $1.1\times10^5$ |
| Secondary beam intensity on secondary target (s$^{-1}$) | 2500 |
| $^{37}$Ca abundance on secondary target (%) | $\approx$ 85 |
| $^{37}$Ca energy on secondary target ($A$ MeV) | 195.7 |
| Secondary target thickness | 700 mg/cm$^2$ $^9$Be |
| Data collection time (h) | 112 |

**Table 3.4:** Experimental parameters of the two-step fragmentation experiment.

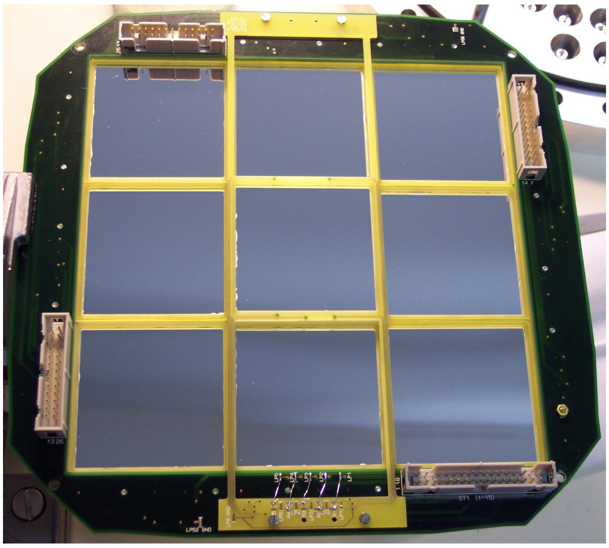

**Figure 3.13:** Photograph of the CATE Si detectors mounted on their motherboard.

## 3.3 Identification of Fragments Produced in the Secondary Target

The reaction channels produced in the secondary target are identified according to their charge $Z$ and mass $A$ with the calorimeter telescope CATE, which is mounted 1400 mm downstream of the secondary target. The complete CATE array consists of $3 \times 3$ stacked detector systems that measure the energy loss $\Delta E$ and the residual energy $E_{res}$. For the $\Delta E$ measurement position sensitive Si detectors are used while CsI(Tl) detectors are used to measure $E_{res}$. A Si detector is also mounted directly after the secondary target ($\approx$ 10 mm) in order to improve the heavy ion position information at the secondary target. This proves to be absolutely crucial for the MINIBALL detectors because they are mounted very close to the target and are thus very sensitive to the direction of the emitted $\gamma$-rays. A very detailed description of the CATE array can be found in Ref. [63]. Here, the basic working principles are emphasised.

### 3.3.1 The CATE Si $\Delta E$ Detectors

The Si $\Delta E$ position sensitive counters (CANBERRA, model: PIPS) have a thickness of 321 $\mu$m. A resistive carbon layer with a resistance of 4–5 k$\Omega$/cm$^2$ serves as front contact. The purpose of this layer is to divide the collected charge to four contact electrodes at the four corners. The measured pulse height at each corner is then taken to determine the heavy ion positions. To reduce nonlinearities in the position determination each corner contact has in addition a resistor of 1.5–1.6 kΩ. The energy loss of the heavy ions in the detector is measured by its back-side contact and is proportional to the total charge created. The energy resolution of the detectors was found to be 2.0 % (FWHM) for relativistic heavy ion beams by Ref. [6]. The geometrical size of each Si frame is 54 × 54 $\text{mm}^2$, while the size of the Si detectors is 50 × 50 $\text{mm}^2$. This results in a geometrical efficiency of 92 % and covers an opening angle of 58 mrad for the total array. A photograph of the Si array mounted on its motherboard is shown in Fig. 3.13.

#### Position Reconstruction with the Si Detector

The charge recorded at the four corners of the Si detector is used to determine the incident position of a heavy ion. It is inversely proportional with respect to the distance of the heavy ion penetrating the Si detector. Therefore, the position in (X, Y) for a detector with a length $2L$ can be determined by the equations:

$$X = L\frac{(B+C)-(A+D)}{A+B+C+D}, \tag{3.20}$$

$$Y = L\frac{(D+C)-(A+B)}{A+B+C+D}, \tag{3.21}$$

where $A$, $B$, $C$ and $D$ mark the pulse heights of the signals at the four corner contacts, as shown in Fig. 3.14.

The position resolution obtained with this method has been measured to be better than 3 × 3 $\text{mm}^2$ [6]. In contrast to early RISING experiments no corrections for a “pin cushion” distortion in the Si detectors [63] have to be applied. The position spectra obtained for $^{37}$Ca fragments are shown in Fig. 3.15 for the Si detector at the secondary target and the total CATE array.

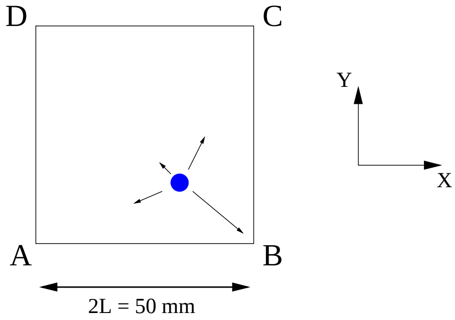

**Figure 3.14:** Schematic drawing of the CATE Si position sensitive detector. The energy measured at the corners is inversely proportional to the distance to the penetrating heavy ion (blue circle). This is indicated by the length of the arrows pointing at the corners.

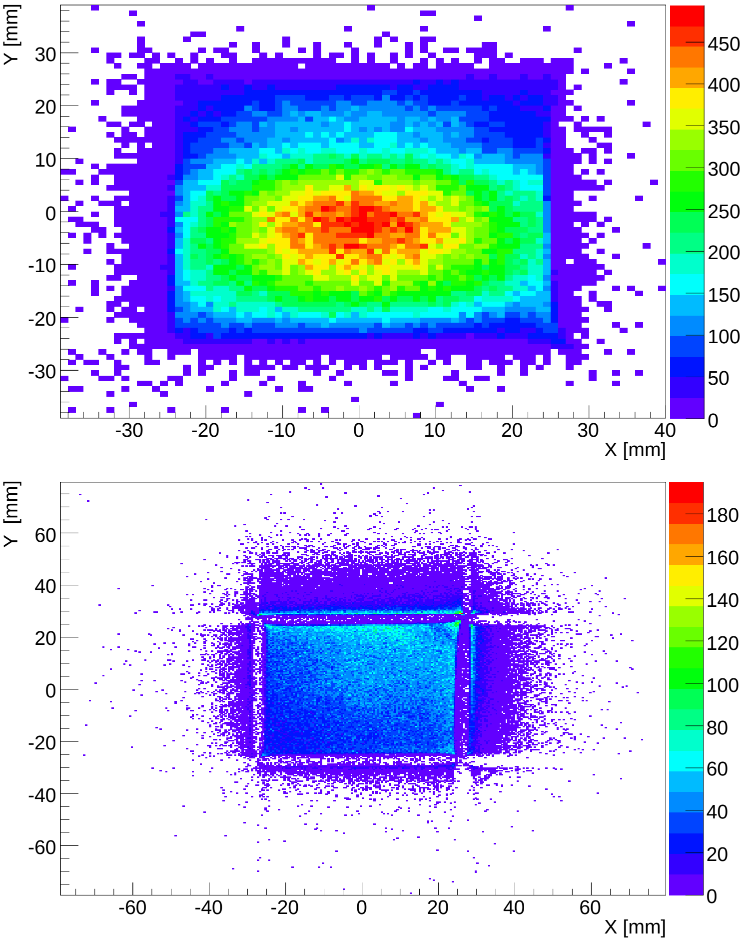

**Figure 3.15:** Top panel: Position spectrum of the $^{37}$Ca secondary beam measured with the Si detector mounted after the secondary target.
Bottom panel: Position spectrum of the $^{37}$Ca secondary beam measured with the CATE Si detectors.

### 3.3.2 The CATE CsI(Tl) $E_{res}$ Detectors

The CATE CsI(Tl) detectors are provided by the company SCIONIX (model: V502P25/18-e2-Cs-X SSX848) and positioned 40 mm behind the Si detectors. The front side of the detectors has the dimension of 54 × 54 mm$^2$ and a thickness of 10 mm, while the back side is of trapezoidal shape with a thickness of 15 mm. For the signal readout a photodiode is attached at the back side in combination with an integrated preamplifier. A 2 $\mu$m thick Mylar foil covers the crystals to assure a good light collection. The intrinsic energy resolution of the CsI(Tl) detector was found to be about 0.7 % for primary beams of $^{86}$Kr and $^{58}$Ni at energies of 145 and 113 $A$ MeV, respectively [6]. The CATE CsI(Tl) detectors are mounted in an aluminium frame with 4 mm thickness between each neighbour, as shown in Fig. 3.16, thus also yielding a geometrical efficiency of 92 %.

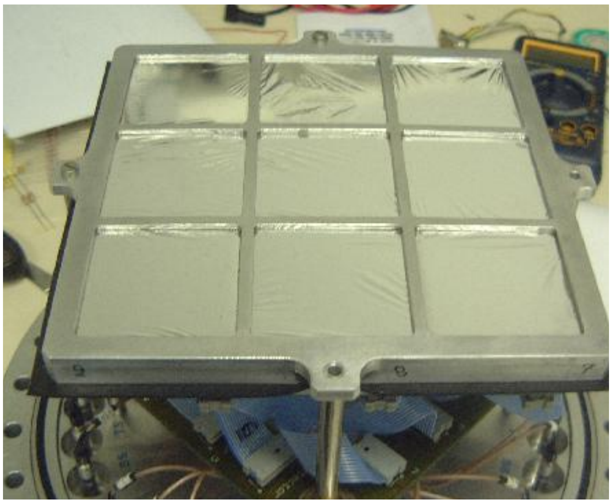

**Figure 3.16:** Photograph of the CATE CsI detectors mounted on their motherboard.

### 3.3.3 Electronics and Readout of the CATE Array

The electronic scheme of the CATE array is displayed in Fig. 3.17, ignoring all the delays necessary in some branches in order to synchronise the CATE array with other detector systems. A voltage of +40 V is applied to the Si detectors via the energy loss preamplifiers of the back side. Also the four position signals from the corners are connected to charge sensitive preamplifiers. After forming the pulse the signals are fed into main amplifiers (model: C.A.E.N. N568B) with 2 $\mu$s shaping time. The energy loss signals from the back

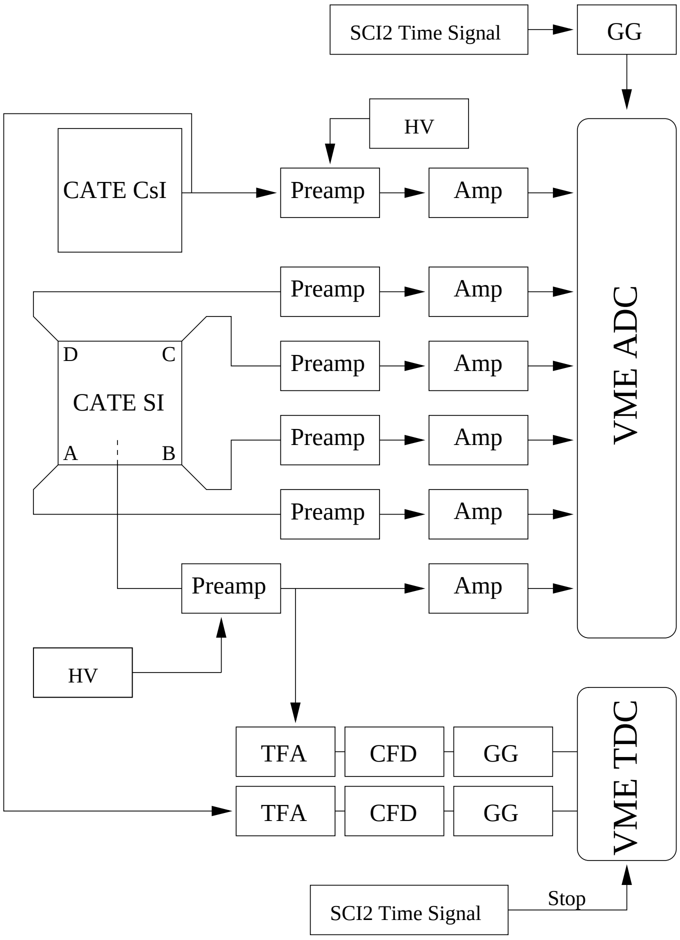

**Figure 3.17:** CATE block diagram of all the electronics used. See text for details.

side are negative. They are inverted and sent together with the signals from the positions to a VME ADC (model: C.A.E.N. V785). The pattern is identical for the CsI detectors, i.e. after the preamplifier the energy signals are put into the same type main amplifier with 2 $\mu$s shaping time and afterwards into the same type ADC. However, unlike the Si detectors, a common unit is supplying the high voltage of $+30$ V.

The time information from the detectors is also generated in an identical manner for both, the Si and the CsI detectors. The signals from the preamplifiers are fed into a timing filter amplifier (TFA) (model: TFA S07-0512 from the TU Darmstadt) and from there into a CFD to produce a logic signal. From this signal a gate is produced with a gate generator (GG) which creates the start signal in a TDC and is stopped by the common SCI2 trigger signal.

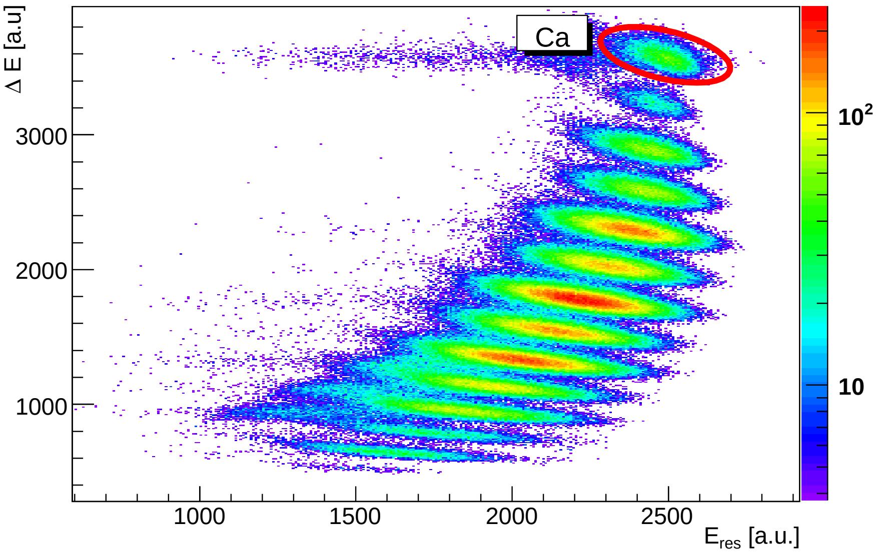

**Figure 3.18:** Particle identification after the secondary target using the $\Delta E - E_{res}$ information of the CATE detectors.

### 3.3.4 The CATE $\Delta E - E_{res}$ Plot — Corrections Applied to the CATE CsI(Tl) Detectors

The element number $Z$ and mass number $A$ of the fragments after the secondary target are determined by plotting the energy loss $\Delta E$ against the residual energy $E_{res}$. An example of a raw $\Delta E - E_{res}$ plot, gated on incoming $^{37}$Ca particles and requesting a particle-$\gamma$ coincidence, is shown in Fig. 3.18.

The separation for the different elements is sufficient, but different masses cannot be resolved due to several reasons: Firstly, the heavy ions reach the final focus area with different velocities, i.e. with different total energies. Secondly, in Ref. [63] is shown that the energy signal of the CsI(Tl) detectors is dependent on the hit position on the detector. These effects need to be corrected using the position sensitivity of the CATE Si detectors and the TOF measurement between SCI1 and SCI2. The most severe reason is, however, the momentum spread introduced by the secondary fragmentation reaction. Eq. 3.1 shows that this spread enlarges with the amount of nuclei removed from the projectile. Since this momentum spread cannot be corrected for, only for few nucleon removal reactions a high correlation between mass and the measured energy $E_{res}$ is expected.

To improve the energy resolution of the CsI(Tl) detectors, the dependence between the measured residual energy on the fragment velocity $\beta$ and on the radial distance of the CsI(Tl) detectors is investigated. Wide gates are imposed in the $\Delta E - E_{res}$ plots on calcium ions. Fig. 3.19 displays the two-dimensional plot between the residual energy $E_{res}$ and the velocity $\beta$. This plot shows a linear dependence that is corrected by a first order polynomial.

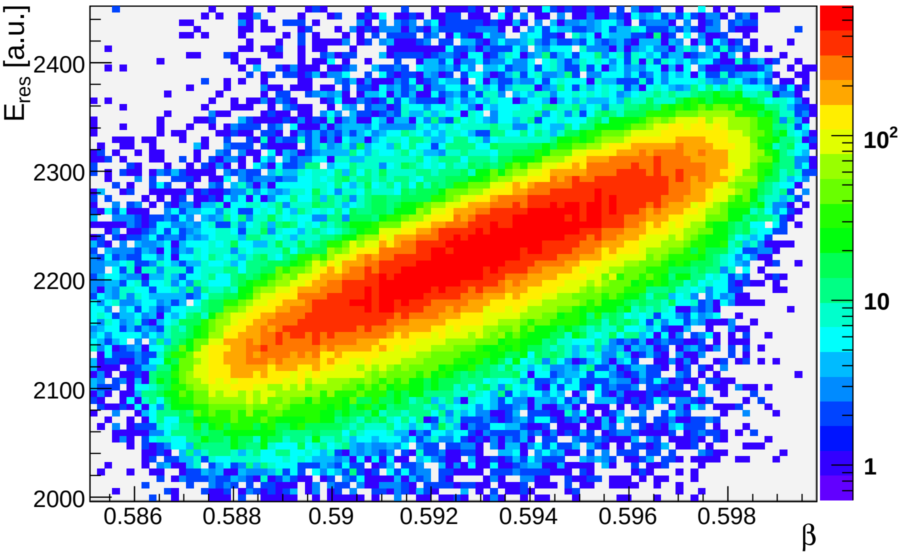

**Figure 3.19:** $\beta$-dependence of measured $E_{res}$. See text for details.

The radial distance of the heavy ions to the CsI(Tl) centre is measured by the position sensitive Si detectors. Hence, the $\beta$ corrected residual energy $E_{res}$ of the CsI(Tl) detectors can be plotted as a function of the radial distance, as shown in Fig. 3.20. Again, the linear dependence is evident and is corrected for. After applying these two corrections an energy resolution of 2 % is achieved for the secondary $^{37}$Ca beam.

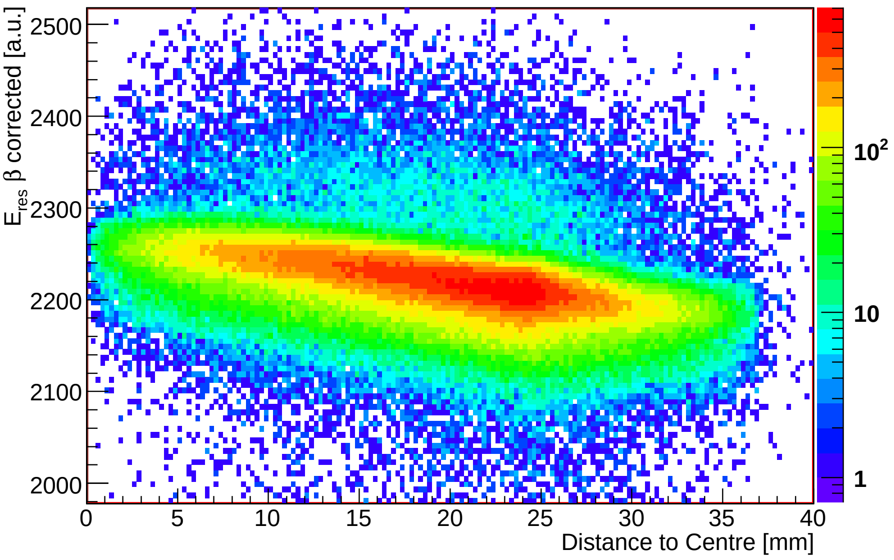

**Figure 3.20:** Radial dependence of the velocity corrected $E_{res}$. See text for details.

# 4 The RISING Fast Beam Setup — Gamma-Ray Detection at Relativistic Energies

With the SIS-FRS combination at GSI secondary beam energies up to 1 $A$ GeV for fragments with an element number up to $Z = 92$ can be provided. This is about one order of magnitude higher than secondary beam energies obtainable with other fragment separator setups as the A1900 [64] at MSU, Alpha and LISE3 [65] at GANIL, or RIPS [66] at RIKEN. The availability of such high beam energies is therefore unprecedented for in-beam $\gamma$-ray spectroscopic studies of exotic nuclei using relativistic Coulomb-Excitation and two-step fragmentation reactions. This implies that emitted $\gamma$-rays are exposed to large Doppler effects, which have to be considered in the design of the RISING $\gamma$-ray detector setup.

The RISING setup consists of three different $\gamma$-ray detector arrays that are placed around the secondary target, as shown in Fig. 4.1, namely

- the Cluster array consisting of 15 former EUROBALL Ge Cluster detectors [67],
- the MINIBALL array consisting of eight MINIBALL Ge detectors [68],
- and the HECTOR array consisting of eight $BaF_2$ detectors [69, 70].

Their basic characteristics and results of Monte Carlo simulations that reveal their performance as a function of $\gamma$-ray energy and beam energy are described in this chapter.

The parameters specifying the performance are energy resolution, photopeak detection efficiency, and the peak-to-total ratio. They are defined as follows:

- The energy resolution of the detectors is the full width at half maximum (FWHM) of a peak distribution divided by the location of the peak centroid.

- The photopeak detection efficiency $\varepsilon_{peak}$ is defined as:

$$\varepsilon_{peak} = \frac{\text{Number of } \gamma\text{-rays detected in photopeak}}{\text{Number of } \gamma\text{-rays emitted by source}}. \tag{4.1}$$

- The peak-to-total ratio $P/T$ is defined as:

$$P/T = \frac{\text{Number of } \gamma\text{-rays detected in photopeak}}{\text{Total number of } \gamma\text{-rays detected}}. \tag{4.2}$$

Before starting the description of the RISING $\gamma$-ray detector setup, the basic interactions of $\gamma$-rays with matter have to be revised because they will be relevant in a later stage.

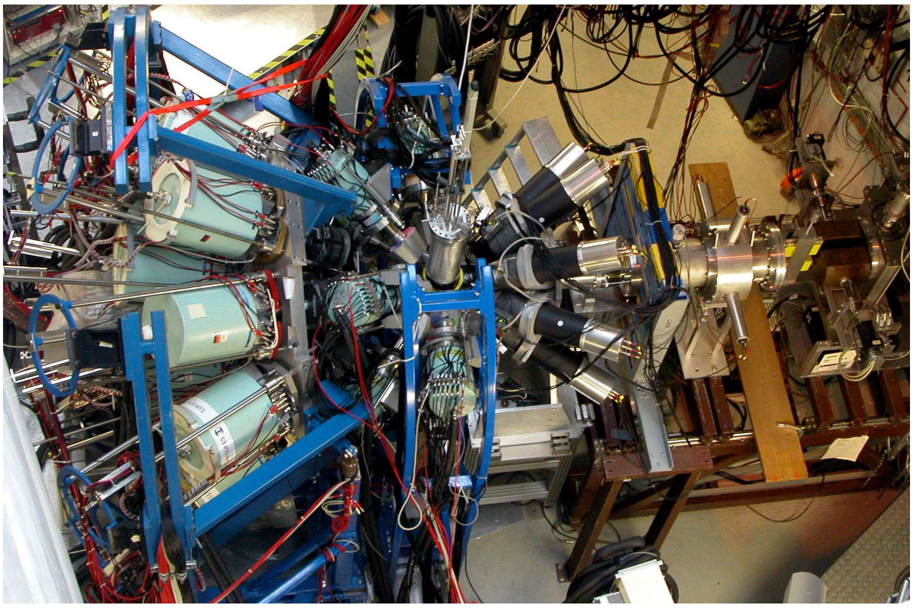

**Figure 4.1:** Photograph of the RISING $\gamma$-ray detectors. All the detectors are put to their closest target distance to allow for the highest possible photopeak detection efficiency.

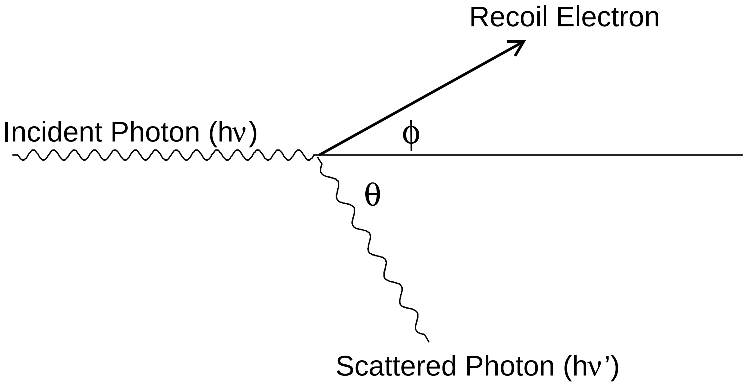

**Figure 4.2:** Illustration of the Compton scattering process. See text for details.

## 4.1 Interaction of $\gamma$-Rays with Matter

Three types of interaction mechanisms play an important role in radiation measurements at $\gamma$-ray energies below 10 MeV: Photoelectric absorption, Compton scattering, and pair production. These processes lead to the partial or complete transfer of the $\gamma$-ray energy to electron energy, which can be measured by the $\gamma$-ray detectors. In the process of a photoelectric absorption an incoming $\gamma$-ray is completely absorbed by the interacting atom. In exchange, a photoelectron is ejected by the atom from one of its bound shells and its energy is given by:

$$E_{e^-} = h\nu - E_b, \tag{4.3}$$

with $E_b$ being the binding energy of the photoelectron in its original shell. The vacancy that is created in the electron shell is quickly filled by an electron rearrangement, which liberates its binding energy in the form of a characteristic X-ray or Auger electron. The Auger electron has a short range because of its low energy, while the X-ray is reabsorbed through photoelectric interactions with less tightly bound electron shells of the absorber atoms. The sum of the energies of the created electrons corresponds to the original $\gamma$-ray energy and is therefore the ideal process to measure $\gamma$-ray transition energies. However, this process is predominant only for low energy $\gamma$-rays.

For higher energies the Compton scattering process as illustrated in Fig. 4.2 gains in importance. In this process the $\gamma$-ray with the initial energy $h\nu$ is scattered by an angle

$\theta$ with respect to its original direction. The $\gamma$-ray transfers a portion of its energy to the recoil electron and keeps the energy $h\nu'$ according to the formula:

$$h\nu' = \frac{h\nu}{1 + \frac{h\nu}{m_0c^2}(1 - \cos\theta)}, \tag{4.4}$$

where $m_0c^2$ is the rest mass energy of the electron (511 keV). For all scattering angles $\theta$ some of the original energy is retained. The head-on collision $\theta = \pi$ represents the maximum energy that can be transferred to an electron in a single Compton scattering interaction. For this case the electron energy becomes:

$$E_{e^-}(\theta = \pi) = h\nu \frac{2h\nu/m_0c^2}{1 + 2h\nu/m_0c^2}. \tag{4.5}$$

The integral over all scattering angles results in a continuum of energies transferred to the electron ranging from zero up to the Compton edge energy of Eq. 4.5, where the $\gamma$-ray may scatter out of the detector without further interactions.

The third significant $\gamma$-ray interaction is pair production. This process corresponds to the creation of an electron-positron pair in the field of the nucleus of the absorbing material, while the incident $\gamma$-ray photon completely disappears. For this interaction a minimum energy of 1022 keV ($2m_0c^2$) is required. If the $\gamma$-ray energies exceed this value, the energies between the electron and positron are shared according to the formula:

$$E_{e^+} + E_{e^-} = h\nu - 2m_0c^2. \tag{4.6}$$

The positron can annihilate with one of the electrons of the absorbing material and produces thereby two annihilation $\gamma$-rays of an energy $m_0c^2 = 511$ keV. If one or both $\gamma$-rays escape without further interactions with the absorbing material, a single-escape or double-escape peak is visible in the detectors energy spectrum at energies of 511 keV and 1022 keV below the photopeak energy, respectively.

## 4.2 The RISING $\gamma$-Ray Detection Setup

As the RISING Fast Beam setup is designed to measure photons in flight at beam velocities $\beta \geq 0.4$, i.e. at energies of 100 $A$ MeV and more, the relevant formulas for the Doppler

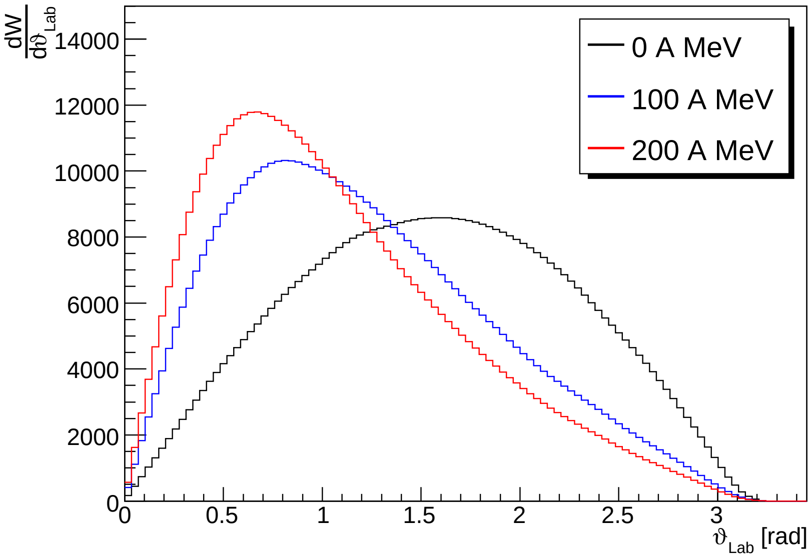

**Figure 4.3:** Polar angle $\vartheta_\gamma$ distributions in the laboratory system for different heavy ion energies.

effect [71, 72] have to be summarised. Due to the large beam velocity the observed $\gamma$-ray energies $E_\gamma$ are strongly Doppler shifted relative to the $\gamma$-ray energy $E_{\gamma 0}$ in the rest coordinate system according to the formula:

$$E_\gamma = E_{\gamma 0} \frac{\sqrt{1-\beta^2}}{1-\beta\cos\vartheta_\gamma}, \tag{4.7}$$

where $\vartheta_\gamma$ is the angle between the $\gamma$-ray and the projectile in the laboratory frame.

In the rest coordinate system a photon is characterised by the polar and azimuthal angles $\theta_\gamma$ and $\phi_\gamma$, respectively. In the laboratory system these angles are denoted by $\vartheta_\gamma$ and $\varphi_\gamma$. Since in both the laboratory and the rest frame the Z-axis is the beam direction, the following relations between the $\gamma$-ray emission angle and the solid angle are obtained [71]:

$$\phi_\gamma = \varphi_\gamma, \tag{4.8}$$

$$\cos\theta_\gamma = \frac{\cos\vartheta_\gamma - \beta}{1-\beta\cos\vartheta_\gamma}, \tag{4.9}$$

$$\frac{d\Omega_{rest}}{d\Omega_{lab}} = \left(\frac{E_\gamma}{E_{\gamma 0}}\right)^2 = \frac{1-\beta^2}{(1-\beta\cos\vartheta_\gamma)^2}, \tag{4.10}$$

where $d\Omega_{rest} = \sin\theta_\gamma d\theta_\gamma d\phi_\gamma$ and accordingly $d\Omega_{lab} = \sin\vartheta_\gamma d\vartheta_\gamma d\varphi_\gamma$. As the relation between the solid angles is given by the square of the Doppler shift, the $\gamma$-ray intensity distribution is peaked at forward angles, as shown in Fig. 4.3 for different beam energies. If the $\gamma$-ray detectors are installed at these angles, the $\gamma$-ray detection efficiency increases. However, the $\gamma$-rays must be detected at higher energies. This diminishes the gain in $\gamma$-ray efficiency.

To get the $\gamma$-ray transition energy $E_{\gamma0}$ in the rest frame of the de-exciting nuclei, the observed energy $E_\gamma$ needs to be corrected for the Doppler shift. Therefore, $E_\gamma$, $\beta$, and $\vartheta_\gamma$ have to be determined precisely. The uncertainty of the emission angle $\Delta\vartheta_\gamma$ is governed by the opening angle of the $\gamma$-ray detectors. The trajectory of the $\gamma$-ray emitting nuclei can be measured very accurately by the Si detector at the secondary target and the Si detectors from the CATE array. This leads to the Doppler broadening due to the opening angle of the $\gamma$-ray detector:

$$\frac{\Delta E_{\gamma0}}{E_{\gamma0}} = \frac{\beta\sin\vartheta_\gamma}{1-\beta\cos\vartheta_\gamma}\Delta\vartheta_\gamma. \tag{4.11}$$

The equation shows that for a given detector position and opening angle the energy resolution deteriorates with increasing velocity $\beta$.

Radioactive beams experiments which are performed at relativistic energies can partially counterbalance their low beam intensities by choosing thick targets. This implicates that the heavy ions undergo an energy loss while penetrating the target and eventually leads to an uncertainty $\Delta\beta$ of the heavy ions' velocity at the moment of $\gamma$-radiation emittance. The degree of uncertainty is determined by the lifetimes of the excited states, the target thickness, the beam velocity, and the energy loss in the target. The equation for the Doppler-broadening due to $\Delta\beta$ is given by:

$$\frac{\Delta E_{\gamma0}}{E_{\gamma0}} = \frac{\beta-\cos\vartheta_\gamma}{(1-\beta^2)(1-\cos\vartheta_\gamma)}\Delta\beta. \tag{4.12}$$

These formulas are considered in the design of the RISING array in order to find the optimal positions for the $\gamma$-ray detectors. All three $\gamma$-ray detection systems are now described individually.

### 4.2.1 The Cluster Array

In total 15 Cluster detectors from the former EUROBALL spectrometer [73, 74] are the basis of the RISING array. Each Cluster detector comprises seven closely packed tapered hexagonal Ge crystals (70 mm diameter and 78 mm in length before shaping), housed in a permanently sealed Al can. In case of Compton scattering the individually measured energies of a Cluster detector are added back. Therefore, high $\gamma$-ray detection efficiencies are maintained up to several MeV [75]. The Cluster detectors are thus best suited to be placed at extreme forward angles relative to the secondary target, where the $\gamma$-rays are Doppler shifted to the highest energies. The large size of the crystals would have caused a large Doppler broadening if the detectors were mounted too close to the reaction target. On the other hand, the efficiency reduces with the square of the distance to the target. A compromise is found by putting the Cluster detectors in three rings around the beam pipe at angles of 16°, 33°, and 36° with variable distances of 700 to 1400 mm. In the close geometry configuration this leads to a calculated performance of an energy resolution of 1.56 % and a photopeak detection efficiency of $\varepsilon_{peak} = 2.81$ % for a 1332.5 keV $\gamma$-ray emitted from a moving nucleus at 100 $A$ MeV ($\beta = 0.43$) [4]. This has to be compared with a measured energy resolution at rest of 0.2 % (2.6 keV) from a $^{60}$Co calibration source.

For the energy calibration of the Cluster detectors also $\gamma$-rays emitted from $^{152}$Eu and $^{16}$O are used. The $3_1^- \rightarrow 0_{g.s.}^+$ transition in $^{16}$O decays with a $\gamma$-ray energy of 6130 keV. This transition is produced with a composite calibration source of $^{13}$C and the $\alpha$-emitter $^{238}$Pu according to the reaction $^{13}$C($\alpha$,n$\gamma$)$^{16}$O. After applying a linear energy calibration a deviation of less than 200 eV compared to the literature values [15] is obtained for observed $\gamma$-ray transitions in $^{16}$O, $^{60}$Co, and $^{152}$Eu.

To reduce the background originating from heavy ion induced reactions other than the secondary target and atomic background produced in the slowing down process inside the target, every Cluster detector is shielded at the sides with 2 mm of lead, at the back with 5 mm of lead, while the frontside is covered with a stacked combination of 1 mm lead, 2 mm tin, and 2 mm aluminium absorbers.

The Cluster detectors signals are processed and digitised by the VXI Cluster cards which provide energy ranges of 4 and 20 MeV and a $\gamma$-ray timing signal with respect to the VXI trigger. A detailed description of the VXI electronic system can be found in Ref. [76].

The Cluster array's $\gamma$-ray multiplicity and the detector's coordinates (r, $\vartheta$, $\varphi$) for the Doppler correction are defined in the following way:

- A photopeak event has a Ge crystal multiplicity equal to one (single hit). For this case the interaction point, necessary to determine $\vartheta_\gamma$, is given by the coordinates of the centroid of the Ge crystal that detected the $\gamma$-ray.
- Compton scattering events are validated only if one detector (7 crystals) has a crystal multiplicity equal to two. For this case the $\gamma$-ray energies of the two crystals are added (add-back). The interaction point is given by the coordinates of the centroid of the Ge crystal which detected the highest $\gamma$-ray energy.

### 4.2.2 The MINIBALL Array

The MINIBALL array is formed by a total of 24 6-fold segmented individually encapsulated crystals. Besides the segmentation, the geometry of a single MINIBALL crystal, shown in Fig. 4.4, corresponds exactly to the Cluster crystal geometry. A MINIBALL detector is composed out of three such crystals, thus also enabling the utilisation of add-back procedures. They are mounted in the RISING setup in two rings at central angles of 51° and 86°. The distance to the target can be varied individually between 200 and 400 mm. To shield the MINIBALL detectors from atomic background produced in the slowing down process of heavy ions inside the target, the exterior of the beam pipe is covered with 1 mm lead and 2 mm tin. A linear energy calibration is applied for $\gamma$-ray transitions from the $^{16}$O, $^{60}$Co, and $^{152}$Eu calibration sources. All $\gamma$-ray transitions included in the fit deviate less than 250 eV from the corresponding literature value. An energy resolution of 0.22 % (2.9 keV) is measured for the MINIBALL array at a $\gamma$-ray energy of 1332.5 keV.

The MINIBALL array's $\gamma$-ray multiplicity and the detector's coordinates (r, $\vartheta$, $\varphi$) for the Doppler correction are defined in the following way:

- A photopeak event corresponds to a segment multiplicity equal to one in the total array. The interaction point is given by the coordinates of the segment that detected the $\gamma$-ray. The $\gamma$-ray energy for the Doppler correction is taken from the central contact of the crystal.

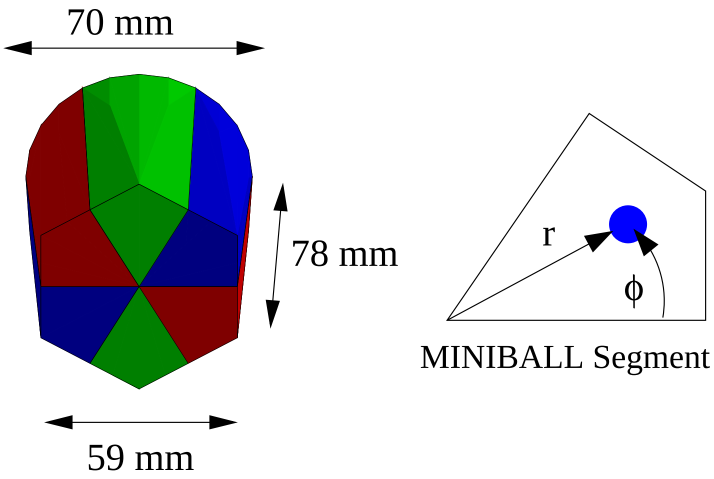

**Figure 4.4:** Schematic drawing of a MINIBALL Ge crystal. Within a segment the radius $r$ and the angle $\varphi$ can be extracted by PSA algorithms.

- A Compton scattering event is restricted to events of a segment multiplicity equal to two in a MINIBALL triple detector. In the case the interaction takes place within one crystal the $\gamma$-ray energy is used from the central contact, otherwise the individual energies are added up. The interaction point is given by the coordinates of the centroid of the segment with the highest $\gamma$-ray energy.

The signals from each segment as well as from the central core are read out individually and passed to an electronic readout using XIA DGF-4C modules [77]. Here, the preamplified signals are digitised by a 12-bit flash ADC with a sampling frequency of 40 MHz, which corresponds to a sampling distance of 25 ns. These signals can be used in real-time for pulse shape analysis (PSA) algorithms, well described in Ref. [78].

Using PSA algorithms augments the effective granularity of the MINIBALL detector, yet they are restricted to events where $\gamma$-rays interacted solely in one segment. For high energy $\gamma$-rays the full energy peak is mostly attained by $\gamma$-rays scattering across at least two segments. Events where the $\gamma$-ray deposits energy in only one segment, however, are dominated by the single-, double-escape, and Compton scattering interactions. Therefore, PSA algorithms are not used for the $2_1^+ \rightarrow 0_{g.s.}^+$ decay in $^{36}$Ca. Nevertheless, they are tested for other reaction channels observed in CATE. Hence, a short description of the pulse shape analysis with the MINIBALL detectors is given. More detailed explanations can be found in Refs. [78, 79, 80].

### Pulse Shape Analysis with the MINIBALL Detectors

With the PSA algorithms the $r$ and $\phi$ coordinates shown in the right of Fig. 4.4 can be determined for the main interaction (MI). It is assumed that this is the point where also the first interaction (FI) occurs. That this assumption is permissible has been shown by means of simulations [79].

The steepest slope algorithm [80] provides the radial distance $r$ of the MI. In the vicinity of a $\gamma$-ray interaction the created electron-hole pairs drift to the electrodes of the Ge crystal (the electrons to the central contact and the holes to the outer segments). When the electrons reach the central contact at the steepest slope time $T_{ss}$ the induced current in the crystal drops immediately. Because the drift velocity of the electrons is roughly constant, $T_{ss}$ yields for the MI radius

$$r = r_0 + r_1 \cdot T_{ss}, \tag{4.13}$$

where $r_0$ and $r_1$ are the coefficients of a linear function that has been determined experimentally [78].

When a $\gamma$-ray deposits the energy of its MI in the segment $n$, it induces mirror charges in the neighboring segments $n-1$ and $n+1$. The angle $\phi$ is then determined from the maximum amplitude of the mirror charge signal in those segments. To overcome the radial dependence on the absolute values of the induced charge, the logarithmic ratio of the mirror charge is used [79], thus yielding for the azimuthal angle

$$\phi = \phi_0 + \phi_1 \cdot \log\left(\frac{|q_-|}{|q_+|}\right), \tag{4.14}$$

with $|q_-|$ and $|q_+|$ being the heights of the induced charge in the neighboring segments. The coefficients $\phi_0$ and $\phi_1$ have been determined experimentally [78].

## 4.2.3 The HECTOR Array

The HECTOR array consists of eight large $BaF_2$ scintillating crystals which have a length of 175 mm and a diameter of 145 mm. The front half of each $BaF_2$ crystal possesses a tapered geometry that begins with a diameter of 100 mm and merges with the 145 mm diameter of the cylindrical shape of the second half. To reduce atomic background contributions, the crystals are surrounded on the front side by 3 mm of lead (also 1 mm or 6 mm can be used optionally), while for the sides 6 mm of lead are used.

The energy resolution of the $BaF_2$ detectors is in the order of 10 % for the $^{60}$Co lines at 1173.2 and 1332.5 keV. For the 6130 keV $\gamma$-ray transition of $^{16}$O an energy resolution of 8(1) % is measured. After a linear calibration from the $^{16}$O and $^{60}$Co sources it is possible to determine the energy of observed $\gamma$-ray lines with an accuracy of 20 keV.

The $BaF_2$ detectors have also internal radiation arising from radium contaminations emitting $\alpha$-particles. To distinguish these from $\gamma$-rays produced with a secondary target reaction, the dependence on the relative intensities of the two scintillation components of $BaF_2$ (220 nm and 320 nm) on the type of interaction is taken advantage of by an analysis of the pulse shape [69]. This is achieved by integrating the fast component over a gate of several tens of ns while the entire pulse is integrated over a range of 1 $\mu$s.

In comparison to the Ge detectors the big advantage of the HECTOR array is its intrinsic time resolution below 1 ns due to the very fast $BaF_2$ scintillation material. This permits to determine the origin of background radiation in the RISING experiments produced in other sources than the secondary target. For the RISING setup six $BaF_2$ detectors are placed at backward angles of 142° and two at an angle of 86°, all at a distance of 350 mm to the secondary target.

## 4.3 Monte Carlo Simulations of the RISING $\gamma$-Ray Detection Setup

For the $\gamma$-spectroscopy of fragmentation products from a secondary $^{37}$Ca beam a multitude of $\gamma$-rays from various reaction products are emitted. Especially the interesting $2_1^+ \rightarrow 0_{g.s.}^+$ decay in $^{36}$Ca is expected around 3 MeV, implying that energies of up to 5 MeV in the laboratory frame need to be measured for the detectors at extreme forward angles and at a beam energy above 100 $A$ MeV. Thus, the energy spectra of the $\gamma$-ray detectors are expected to be composed of Compton scattering and pair production interactions with single- and double-escape events. Therefore, the RISING $\gamma$-ray energy resolutions and efficiencies for all three detector systems are studied with Monte Carlo simulations using ROOT [81] and GEANT4 [82]. An important aspect of the studies is the influence of the secondary beam energy and target thickness on the detector response.

### 4.3.1 Simulation Sequence

The Monte Carlo simulations are executed in three steps. In the first step a heavy ion beam strikes on a target. The relevant beam parameters as spatial width, position, and beam directions are inserted into the event. A reaction is simulated uniformly distributed within the target. The momentum spread after the fragmentation reaction is introduced according to Eq. 3.1 and the mean kinetic energy is calculated by Eq. 3.2. It is assumed that the fragmentation cross-section is independent of the beam energy. This has been verified in the energy range of 200 $A$ MeV $\leq E_{proj} \leq$ 1500 $A$ MeV [83]. For lower beam energies the experimental data are less well determined and may affect the significance of the simulations at the very low energy range $E_{proj} \leq$ 100 $A$ MeV.

After the reaction the nuclei are excited to fixed values of excitation energy, which are inserted into the simulations together with the excitation probability and lifetime of the excited state as input parameters. The excited states emit the $\gamma$-rays isotropic in the rest system, which causes a shift towards forward $\vartheta_\gamma$ angles in the laboratory system, as shown in Fig. 4.3 for different beam energies. At the end of the first step, the results of the simulations are written event-by-event into a ROOT-tree.

In the second step the events from the first step are used in combination with the RISING detector setup, shown in Fig. 4.5, including the target, the beam pipe of 5 mm thick aluminium, the CATE array, and the $\gamma$-ray detectors. The position of all $\gamma$-ray detectors correspond to the configuration in the experiment: distances to the secondary target of 700 to 725 mm for the Cluster detectors, 200 to 250 mm for the MINIBALL detectors, and 350 mm for the HECTOR detectors. The shielding of $\gamma$-radiation below 200 keV consists of 1 mm Pb, 2 mm Sn, and 2 mm Al for the Cluster detectors, while 1 mm Pb, and 2 mm Sn are placed in front of the MINIBALL detectors. Since these materials partially absorb also high energy $\gamma$-radiation, they are included in the simulations as well. The detectors' intrinsic energy, time, and position resolutions are not simulated. Thus, they are provided as input parameters. The values used in the simulations are given in Tab. 4.1. In the second step the information from step one is extended and written into a new ROOT-tree together with the deposited energy in CATE and the $\gamma$-ray detector information.

In the third and final step the second ROOT-tree is read out and a Doppler correction is applied to the registered $\gamma$-rays. This step has a big similarity to the final, real analysis

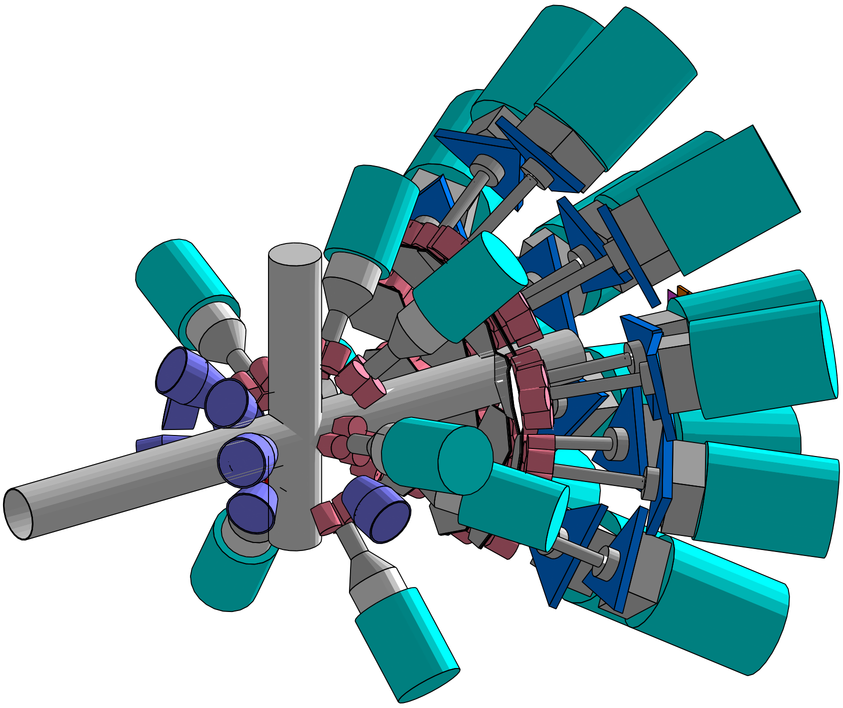

**Figure 4.5:** Geometry for the Monte Carlo simulations of the RISING setup. All relevant detectors and the beam pipe are shown.

of the experimental data. For example the change of energy resolution with and without tracking or using a constant or an event-by-event $\beta$ can be investigated.

In order to get a realistic value for the $\gamma$-ray efficiency $\varepsilon_{peak}$ and the energy resolution for the different $\gamma$-ray detectors as a function of heavy ion energy, a $\gamma$-ray transition of 1332.5 keV is simulated for beam energies ranging from 100 to 300 $A$ MeV. Also for different $\gamma$-ray energies and constant beam velocities the energy resolution and efficiency $\varepsilon_{peak}$ are investigated. Therefore, $\gamma$-ray transitions with energies between 250 and 3000 keV are simulated for three heavy ion energies of 100, 150 and, 200 $A$ MeV. By varying the target thickness and lifetime for constant beam velocities and $\gamma$-ray transition energies the influence on the energy resolution, lineshape, and peak position can be examined. Results of these studies are compared to experimental results in Ch. 7.

The RISING $\gamma$-ray detection array has been simulated also for experiments that implant the fragment of interest into a stopper. Details can be found in App. B.

| Detector | Resolution (FWHM) |
|---|---|
| Cluster Energy | 0.19 % |
| MINIBALL Energy | 0.19 % |
| HECTOR Energy | 10.0 % |
| Si Position | 5.0 mm |
| Si Energy | 2.5 % |
| CsI Energy | 2.0 % |
| $\beta$ (TOF) | 0.2 % |

**Table 4.1:** Intrinsic energy, time, and position resolutions used in the simulations. For the Ge detectors an energy resolution of 2.5 keV is assumed for a $\gamma$-ray of 1332.5 keV.

### 4.3.2 $\gamma$-Ray Efficiency and Energy Resolution of the RISING Setup at 1332.5 keV

For the energy resolution and efficiency $\varepsilon_{peak}$ simulation for a $\gamma$-ray energy of 1332.5 keV the $\gamma$-ray is emitted in the centre of an infinitesimal thin target. The $\gamma$-ray spectra of the Cluster, MINIBALL, and HECTOR detectors for beam velocities of 100 *A* MeV are shown in Fig. 4.6 (left panels). Without Doppler correction two broad distributions are visible for the Cluster detectors at energies of more than 2 MeV. The higher one originates from the more forward detector ring at 16°, the lower one from the two rings at 33° and 36°, respectively. For the MINIBALL array the situation is worse. As the detectors are located very close to the target, a bigger $\vartheta_\gamma$ angle distribution is covered, resulting in a huge energy spread of measured $\gamma$-ray energies. For the HECTOR array also two broad distributions are visible, similar to the Cluster detectors. After applying the Doppler correction these broad lines merge into a single peak at 1332.5 keV, the emitted $\gamma$-ray energy in the moving system of the beam. This is displayed in the right panels for all three detectors branches.

The simulation results for the efficiency $\varepsilon_{peak}$ and the energy resolution for beam energies between 100 and 300 *A* MeV are displayed in Fig. 4.7 and Fig. 4.8. An increase in beam energy barely raises the $\varepsilon_{peak}$ of a combined high energy resolution array, Cluster and MINIBALL, which remains at about 5 %. The given efficiencies include add-back events if the $\gamma$-ray scattered within crystals of the same detector. For the MINIBALL array the position information from the crystals' segments is used to perform the Doppler correction. For the HECTOR array the efficiency $\varepsilon_{peak}$ reduces from 1.5 % to 1.0 %, as expected for an array placed mainly at backward angles.

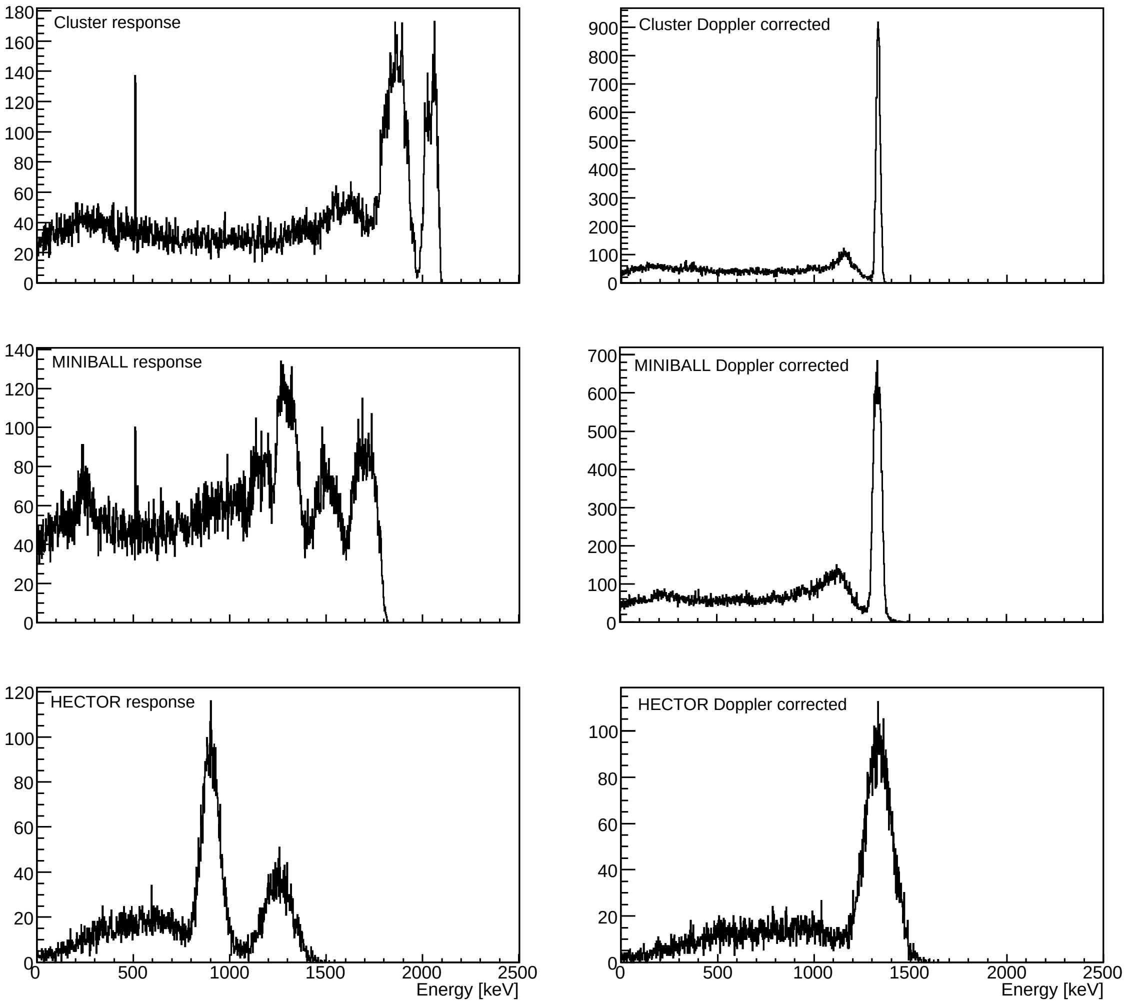

**Figure 4.6:** Comparison of the three simulated $\gamma$-ray detector branches before and after applying a Doppler correction. The $\gamma$-rays are emitted from a moving source at a heavy ion energy of 100 $A$ MeV ($\beta = 0.43$).

The energy resolution deteriorates from 2 % to 4 % for the Cluster and from 3 % to 6 % for the MINIBALL array, respectively, when going from a beam energy of 100 $A$ MeV to 300 $A$ MeV. For the HECTOR array the energy resolution is dominated by its intrinsic resolution of 10 % and ranges from 11.6 % at 100 $A$ MeV to 13.5 % at 300 $A$ MeV. Hence, experiments performed at 100 $A$ MeV would be best suited for the RISING setup if $\gamma$-rays are emitted from an infinitesimal thin target. Smaller heavy ion energies are not desirable because the FRS is not designed for such beam energies.

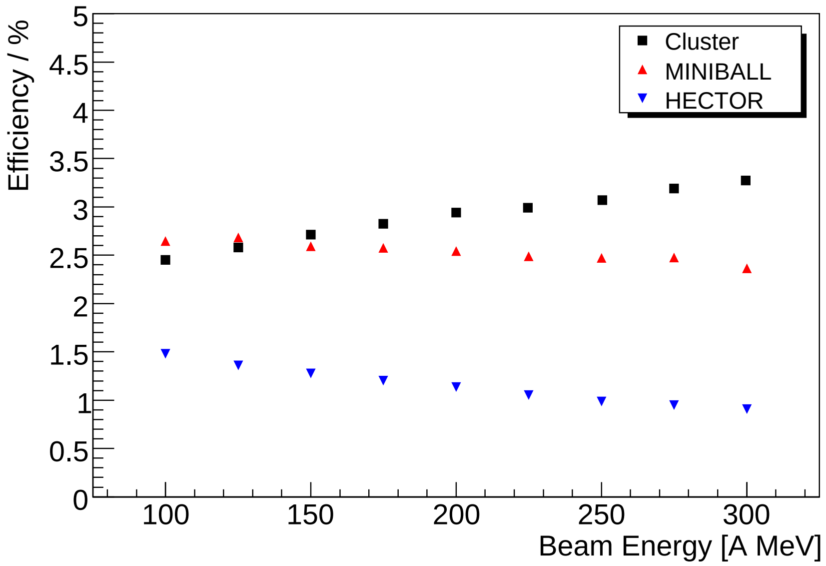

**Figure 4.7:** Simulated $\gamma$-ray efficiency $\varepsilon_{peak}$ for a 1332.5 keV $\gamma$-ray and beam energies between 100 and 300 *A* MeV.

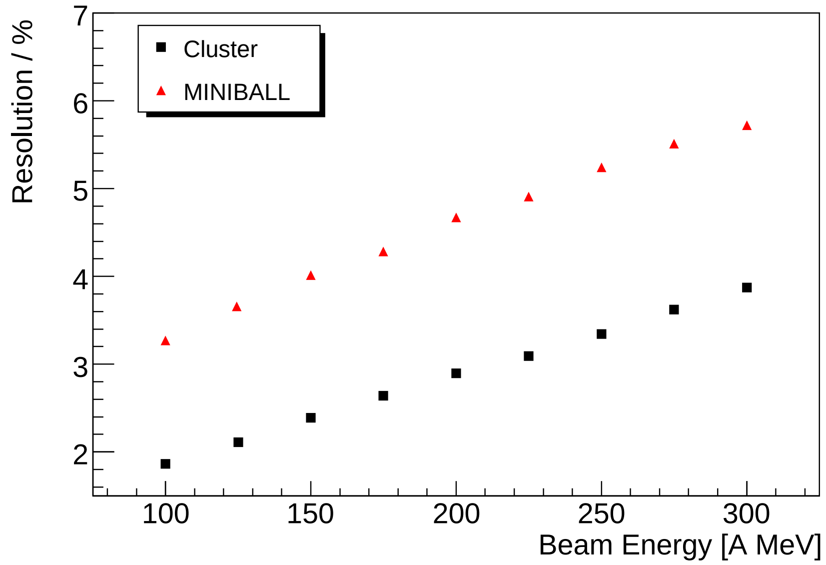

**Figure 4.8:** Simulated energy resolution for a 1332.5 keV $\gamma$-ray and beam energies between 100 and 300 *A* MeV. For the HECTOR array, not shown in this plot, the energy resolution increases from 11.6 % to 13.5 %.

### 4.3.3 $\gamma$-Ray Efficiency and Energy Resolution of the RISING Setup at 100 $A$ MeV

The energy resolution and efficiency $\varepsilon_{peak}$ at a beam energy of 100 $A$ MeV and varying $\gamma$-ray energies between 250 and 3000 keV are plotted in Fig. 4.9 and Fig. 4.10 in steps of 250 keV. The highest efficiency $\varepsilon_{peak}$ is obtained for $\gamma$-rays at 500 keV. For lower energy values the $\gamma$-ray efficiency diminishes due to the atomic background absorbers put in front of the detectors and the beam pipe. With increasing $\gamma$-ray energy the energy resolution is slightly improving for all three $\gamma$-ray detector branches, as shown for the Cluster and MINIBALL arrays in Fig. 4.10. This is due to the fact that more interactions are necessary to release the full energy with increasing $\gamma$-ray energy. For a first $\gamma$-ray interaction away from the detector's centre the probability is then higher to scatter out of the detector. Thereby, the detectors effective opening angles decrease and lead to a better energy resolution. The simulation results for beam energies of 150 and 200 $A$ MeV can be seen in App. A.

The RISING setup can also be used in a distant configuration if the Cluster detectors are positioned at a distance of 1400 mm and the MINIBALL array at a distance of 400 mm to the secondary target. The performance of this geometry is simulated for a beam energy of 100 $A$ MeV. In Fig. 4.11 the Doppler corrected Cluster array response is compared for the two distances, denoted as close and far, respectively. Increasing the distance by a

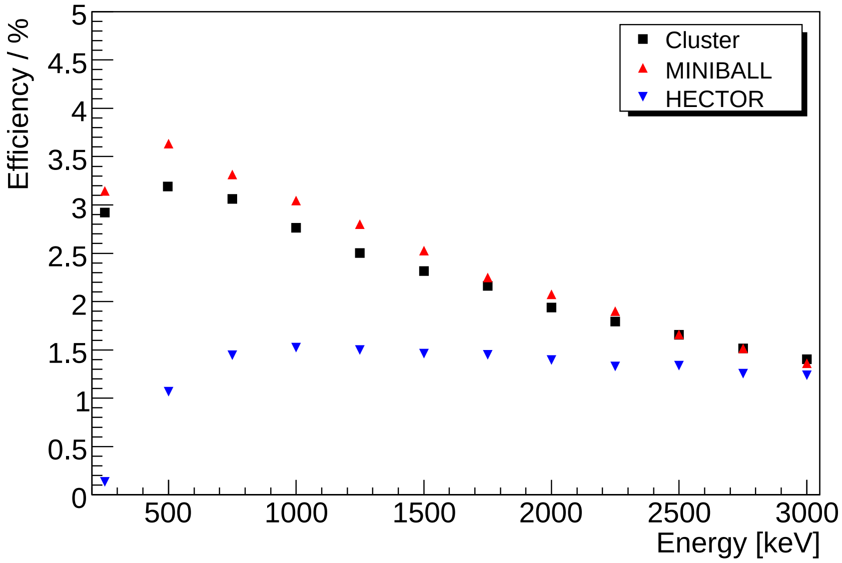

**Figure 4.9:** Simulated $\gamma$-ray efficiency $\varepsilon_{peak}$ at a beam energy of 100 $A$ MeV.

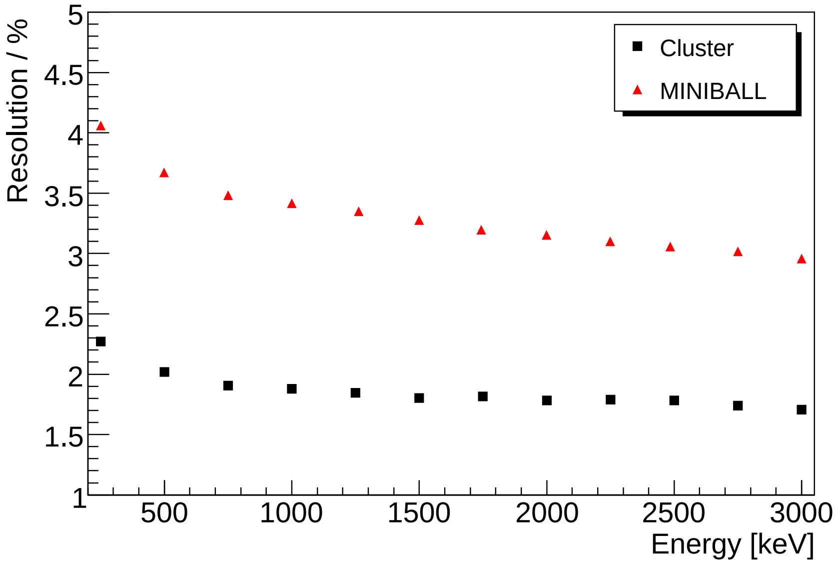

**Figure 4.10:** Simulated energy resolution at a beam energy of 100 *A* MeV for the Ge detector systems.

factor of two reduces the peak integral by a factor of 4, as expected. At the same time the energy resolution improves by a factor of two, so that the peak height is halved. The situation is exactly the same for the MINIBALL detectors, displayed in Fig. 4.12, though with a different starting efficiency $\varepsilon_{peak}$ and energy resolution. From these two figures it is concluded that the close geometry is the preferred choice to measure $\gamma$-ray decays from excited states in $^{36}$Ca, as the production yield of this nucleus is expected to be small. All simulation results for the close and far geometry and the individual detector rings for all three $\gamma$-ray detector branches are summarised in Tab. 4.2.

The $\gamma$-ray intensity increases linearly with the secondary target thickness if secondary reactions are neglected and the cross sections are assumed to be constant. Therefore, one is interested to chose the secondary target as thick as possible to compensate for the low beam intensity. But doing this, the energy loss in the secondary target and especially for fragmentation experiments the lifetime of an excited state compared to the transit time of the nucleus through the target must be included. For the nucleus $^{36}$Ca the lifetime of the first excited $2^+$ is expected to be well below 1 ps (as can be deduced from its mirror nucleus) and the time of flight through a thick Be target (300–700 mg/cm$^2$) is at least one magnitude longer at beam energies between 130 and 200 *A* MeV. Thus, lifetime effects can be neglected and the velocity distribution at the moment of $\gamma$-ray emission is dominated

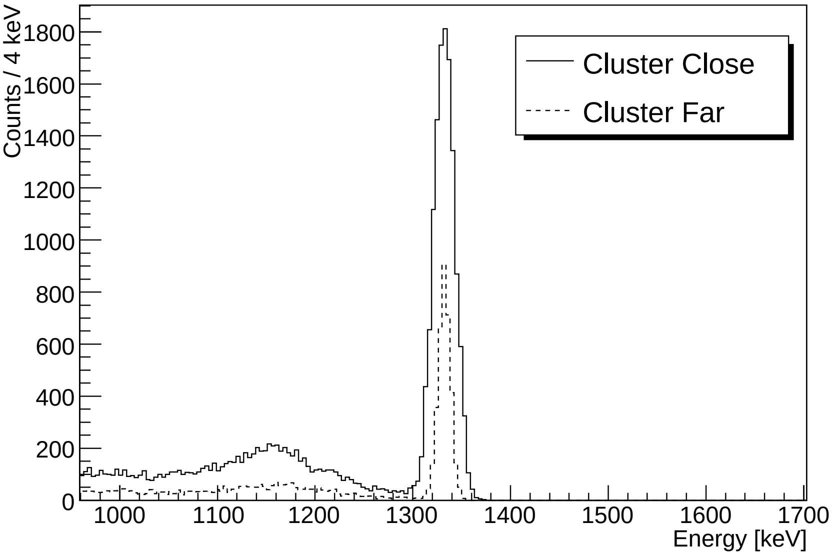

**Figure 4.11:** Simulated Doppler corrected $\gamma$-ray spectrum for the Cluster array installed in the close (solid line) and far geometry (dashed line) setup. The $\gamma$-ray energy is set to 1332.5 keV and the beam energy to 100 *A* MeV.

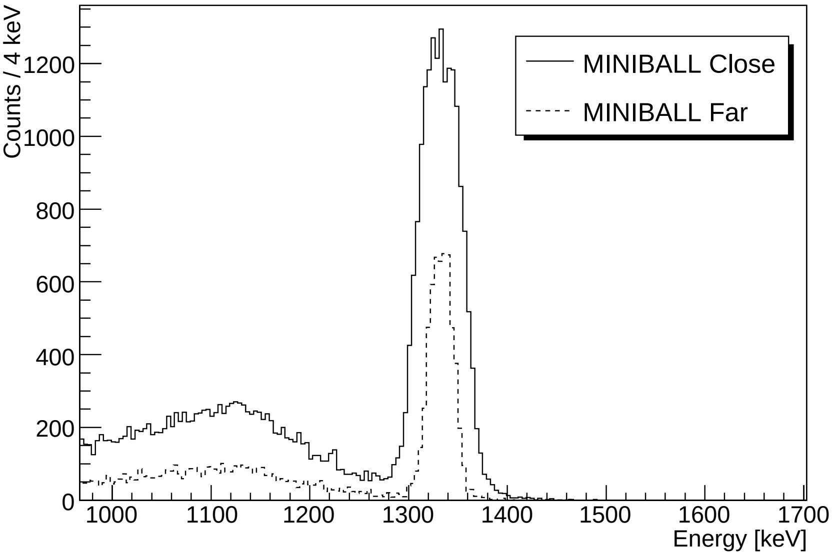

**Figure 4.12:** Simulated Doppler corrected $\gamma$-ray spectrum for the MINIBALL array installed in the close (solid line) and far geometry (dashed line) setup. The $\gamma$-ray energy was set to 1332.5 keV and the beam energy to 100 *A* MeV.

by the energy loss function of the secondary beam in the secondary target. Nevertheless, interesting phenomena arise from the lifetime of an excited state. Thefore, Ch. 7 is devoted

| Detector | Angle | Close geometry | | Far geometry | |
|---|---|---|---|---|---|
| | | $\varepsilon_{peak}$ [%] | Resolution [%] | $\varepsilon_{peak}$ [%] | Resolution [%] |
| Cluster | 16° | 0.87 | 1.46 | 0.24 | 0.94 |
| Cluster | 33° | 0.81 | 1.98 | 0.23 | 1.23 |
| Cluster | 36° | 0.77 | 2.11 | 0.23 | 1.28 |
| Cluster | Total | 2.45 | 1.86 | 0.69 | 1.12 |
| MINIBALL | 51° | 1.64 | 3.36 | 0.55 | 2.02 |
| MINIBALL | 85° | 1.05 | 3.22 | 0.35 | 1.97 |
| MINIBALL | Total | 2.69 | 3.32 | 0.90 | 2.01 |
| HECTOR | 85° | 0.58 | 12.8 | | |
| HECTOR | 142° | 0.94 | 11.3 | | |
| HECTOR | Total | 1.52 | 11.6 | | |

**Table 4.2:** Simulated performance comparison between the close and far geometry of the Cluster and MINIBALL detector arrays for 1332.5 keV $\gamma$-rays de-exciting at a beam energy of 100 $A$ MeV.

to the investigation of lifetime effects for high resolution $\gamma$-ray detection at relativistic energies.

### 4.3.4 Selecting the Most Suitable Secondary Target Thickness and Beam Energy

For a given secondary target thickness the spread in velocity reduces if the beam energy is increased. This implicates that $\gamma$-ray energies up to more than 5 MeV are measured for the Cluster detectors in the laboratory frame for a beam energy of 200 $A$ MeV, assuming a transition energy of $E_{\gamma 0} = 3$ MeV. In order to find the ideal beam energy striking on the secondary target, a $\gamma$-ray decay in $^{36}$Ca with an energy of $E_{\gamma 0} = 3$ MeV is simulated for different secondary $^{37}$Ca beam energies of 130, 150, and 195.7 $A$ MeV and secondary target thicknesses of 300, 500, and 700 mg/cm$^2$ Be, respectively. The simulated secondary beam yield given in Tab. 3.2 is accounted for. Moreover, for all beam energies the $^{37}$Ca energy width is kept at 6 $A$ MeV (FWHM). For the case of a 195.7 $A$ MeV secondary beam striking on a 700 mg/cm $^2$Be target a total of 7 $\times 10^5$ $\gamma$-rays of an energy of $E_{\gamma 0} = 3$ MeV are generated and the other cases are scaled proportionately.

Increasing the secondary target thickness produces a higher yield for the $^{36}$Ca fragment but deteriorates the $\beta$-definition at the moment of decay. This is exemplified in

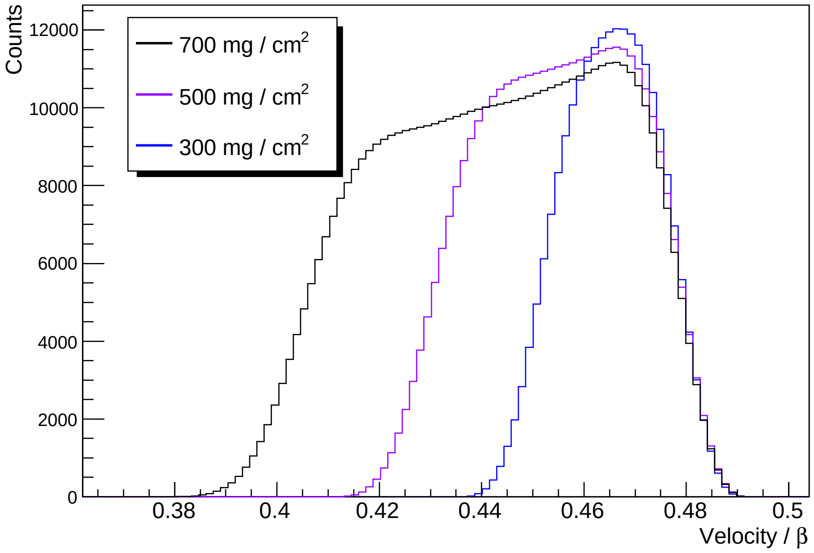

**Figure 4.13:** Simulated velocity distribution at the moment of a prompt $\gamma$-ray decay after the production of $^{36}$Ca. The values are plotted for an incoming kinetic energy of 130 *A* MeV and different $^{9}$Be secondary target thicknesses (300, 500, and 700 mg/cm$^2$).

| Beam Energy [*A* MeV] | Detector | Target Thickness<br>300 mg/cm$^2$<br>Yield | <br><br>Res. [%] | <br>500 mg/cm$^2$<br>Yield | <br><br>Res. [%] | <br>700 mg/cm$^2$<br>Yield | <br><br>Res. [%] |
|---|---|---|---|---|---|---|---|
| 130 | Cluster | 1.13 | 3.4 | 1.85 | 3.8 | 2.25 | 5.3 |
| 130 | MINIBALL | 1.00 | 3.4 | 1.69 | 3.6 | 2.36 | 3.9 |
| 150 | Cluster | 1.17 | 2.7 | 1.99 | 3.5 | 2.74 | 4.2 |
| 150 | MINIBALL | 1.04 | 3.8 | 1.80 | 3.8 | 2.42 | 3.8 |
| 195.7 | Cluster | 1.62 | 3.1 | 2.61 | 3.4 | 3.33 | 3.6 |
| 195.7 | MINIBALL | 1.19 | 4.3 | 2.12 | 4.4 | 3.17 | 4.5 |

**Table 4.3:** Simulation results of relative yields and energy resolution for a $\gamma$-ray energy $E_{\gamma 0} = 3$ MeV measured with the Cluster and MINIBALL detectors. The results are given for secondary beam energies of 130, 150, and 195.7 *A* MeV and secondary target thicknesses of 300, 500, and 700 mg/cm$^2$ $^{9}$Be. The $\gamma$-ray yield is normalised to the yield of the MINIBALL detectors for a 130 *A* MeV beam energy and 300 mg/cm$^2$ secondary target thickness.

Fig. 4.13 for the 130 *A* MeV case striking on the three different target thicknesses. For the 300 mg/cm$^2$ Be secondary target the beta distribution is dominated by the secondary beam width of 6 *A* MeV, which can be corrected with the TOF information, and the momentum distribution introduced by the nucleon removal reaction. As a consequence, the resulting

$\beta$-distribution is of a Gaussian shape. For thicker secondary targets the $\beta$-distribution is governed by the energy loss function of the secondary beam within the secondary target material which increases the width of the $\beta$-distribution.

The simulated Doppler corrected Cluster and MINIBALL spectra for a $\gamma$-ray decay in $^{36}$Ca with an energy of $E_{\gamma 0} = 3$ MeV are visualised in Fig. 4.14 and tabulated in Tab. 4.3. Using thin secondary targets results in better energy resolutions than thick secondary targets. But on the other hand, with increasing secondary target thickness the yield of the $\gamma$-ray decays in $^{36}$Ca increases linearly. This overcompensates the slight loss in energy resolution for high beam energies.

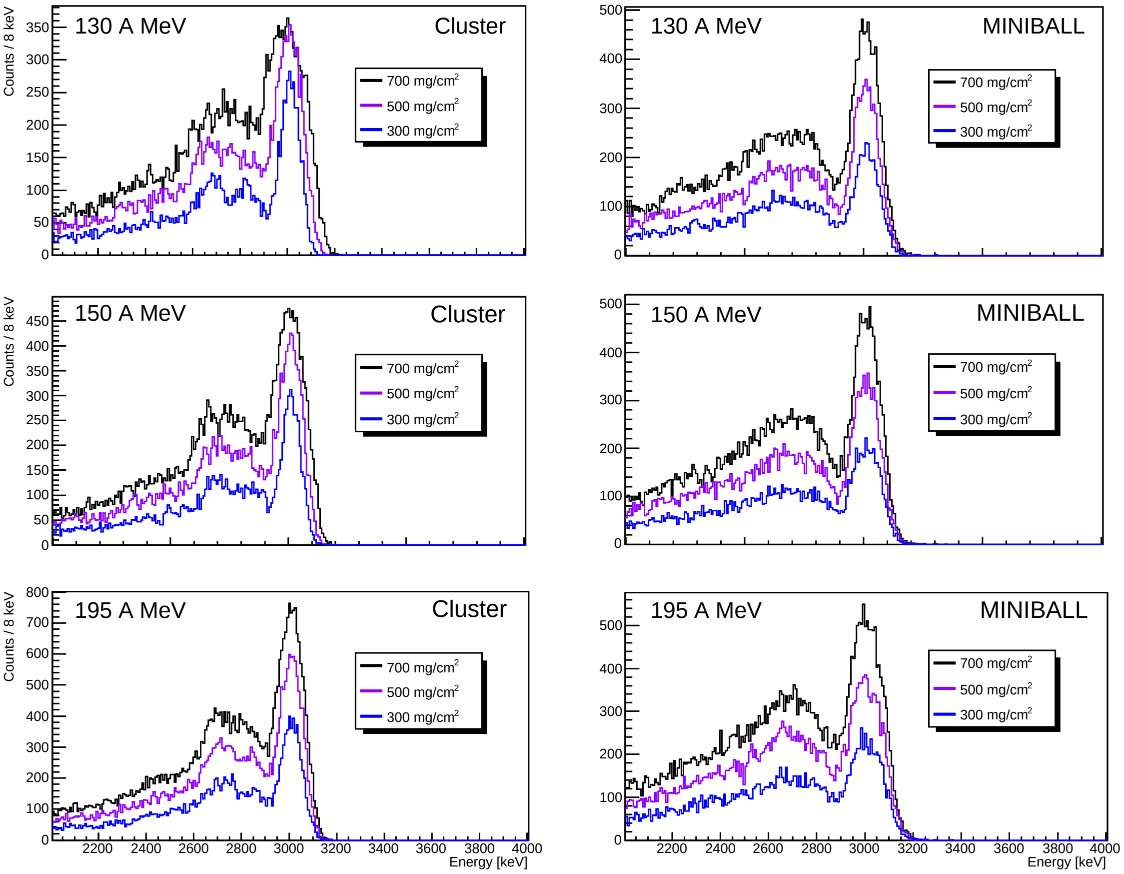

**Figure 4.14:** Simulated Doppler corrected Cluster and MINIBALL spectra for a $\gamma$-ray decay in $^{36}$Ca with an energy of $E_{\gamma 0} = 3$ MeV. The simulations are performed for $^{37}$Ca secondary beam energies of 130, 150, and 195.7 $A$ MeV and secondary target thicknesses of 300, 500, and 700 mg/cm$^2$ $^9$Be.

It is also noteworthy that for a given secondary target thickness the energy resolution is generally augmented for the Cluster detectors with increasing beam energy. As the Cluster detectors are positioned at forward angles, they are very sensitive to the velocity distribution, which broadens for a fixed secondary target thickness while the beam energy is reduced. This effect is more significant than the Doppler broadening described in Eq. 4.11. Furthermore, as the MINIBALL detectors are positioned almost perpendicular to the beam axis in the Lorentz boosted coordinate system, their energy resolution is scarcely affected by a change in secondary target thickness for a given beam energy. In summary, a secondary beam energy of 195.7 $A$ MeV striking on a 700 mg/cm$^2$ $^2$Be secondary target is concluded to be the best choice due to its largest $\gamma$-ray yield.

## 4.4 MINIBALL Crystal Segmentation and Cluster Add-Back Procedure: Implications for High $\gamma$-Ray Energies

The response function of an ideal $\gamma$-ray spectrometer should consist only of the photopeaks which can be associated to decays of the nuclei of interest. However, as seen for the simulated Doppler corrected $\gamma$-ray spectra in Fig. 4.6, the photopeaks are accompanied by a continuum of Compton scattered events. For higher $\gamma$-ray energies also components of single- and double-escape events emerge. Most of the Compton continuum consist of single Compton scatterings which are followed by the escape of the scattered $\gamma$-ray. On the other hand, the photopeak events are comprised of multiple scatterings and a photoelectric absorption at the end. Therefore, the peak-to-background ratio $P/T$ can be enhanced if more than one interaction is required within the detector. This can be accomplished if the Cluster detectors are used in the add-back mode, i.e. at least a $\gamma$-ray multiplicity of two is required for the seven crystals of one single Cluster detector. For the MINIBALL array the segmentation of the individual crystals can be used to select $\gamma$-rays that scattered within one or more crystals of the same detector.

The single- and double-escape peak reduction can be investigated for the MINIBALL array with the $3^-_1 \rightarrow 0^+_{g.s.}$ decay at a $\gamma$-ray energy of 6130 keV from the $^{16}$O calibration source. In Fig. 4.15 segment multiplicity one and two events are compared. Single- and double-escape events are suppressed relative to the photopeak intensity when a segment

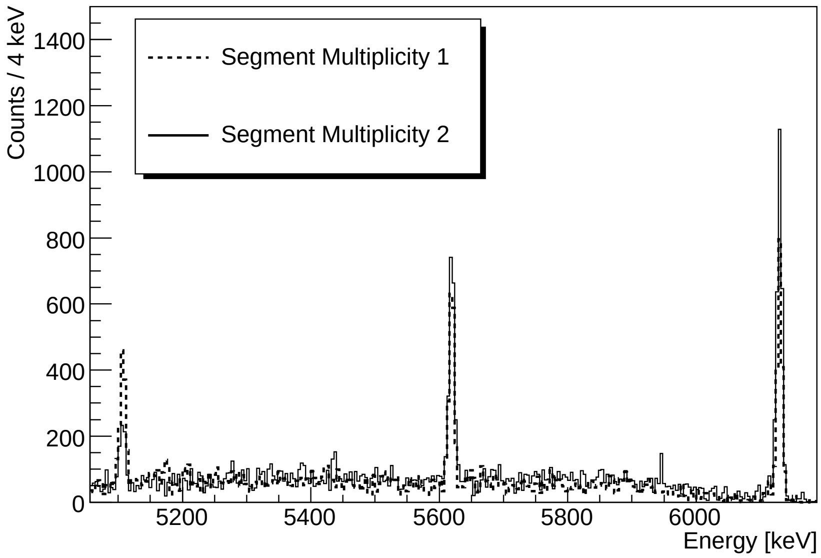

**Figure 4.15:** MINIBALL energy spectra of a 6130 keV calibration source ($^{16}$O) for a segment multiplicity equal to one (dashed line) and two (solid line). If a segment multiplicity of two is required, single- and double- escape events are suppressed relative to the photopeak.

multiplicity of two is required. However, the photopeak events of a segment multiplicity equal to one events are lost if such a condition is demanded. A similar result is obtained for the Cluster detectors.

In the next step the influence on the energy resolution for $\gamma$-rays emitted in-flight can be investigated by means of simulations. The Doppler shift correction applied to the scattered $\gamma$-ray is performed with the position information from the crystals centre for the Cluster detectors and with the segments centre for the MINIBALL detectors that measures the highest energy. But not in all cases this is the crystal or segment in which the first interaction takes place. Therefore, a reduced energy resolution is expected.

To study the change in energy resolution and also the loss in efficiency $\varepsilon_{peak}$ for a $\gamma$-ray of $E_{\gamma 0} = 3$ MeV, the Cluster and MINIBALL simulations are analysed under the condition of single hit and add-back events for the Cluster array and segment multiplicity one and two for the MINIBALL array, respectively. The Doppler corrected spectra of the MINIBALL array are shown in Fig. 4.16. In the spectrum of a segment multiplicity equal to one scattered $\gamma$-rays that do not release their full energy have the same height as the photopeak. The advantage of considering only events of a segment multiplicity equal to two is evident

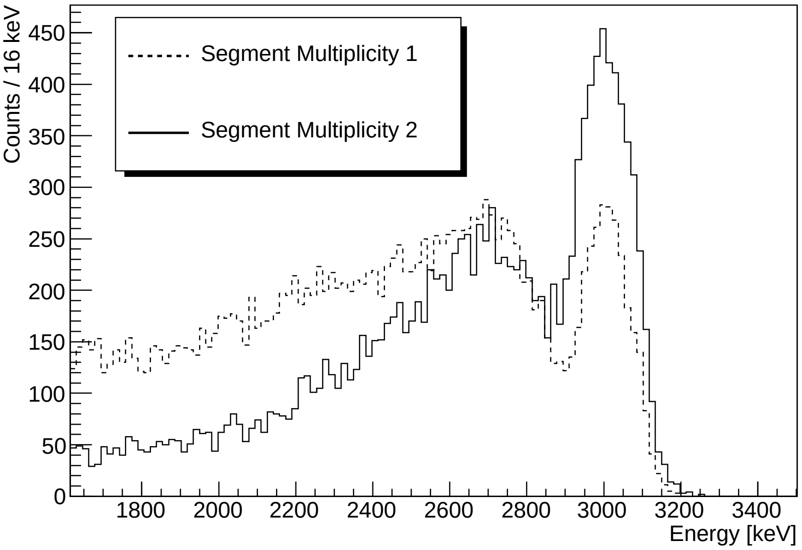

**Figure 4.16:** Simulated Doppler corrected MINIBALL $\gamma$-ray spectra requiring segment multiplicity one and two for a $E_{\gamma 0} = 3$ MeV $\gamma$-ray decay from $^{36}$Ca. The incoming $^{37}$Ca secondary beam energy is 195.7 $A$ MeV and the secondary target has a thickness of 700 mg/cm$^2$ $^9$Be.

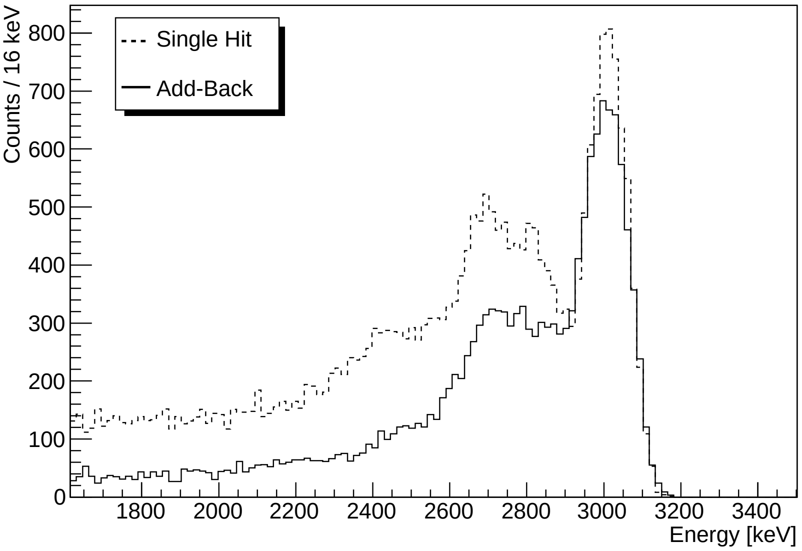

**Figure 4.17:** Doppler corrected Cluster $\gamma$-ray spectra used in the single hit and add-back mode for an $E_{\gamma 0} = 3$ MeV $\gamma$-ray decay from $^{36}$Ca. The incoming $^{37}$Ca secondary beam energy is 195.7 $A$ MeV and the secondary target had a thickness of 700 mg/cm$^2$ $^9$Be.

as most Compton scattered, single-, and double-escape events are discriminated. (This counts also for $\gamma$-rays not originating from the target.) Thereby, the $P/T$ ratio raises from 0.05 to 0.2. However, about 1/3 of the peak integral is lost and the energy resolution is slightly worse, being 4.6 % compared to 4.1 % for events of a segment multiplicity equal to one.

The Doppler corrected spectra of the Cluster array are shown in Fig. 4.17. About half of the peak integral is lost if the add-back case is separated from single hit events. The energy resolution worsens from 3.5 % for single hit events to 3.8 % for add-back events. The $P/T$ ratio increases from 0.1 for single hit events to 0.2 for the add-back case.

In summary, selecting segment multiplicity two events for the MINIBALL array and add-back events for the Cluster array increases the $P/T$ ratio considerably, while the energy resolution remains almost unchanged. Compton scattered, single-, and double-escape events are reduced compared to the photopeak intensity. For experimental $\gamma$-ray peaks sitting on top of a high background the background can thereby be reduced significantly.

# 5 Data Acquisition, Analysis, and Experimental Results

In the following chapter the analysis and the results on the two-step fragmentation experiment with a $^{37}$Ca secondary beam are presented. The main goal is the identification of unknown transitions in $^{36}$Ca, especially the $2_1^+ \rightarrow 0_{g.s.}^+$. Since no $\gamma$-ray transition is known for $^{36}$Ca, Doppler correction, mass selection with CATE, and the performance of the Cluster, MINIBALL, and HECTOR array for high energy $\gamma$-rays have to be optimised for other reaction channels. Tab. 5.1 shows the results of EPAX cross-section calculations [54] of the $^{37}$Ca + $^{9}$Be reaction. The strongest reaction channels are expected to provide the highest $\gamma$-ray yield and are therefore dedicated for analysis optimisations.

| $Z\backslash N$ | 12 | 13 | 14 | 15 | 16 | 17 |
|---|---|---|---|---|---|---|
| 20 (Ca) | | | | 0.01 | 1.8 | Beam |
| 19 (K) | | | | | 4.2 | 66.1 |
| 18 (Ar) | | | 0.5 | 0.5 | 8.6 | 46.7 |
| 17 (Cl) | | | 1.4 | 2.6 | 17.1 | 29.6 |
| 16 (S) | | | 1.2 | 9.3 | 25.3 | 16.3 |
| 15 (P) | | 0.7 | 5.9 | 2.0 | 20.5 | 6.6 |
| 14 (Si) | 0.6 | 4.5 | 16.0 | 20.8 | 8.8 | 1.8 |

**Table 5.1:** EPAX calculated cross-sections (mbarn) for the population of different nuclei after fragmentation reactions induced by a $^{37}$Ca projectile impinging on a $^{9}$Be target.

So far, the particle identification and the $\gamma$-ray detection systems were covered independently from each other. However, to associate observed $\gamma$-rays with reaction channels, the signals from the individual detectors have to be linked. This is the task of the data acquisition (DAQ) and control system which needs to be discussed.

## 5.1 Data Acquisition and Control System

Each of the four detectors systems, the FRS including CATE, the Cluster detectors, the MINIBALL detectors, and the HECTOR array has its own data acquisition system producing independent events. The multi branch system MBS [84, 85] was developed in the framework of the GSI standard DAQ system to assemble them into one common event by applying a time-stamping technique for event synchronisation. Therefore, the four sub-systems in the RISING DAQ are equipped with the VME time stamping module TITRIS [86]. It produces a single-hit 48 bit time stamp with a granularity of 20 ns. One of the TITRIS modules is arbitrary chosen to be the master, while the others are the slaves. They are connected in line via a synchronisation bus. The master module sends regularly synchronisation pulses to all slave modules to keep all modules on the same time base.

Due to this approach the RISING sub-systems can run independently and are fully operational DAQ systems with individual trigger sources. In addition, identical triggers can be fed into all sub-systems and their local dead times can be combined. Upon the reception of each accepted trigger the digitisers are read out and the event data is sent via a Transmission Control Protocol (TCP) socket to an event builder. The time-stamping module gets a signal from the Master Trigger Output signal for each accepted trigger. The time difference of the time stamps from the trigger amounts up to 3 $\mu$s which is caused by various signal delay times of the VXI trigger card [87] and the Master Trigger Output of the VME trigger module. This constant time offset is taken into account for the time matching of events from different sub-systems. A schematic diagram of the RISING DAQ system is presented in Fig. 5.1.

The VXI Cluster cards are read out by the the VXI Readout engine (VRE) and the data is sent via the DT32 bus to a VME processor [76]. On the VME processor the event data is sent in large data blocks via TCP sockets to an MBS event-builder PC. This event-builder receives the data, converts it into the MBS data format, and provides it for further processing. For the FRS/CATE, HECTOR, and MINIBALL the DAQ systems are structurally identical. A VME crate contains a RIO3 readout processor, the GSI trigger module [88], the TITRIS time stamping module, QDC, ADC, TDC, scaler, and pattern units. For the MINIBALL array the CAMAC crate containing the DGF modules is read out via a VC32-CC32 CAMAC controller which consists of a VME interface module (VC32) and a CAMAC controller (CC32) that are connected via a SCSI like cable.

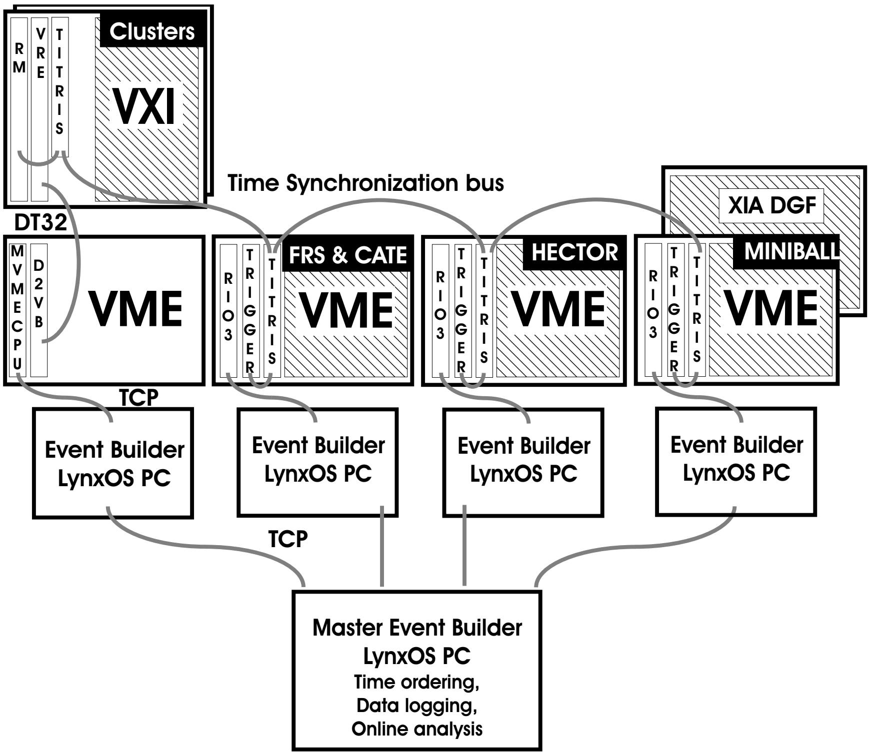

**Figure 5.1:** Block diagram of the RISING data acquisition system. See text for details.

The collecting and sorting of the data from all sub-systems is made by the RISING master event-builder running with an additional, independent MBS system. It is used to connect and disconnect to the four sub-systems data output streams via TCP sockets. The events coming from the connected systems are then sorted according to their time stamps in ascending order into a single data output stream and formated into output buffers for data logging and online monitoring purposes.

In the data analysis the events are selected from the time sorted event stream and combined to real “physics” events. For the on-line analysis of the RISING data the ROOT based GO4 package [89] is used in conjunction with the graphical user interface CRACOW [90]. The programme takes a portion of the data output stream from the MBS master event builder and allows for merging time sorted sub-events into complete “physical” events. In the off-line analysis GO4 is used to write the collected data into ROOT-files which are later divided into smaller files and analysed with ROOT.

### 5.1.1 Trigger Options

The basic trigger signal is extracted from the timing signal of the scintillator positioned at the final focal plane (SCI2) in combination with signals from other branches:

- SCI2 in coincidence with at least one $\gamma$-ray in the Cluster detectors. This triggers both, the Cluster and FRS/CATE DAQ system.
- SCI2 in coincidence with at least one $\gamma$-ray in the MINIBALL detectors. This trigger initiates the MINIBALL and FRS/CATE readout.
- SCI2 in coincidence with at least a single $\gamma$-ray in the HECTOR array starts the FRS/CATE and HECTOR DAQ system.
- During the $\gamma$-ray measurement with fragments the SCI2 trigger is used in a scaled down mode (scaled down factor $= 2^8$) to allow for a normalisation on the number of incoming particles.

It is also possible to trigger with the individual $\gamma$-ray detectors as well as FRS detectors (SCI1, SCI2 and the MWPCs) in the singles mode for calibration purposes.

## 5.2 Background Investigations

The charge of the fragments after the secondary target is identified via their energy loss measurement in the CATE Si detectors. The fragments are then slowed down and stopped in the thick CATE CsI(Tl) detectors to measure their total residual energy $E_{res}$. By stopping in the CsI(Tl) detectors reactions occur after the heavy ions have passed the CATE Si detectors. The nuclear reactions in the CsI(Tl) detectors lead to fairly different nuclei in excited states. The emitted $\gamma$-rays of these states are detected by the HECTOR array, which has a very good time resolution. In Fig. 5.2 the $BaF_2$ time spectra are displayed after the selection of calcium and sulphur fragmentation products with CATE from the $^{37}$Ca secondary beam. For the calcium isotopes two distinct time peaks are seen. They originate from $\gamma$-rays after reactions in the secondary target and in the CATE detectors. This is corroborated by the fact that the difference of the two time peaks is 14 ns. This

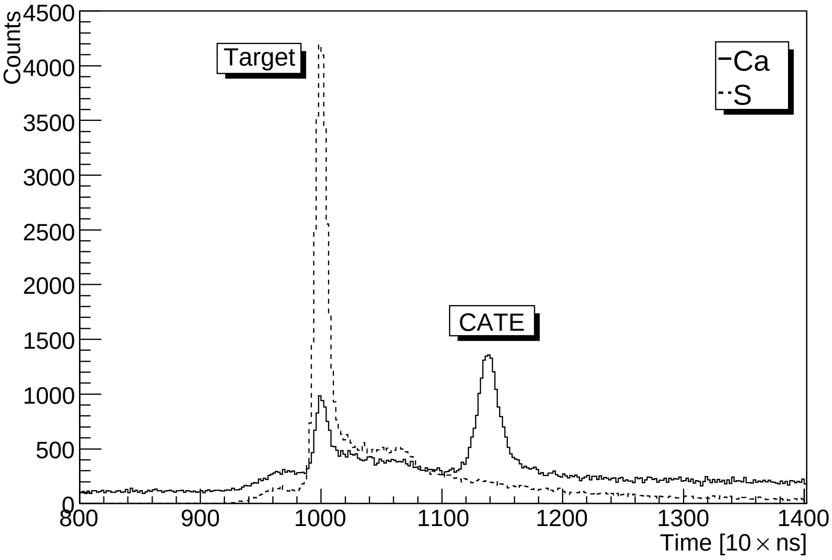

**Figure 5.2:** HECTOR array time spectra after selecting the calcium (solid line) and sulphur (dashed line) reaction channels with CATE.

time difference is explained by the time needed for a heavy ion to reach CATE from the target (9 ns) plus a $\gamma$-ray emitted from the CATE detector (5 to 6 ns).

The situation changes when a gate on sulphur isotopes is applied. Here, a reaction must have taken place already in the secondary target or in the target Si detector in order to identify sulphur with CATE. This is shown in Fig. 5.2 by the dashed curve where almost all particle-$\gamma$ coincidences originate from the secondary target.

### 5.2.1 Conditions on the $\gamma$-Ray Times

It was just shown that most of the events related to identified calcium ions are caused from reactions within the CATE detector. These can be identified and discriminated with the HECTOR array due to the good time resolution of the $BaF_2$ detectors. But in the case of Ge detectors the separation is hindered by (i) the time resolution of 12 ns and (ii) the detectors positioned geometrically closer to the CATE detectors than the HECTOR array. Therefore, a very narrow time condition has to be applied to the Cluster and MINIBALL detectors to obtain calcium reactions from the secondary target. The relevant time spectra for imposed gates on calcium and sulphur reaction products from the $^{37}$Ca secondary beam are displayed in Fig. 5.3 for the Cluster detectors and in Fig. 5.4 for the MINIBALL detectors.

For the Cluster detectors the time peak of the $\gamma$-rays shifts from channel 5000 to channel 4960 if calcium fragments are selected instead of sulphur fragments. These spectra have the particularity that the electronics used for the measurement cause a direction for the timeline from right to left. The peak position, when gated on calcium, is located more to the left and is dominated by the $\gamma$-rays from CATE as already seen by the HECTOR array. To get $\gamma$-rays emitted from the target, the prompt $\gamma$-ray time window for calcium reaction products is set from channel 4980 to 5060 around the maximum of the time peak observed for the sulphur reaction channel. For reaction channels other than calcium a wider gate from channel 4940 to 5100 is used since the $\gamma$-background due to CATE is reduced.

The MINIBALL detectors are "shielded" by the Cluster detectors, which are placed in a direct line in between the MINIBALL array and CATE. Hence, they suffer less from background produced in CATE for selected calcium, as is depicted in Fig. 5.4. A distinction between $\gamma$-rays originating from the secondary target at channel 1000 and CATE at channel 1045 is possible. To minimise the background from CATE in the calcium reaction channel, the prompt $\gamma$-ray time window for the MINIBALL detectors is set from channel

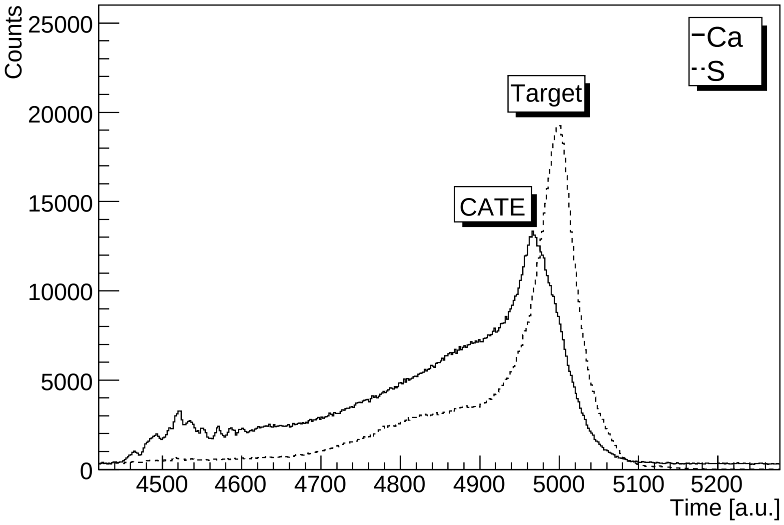

**Figure 5.3:** Cluster array time spectra after selecting the calcium (solid line) and sulphur (dashed line) reaction channels with CATE. The time increases to the left.

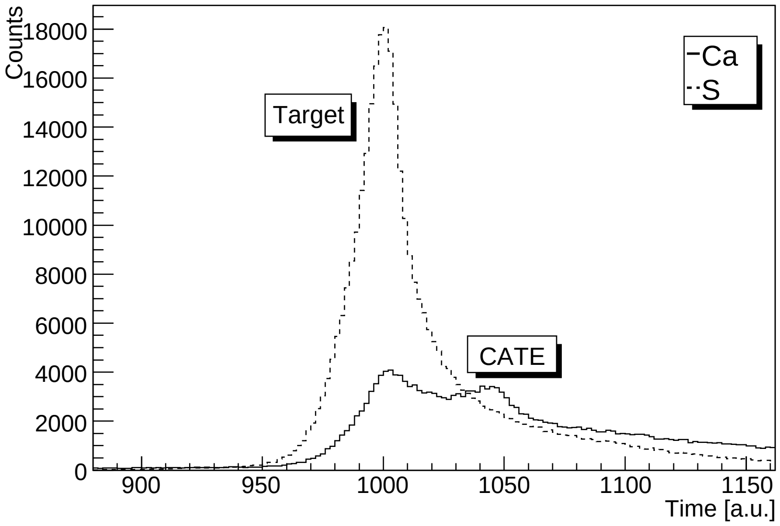

**Figure 5.4:** MINIBALL array time spectra after selecting calcium (solid line) and sulphur (dashed line) reaction channels with CATE.

985 to channel 1015 close to the time peak observed in the sulphur reaction channel. For other reaction channels a time gate from channel 960 to channel 1040 is applied.

## 5.3 Observed $\gamma$-ray Transitions

The observed $\gamma$-ray decays of reaction fragments shown in this section are especially selected for high transition energies in order to be comparable with the $^{36}$Ca case. For the Doppler correction of the $\gamma$-ray spectra the mean velocity value $\beta$ ($\approx 0.54$) is obtained with Monte Carlo Methods that are described in Ch. 4 and Ch. 7. Deviations of this value in front of the secondary target are corrected on an event-by-event basis using the TOF information between the scintillators SCI1 and SCI2, as it is described in Ref. [91]. The fragments are tracked with the Si detector at the target position and with the CATE Si detectors. The transition energies are fitted with a Gaussian distribution on top of a linear background.

For $^{28,29}$Si the Doppler corrected $\gamma$-ray spectra for photopeak and Compton scattering events will be discussed for the three $\gamma$-ray arrays and the resulting transition energies are compared to corresponding literature values of known transitions. A similar analysis is performed for $^{31,32,33}$S. In addition, the MINIBALL data are compared with and without pulse shape analysis. For the $^{34,35}$Ar reaction channels only a few nucleons are removed from the secondary $^{37}$Ca beam, which allows for the investigation of the necessary mass separation with the CATE array. Excitations found in the chlorine and potassium reaction channels involve large lifetime effects. Implications for the lineshape and energy measurement of these nuclei are covered in Ch. 7.

### 5.3.1 Decays of High Energetic $\gamma$-Ray Transitions in $^{28,29}$Si

The Doppler corrected $\gamma$-ray spectrum for the Cluster array shown in Fig. 5.5 is produced with gates on silicon fragments. Distinct peaks of the $3/2^+_1 \rightarrow 1/2^+_{g.s.}$ and $5/2^+_1 \rightarrow 1/2^+_{g.s.}$ transitions at 1270(3) and 2023(6) keV from $^{29}$Si are visible. The most prominent peak is the $2^+_1 \rightarrow 0^+_{g.s.}$ transition at 1780(2) keV from $^{28}$Si. At 2820 keV indications of the known $4^+_1 \rightarrow 2^+_1$ decay are visible. When the photopeak (single hit) events are compared to the Compton scattering (add-back) events it is found that the add-back spectrum, though weak in statistics, shows an elevation at 2815(28) keV.

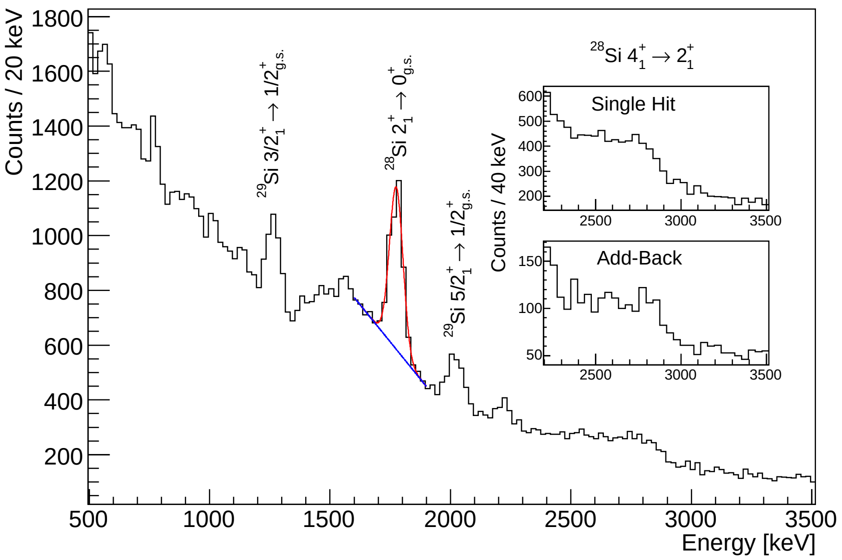

**Figure 5.5:** Doppler corrected $\gamma$-ray spectrum for the $^{28,29}$Si reaction channels measured with the Cluster array. For the $2^+_1 \rightarrow 0^+_{g.s.}$ transition in $^{28}$Si an exemplary Gaussian fit on a linear background is shown. The inserts show the energy region around the $4^+_1 \rightarrow 2^+_1$ transition in $^{28}$Si which were analysed for photopeak (single hit) and Compton scattering (add-back) events.

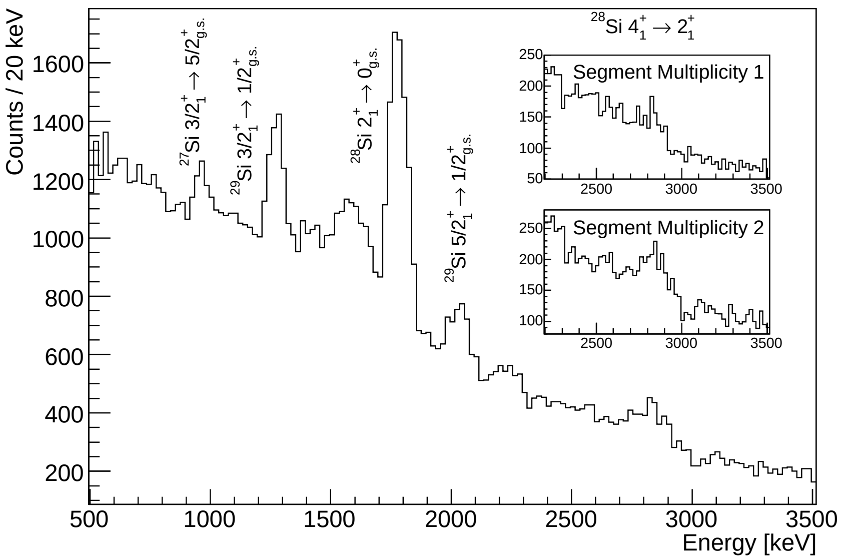

**Figure 5.6:** Doppler corrected $\gamma$-ray spectrum for the $^{28,29}$Si reaction channels measured with the MINIBALL array. The $4^+_1 \rightarrow 2^+_1$ transition of $^{28}$Si is only visible for the segment multiplicity of two, as shown in the insert.

The single hit case, however, is dominated by Compton scattered and single-escape $\gamma$-rays and therefore shows a shoulder below the known transition energy. As a consequence for the $^{36}$Ca analysis, the high-energetic $2^+_1 \rightarrow 0^+_{g.s.}$ decay may only be seen in the add-back mode.

The situation is similar for the MINIBALL detectors. In Fig. 5.6 events with a segment multiplicity of one and two are compared instead. The $4^+_1 \rightarrow 2^+_1$ transition of $^{28}$Si is pronounced for events of a multiplicity of two while in the other case no clear evidence for a peak can be detected.

The HECTOR array is designed to measure high $\gamma$-ray transition energies. Therefore, Fig. 5.7 displays a distinct peak of the $4^+_1 \rightarrow 2^+_1$ transition in $^{28}$Si at 2850(20) keV for the background subtracted spectrum. However, the HECTOR energy resolution is only about 14 % so that other observed transition lines cannot be resolved.

Tab. 5.2 summarises the observed transitions for imposed gates on silicon in comparison to the literature values [15]. All measured values are in good agreement with the literature values. The analysis of known transition energies is employed to prove the accurate Doppler correction for the FRS-RISING setup which depends on the fragment velocity and detector positions.

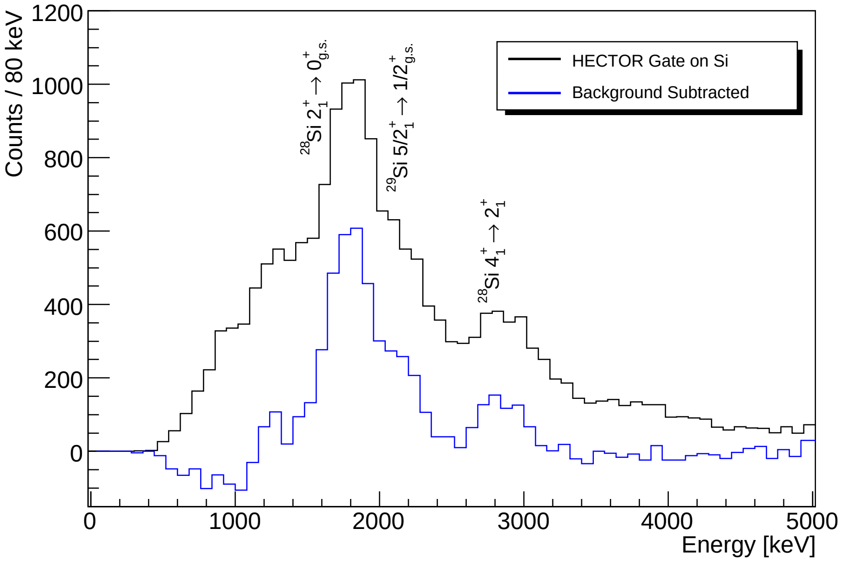

**Figure 5.7:** Doppler corrected $\gamma$-ray spectrum for the $^{28,29}$Si reaction channels measured with the HECTOR array. The black and blue coloured spectra are without and with background subtraction, respectively.

| Literature Energy | Nuclide | Transition | Detector |  |  |
|---|---|---|---|---|---|
|  |  |  | Cluster | MINIBALL | HECTOR |
| 957.4(2) | $^{27}$Si | $3/2_1^+ \to 5/2^+_{g.s.}$ |  | 962(5) |  |
| 1273.367(12) | $^{29}$Si | $3/2_1^+ \to 1/2^+_{g.s}$ | 1270(3) | 1273(2) |  |
| 1778.969(12) | $^{28}$Si | $2_1^+ \to 0^+_{g.s.}$ | 1780(2) | 1781(1) |  |
| 2028.12(6) | $^{29}$Si | $5/2_1^+ \to 1/2^+_{g.s}$ | 2023(4) | 2034(4) |  |
| 2838.67(5) | $^{28}$Si | $4_1^+ \to 2_1^+$ | 2815(28) | 2836(16) | 2850(20) |

**Table 5.2:** Measured transition energies from the silicon isotopes $^{27,28,29}$Si are compared to literature values from Ref. [15]. The value of the $4_1^+ \to 2_1^+$ transition in $^{28}$Si is given for add-back events in the Cluster array, for segment multiplicity two events in the MINIBALL array, and for the background subtracted case of the HECTOR array. The energy assignment errors include only the statistical error from a Gaussian fit on linear background.

### 5.3.2 Decays of High Energetic $\gamma$-Ray Transitions in $^{31,32,33}$S

For the strong reaction channels $^{31,32,33}$S the $\gamma$-rays are also analysed. The Cluster spectrum, shown in Fig. 5.8, has a strong $\gamma$-ray de-excitation doublet at 2231(2) keV. This line originates from the $2^+_1 \rightarrow 0^+_{g.s.}$ transition in $^{32}$S with an energy of 2230.3 keV and the $5/2^+_1 \rightarrow 1/2^+_{g.s.}$ transition of $^{31}$S with an energy of 2235.6 keV [15]. Due to the larger fragmentation cross-section of $^{32}$S (see Tab. 5.1) the $2^+_1 \rightarrow 0^+_{g.s.}$ transition in $^{32}$S is expected to provide the bigger portion for the doublet. In addition, for $^{31}$S the $3/2^+_1 \rightarrow 1/2^+_{g.s.}$ transition is visible at 1248(2) keV.

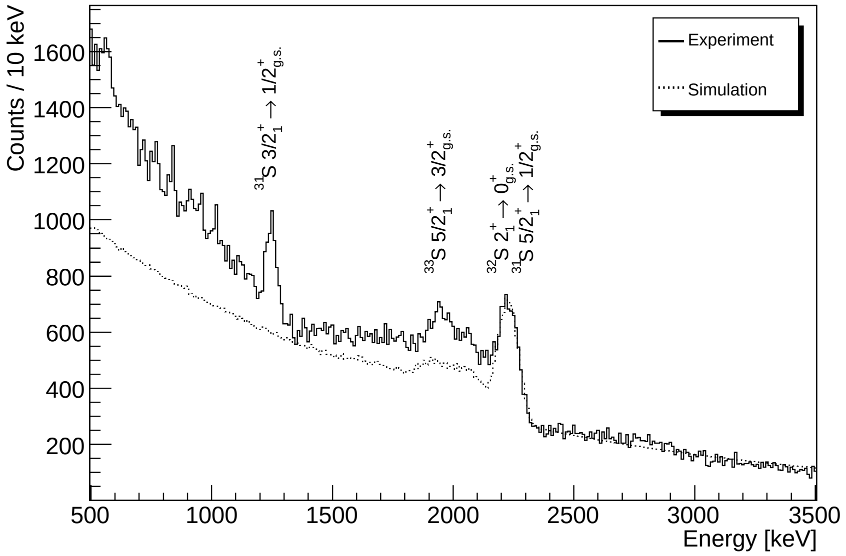

**Figure 5.8:** Doppler corrected $\gamma$-ray spectrum for the $^{31,32,33}$S reaction channels measured with the Cluster array (solid line). A comparison with the simulation of the $2^+_1 \rightarrow 0^+_{g.s.}$ decay in $^{32}$S is shown (dotted line). The simulation includes background from an exponential fit of the experimentally observed background between 2500 and 5000 keV. It does not include $\gamma$-ray transitions from $^{31}$S and $^{33}$S.

GEANT4 simulations are performed for the $2^+_1 \rightarrow 0^+_{g.s.}$ transition of $^{32}$S, see Fig. 5.8, which yield an energy resolution of 87 keV (3.9 %). The experimental energy resolution of 84(4) keV (3.8(2) %) for the doublet is in excellent agreement with this value. The simulation include an exponentially declining background that is deduced from a fit of the experimentally observed background between 2500 and 5000 keV. The experimental shape of the photopeak matches the simulation. The $\gamma$-ray spectrum below the photopeak is not

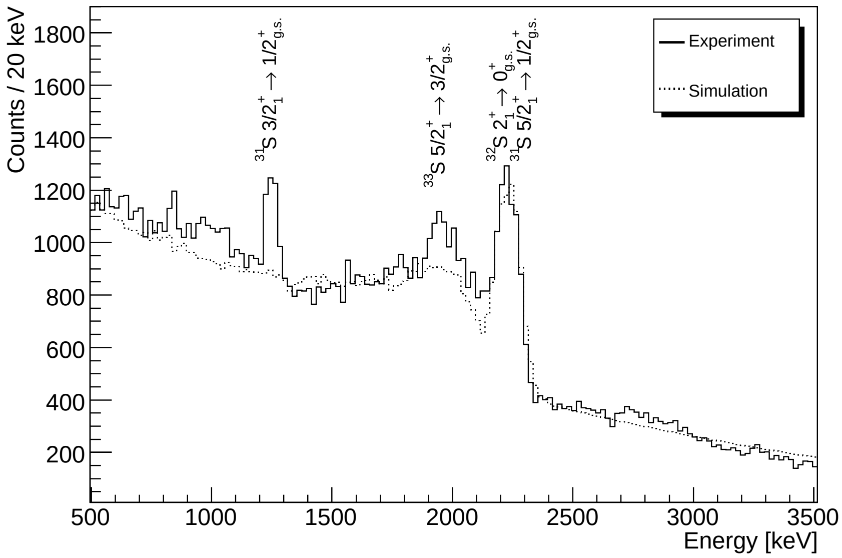

**Figure 5.9:** Doppler corrected $\gamma$-ray spectrum for the $^{31,32,33}$S reaction channels measured with the MINIBALL array (solid line). A comparison with the simulation of the $2^+_1 \rightarrow 0^+_{g.s.}$ decay in $^{32}$S is shown (dotted line). The simulation includes background from a quadratic fit of the experimentally observed background between 2500 and 5000 keV. It does not include $\gamma$-ray transitions from $^{31}$S and $^{33}$S.

well reproduced in the simulation due to lower-lying lines, such as the $5/2^+_1 \rightarrow 3/2^+_{g.s.}$ transition in $^{33}$S at an energy of 1967.2 keV [15] which are not included in the simulation.

The same lines are also seen with the MINIBALL array, displayed in Fig. 5.9, where the observed peak at 2333(3) keV is compared to a GEANT4 simulation of the $2^+_1 \rightarrow 0^+_{g.s.}$ decay in $^{32}$S. The simulation yield an energy resolution of 105 keV (4.7 %), while from the experiment a value of 104(4) keV (4.7(2) %) is obtained. The simulation include a quadratic background that is deduced from a fit of the experimentally observed background between 2500 and 5000 keV.

The high yield of $\gamma$-rays for the two transitions observed at 2230 keV allows for a comparison between the energy resolutions obtained after applying a Doppler correction using the position information of the detected $\gamma$-ray obtained from (i) the MINIBALL segment centres and (ii) from the pulse shape analysis (PSA) algorithms. The PSA algorithms are only employed for segment multiplicity one events. In Fig. 5.10 the corresponding spectra are shown for both cases. Using the segment centres an energy resolution of 95(7) keV (4.2(3) %) is obtained. The PSA algorithms yield an energy resolution of 73(5) keV

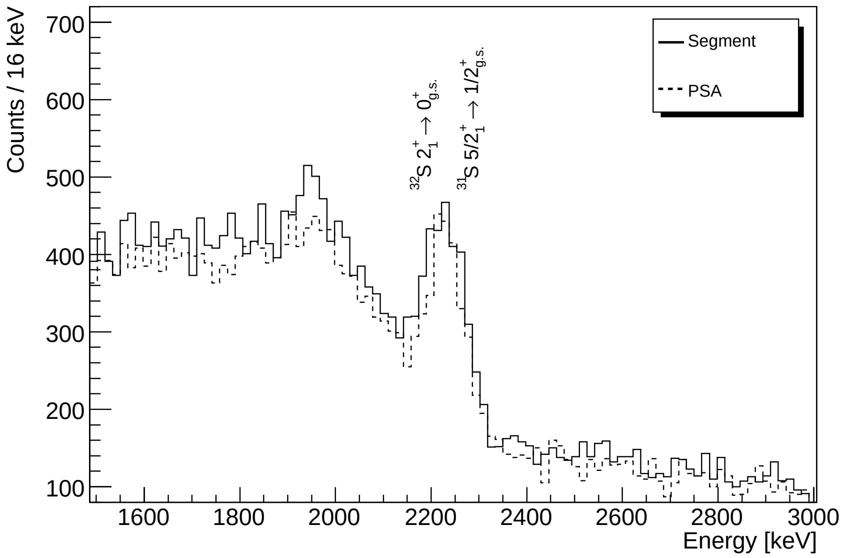

**Figure 5.10:** Doppler corrected MINIBALL $\gamma$-ray spectra for the $^{31,32,33}$S reaction channels using the position information obtained from the segment centres (solid line) or PSA algorithms (dashed line). Only events with a segment multiplicity equal to one are compared.

(3.3(3) %). However, $\approx$ 30 % of the events are lost in the latter case, as the peak integral reduces from 1488(133) counts to 1053(98) counts. The reduced intensity is due to events where either the $r$ or the $\varphi$ coordinate of the segment cannot be determined. In conclusion, the PSA procedure yields an improvement of the energy resolution. However, it results in a big loss of peak intensity for the already weak case of segment multiplicity one photopeak events for high $\gamma$-ray energies. Therefore, it is not used in the $^{36}$Ca analysis.

The sulphur gated spectra of the HECTOR array is displayed in Fig. 5.11. The measured transition energy for the doublet at 2230 keV is shifted to 2190(20) keV. This might be due to the unresolved $5/2^+_1 \rightarrow 3/2^+_{g.s.}$ transition of $^{33}$S. The transition energies for sulphur fragments are summarised in Tab. 5.3 for the three detector systems, showing a good agreement with literature values.

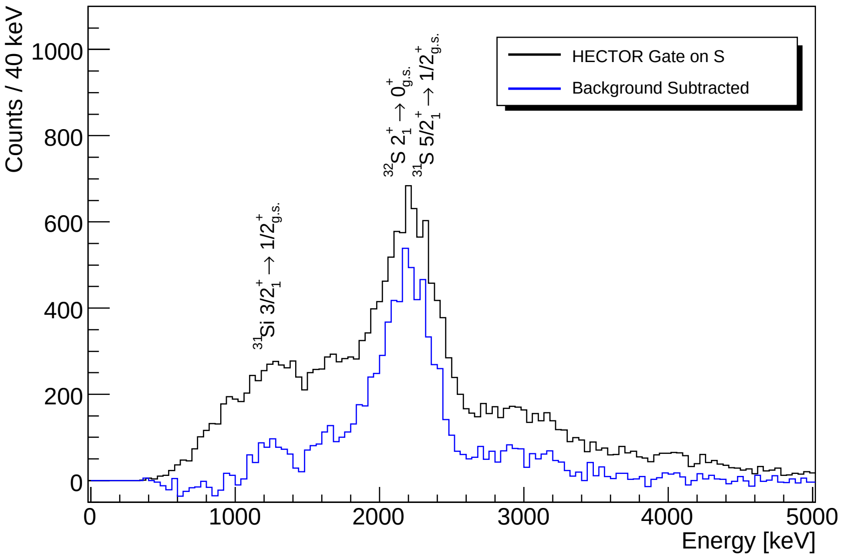

**Figure 5.11:** Doppler corrected $\gamma$-ray spectrum for the $^{31,32,33}$S reaction channels measured with the HECTOR array. The black and blue coloured spectra are without and with background subtraction, respectively.

| Literature Energy | Nuclide | Transition | Detector | | |
|---|---|---|---|---|---|
| | | | Cluster | MINIBALL | HECTOR |
| 1248.9(2) | $^{31}$S | $3/2^+_1 \rightarrow 1/2^+_{g.s.}$ | 1248(2) | 1252(3) | 1250(10) |
| 2230.3(2)<br>2235.6(4) | $^{32}$S<br>$^{31}$S | $2^+_1 \rightarrow 0^+_{g.s.}$<br>$5/2^+_1 \rightarrow 1/2^+_{g.s.}$ | 2231(2) | 2233(3) | 2190(20) |

**Table 5.3:** Measured transition energies from the sulphur isotopes $^{31,32}$S are compared to literature values from Ref. [15]. The values for the HECTOR array are given for the background subtracted case. The energy assignment errors include only the statistical error from a Gaussian fit on linear background.

### 5.3.3 Decays of High Energetic $\gamma$-Ray Transitions in $^{34,35}$Ar

In the secondary fragmentation process a parallel momentum distribution is introduced that increases with the number of removed nucleons (see Eq. 3.1). This affects the correlation between the mass of a fragment and the residual energy $E_{res}$ measured with the CATE CsI(Tl) detectors. The measured $^{34,35}$Ar isotopes are in close vicinity of the $^{37}$Ca secondary beam and are produced by the removal of a few nucleons, namely a (2p,1n) and (2p) reaction. Therefore, they are the ideal test for the mass separation with the CATE detector. The mass separation is investigated by a plot of the Doppler corrected $\gamma$-ray energy versus $E_{res}$. Known observed $\gamma$-ray transitions in $^{35}$Ar should correspond to a higher measured residual energy $E_{res}$ than $\gamma$-ray transitions in $^{34}$Ar.

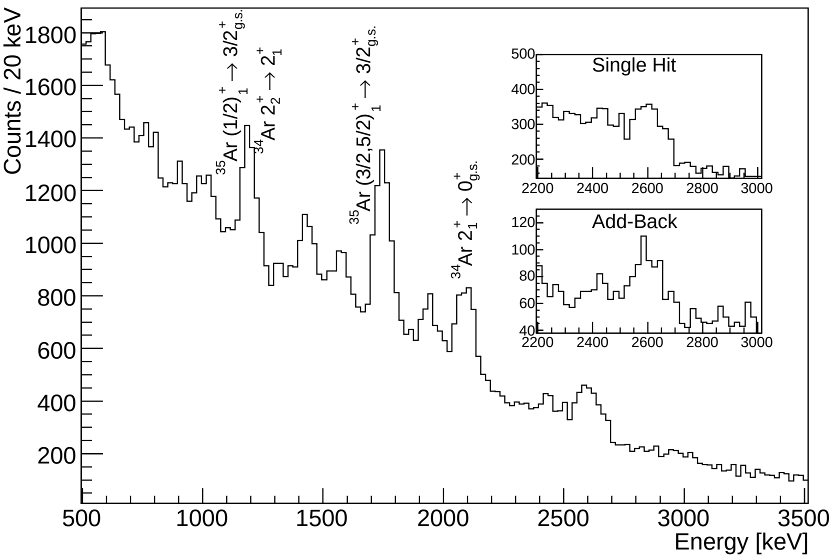

**Figure 5.12:** Doppler corrected $\gamma$-ray spectrum for the $^{34,35}$Ar reaction channels measured with the Cluster array. For the doublet at 2600 keV a peak is more pronounced for the add-back case, while the single-hit spectrum shows only a shoulder.

In the $\gamma$-ray spectrum of the Cluster detectors, shown in Fig. 5.12, several lines are visible: At 1193(2) keV a doublet of the $2_2^+ \rightarrow 2_1^+$ decay in $^{34}$Ar and the $1/2_1^+ \rightarrow 3/2_{g.s.}^+$ decay in $^{35}$Ar; at 1747(2) keV the $(3/2_2^+, 5/2_2^+) \rightarrow 3/2_{g.s.}^+$ transition in $^{35}$Ar; at 2093(4) keV the $2_1^+ \rightarrow 0_{g.s.}^+$ transition in $^{34}$Ar; at 2595(11) keV a doublet from an energy level of 2600.8(15) with an unassigned spin and the $(3/2,5/2)^+ \rightarrow 3/2_{g.s.}^+$ decay in $^{35}$Ar.

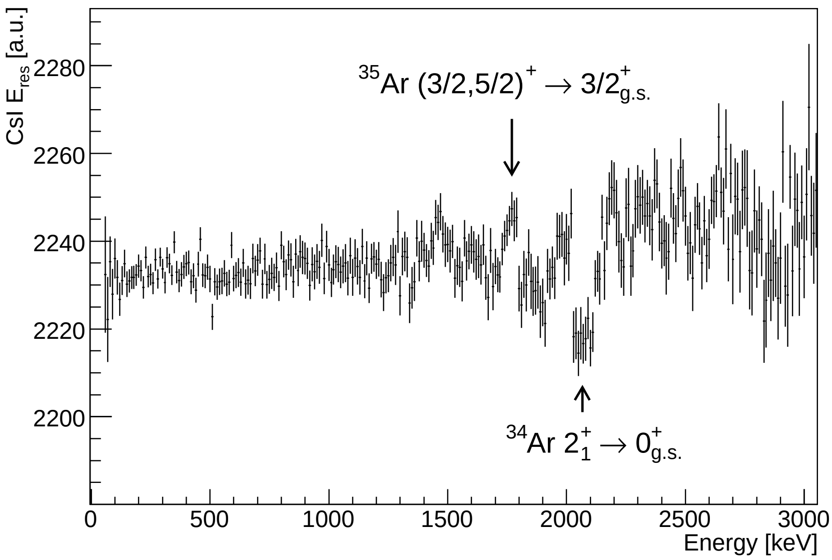

**Figure 5.13:** Dependence of the CATE $E_{res}$ energies on the Doppler corrected $\gamma$-ray energies measured with the Cluster array in $^{35,35}$Ar. For strong $\gamma$-ray transitions different energies from $E_{res}$ can be used to distinguish isotopes.

To investigate the mass sensitivity of the CATE array, the argon $\gamma$-ray spectrum of the Cluster detectors is plotted versus the kinetic energy of the fragments, measured via the CATE $E_{res}$ energy, see Fig. 5.13. For the $(3/2,5/2)^+ \rightarrow 3/2^+_{g.s.}$ transition in $^{35}$Ar at 1750 keV a higher $E_{res}$ energy is observed (channel 2245) than for the $2^+_1 \rightarrow 0^+_{g.s.}$ transition in $^{34}$Ar at 2090 keV (channel 2218). Thus, $\gamma$-ray transitions from a certain nucleus can be enhanced if the corresponding gates are imposed on the CATE $E_{res}$ energy.

An alternative procedure is based on the CATE $\Delta E - E_{res}$ plot for argon isotopes. Based on the fragment energy distributions calculated with the LISE++ code [57], different argon masses can be enhanced better with specific energy cuts on the measured 2-dimensional $\Delta E - E_{res}$ plot, shown in Fig. 5.14. Though the two argon isotopes are not separated, different transitions can be enhanced in Fig. 5.15, namely the $(3/2,5/2)^+ \rightarrow 3/2^+_{g.s.}$ transition for $^{35}$Ar and the $2^+_1 \rightarrow 0^+_{g.s.}$ transition for $^{34}$Ar. The mass separation is expected to be better for the 1n-removal reaction because the parallel momentum spread introduced by the secondary fragmentation reaction calculated from Eq. 3.1 yields $\sigma_{||} = 90$ MeV/c for $^{36}$Ca, while the values for $^{35}$Ar and $^{34}$Ar are 125.5 MeV/c and 151.1 MeV/c $^{34}$Ar, respectively. For completeness the measured transition energies for the argon fragments are summarised in Tab. 5.4, which agree well with the literature values.

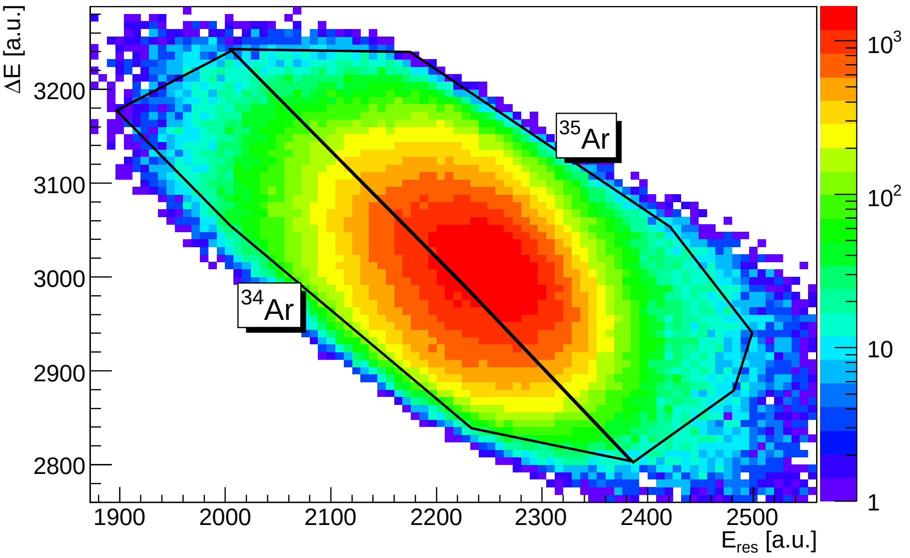

**Figure 5.14:** Argon gated CATE $\Delta E - E_{res}$ plot. The cuts applied for $^{34,35}$Ar are indicated.

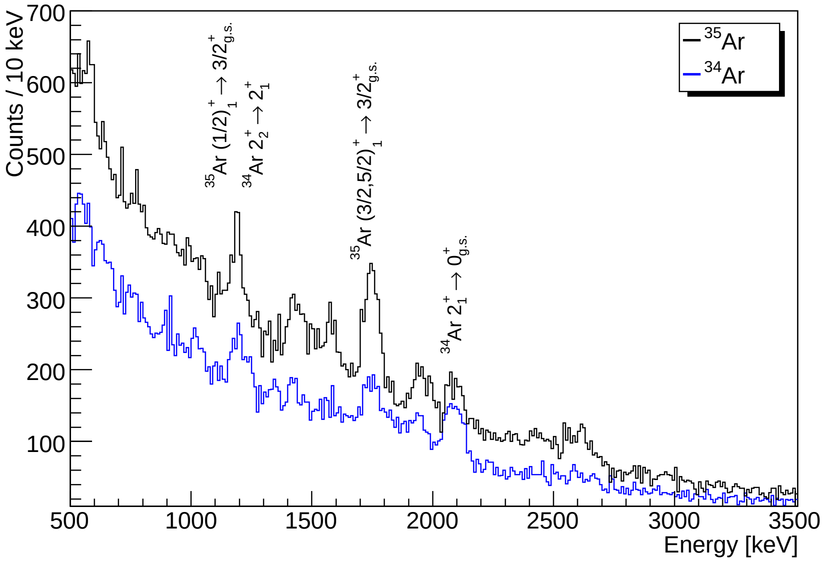

**Figure 5.15:** Doppler corrected Cluster energy spectra for gates imposed on the CATE $\Delta E - E_{res}$ regions of $^{34,35}$Ar.

### 5.3.4 The $2_1^+ \rightarrow 0_{g.s.}^+$ Decay in $^{36}$Ca

The experimental results for the silicon, sulphur, and argon reaction channels demonstrated the accurate Doppler correction procedure for known transition energies. It was shown

| Literature Energy | Nuclide | Transition | Detector | | |
|---|---|---|---|---|---|
| | | | Cluster | MINIBALL | HECTOR |
| 1184.0(3)<br>1196.6(5) | $^{35}$Ar<br>$^{34}$Ar | $1/2_1^+ \rightarrow 3/2_1^+$<br>$2_2^+ \rightarrow 2_1^+$ | 1193(2) | 1193(2) | |
| 1750.6(3) | $^{35}$Ar | $(3/2,5/2)^+ \rightarrow 3/2_{g.s.}^+$ | 1747(2) | 1751(2) | |
| 2090.3(3) | $^{34}$Ar | $2_1^+ \rightarrow 0_{g.s.}^+$ | 2093(4) | 2100(3) | |
| 2600.8(15)<br>2637.9(3) | $^{35}$Ar<br>$^{35}$Ar | $2600.8(15) \rightarrow 3/2_{g.s.}^+$<br>$(3/2,5/2)^+ \rightarrow 3/2_{g.s.}^+$ | 2595(11)[a] | 2612(9)[b] | |

---

[a] Only add-back.

[b] Only segment multiplicity two.

**Table 5.4:** Measured transition energies from the argon isotopes $^{34,35}$Ar are compared to literature values from Ref. [15]. The energy assignment errors include only the statistical error from a Gaussian fit on linear background.

that the residual energy of the fragments measured by CATE can be used to achieve a mass dependence for few nucleon removal reactions. High transition energies were best resolved using Cluster detectors in the add-back mode. For the MINIBALL detectors the best results were obtained by requiring a segment multiplicity of two. With this knowledge the main goal of the experiment, the $2_1^+ \rightarrow 0_{g.s.}^+$ decay in $^{36}$Ca, can be tackled.

The mean energy deposition of $^{36}$Ca secondary beam fragments and the $^{37}$Ca secondary beam in the CATE CsI(Tl) detectors is calculated with the LISE++ code, yielding 5700 MeV and 5890 MeV, respectively. The residual energy $E_{res}$ of the $^{37}$Ca secondary beam is measured in the CATE CsI(Tl) detectors at channel 2260 using the scaled down FRS singles trigger, see Fig. 5.16. To get the centroid of the distribution of the $^{36}$Ca fragments, this value is scaled by the calculated energy depositions of $^{36}$Ca and $^{37}$Ca ($\frac{5700}{5980}$) and yields a channel number of 2187. The upper bound for the gate of $^{36}$Ca is then set in between the centroids of $^{36}$Ca and $^{37}$Ca at channel 2225. As the calculated EPAX cross-section for $^{35}$Ca is very low compared to $^{36}$Ca ($\frac{\sigma^{35}\mathrm{Ca}}{\sigma^{36}\mathrm{Ca}} = 0.007$) the lower bound of the gate for $^{36}$Ca is set to channel 2100. For the $^{37}$Ca secondary beam the window for the residual energy $E_{res}$ is set between channel 2225 and 2350.

The Doppler corrected $\gamma$-ray spectra obtained for the Cluster detectors are shown in Fig. 5.17 for residual energy $E_{res}$ cuts on the $^{37}$Ca secondary beam and the $^{36}$Ca reaction channel. The spectra are further distinguished between single hit and add-back events. The single hit spectra of $^{37}$Ca shows some structure around 3 MeV but no distinct peaks. For

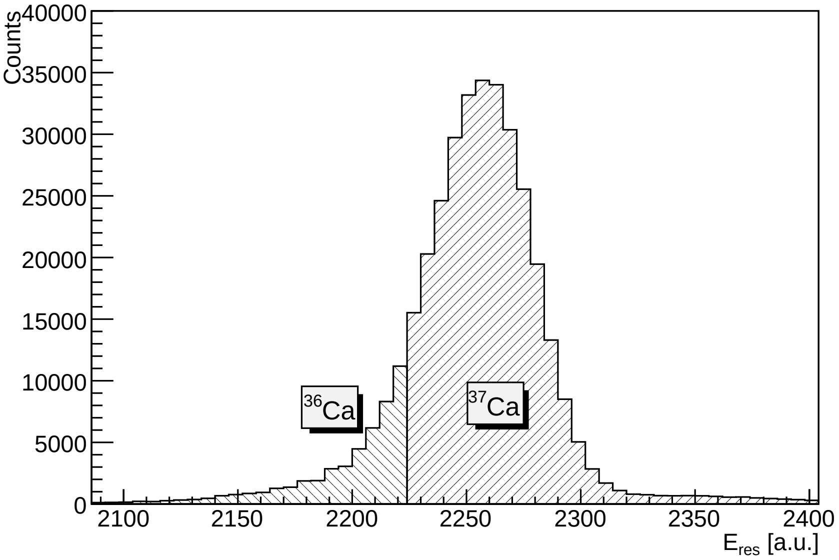

**Figure 5.16:** Measured residual energy $E_{res}$ of the $^{37}$Ca secondary beam in the CATE CsI(Tl) detectors using the scaled down FRS singles trigger. The gates applied for $^{36}$Ca and $^{37}$Ca in coincidence with prompt $\gamma$-rays are shown by the hatched areas.

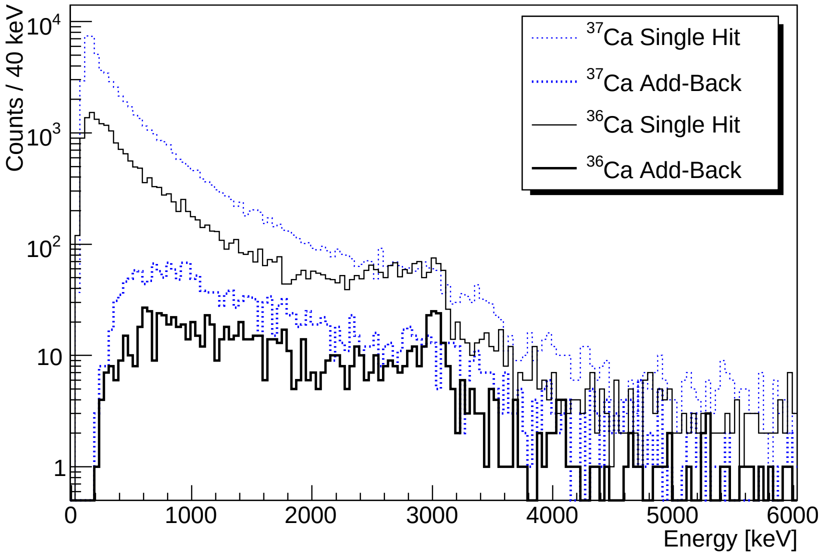

**Figure 5.17:** Doppler corrected $\gamma$-ray Cluster spectra with gates imposed on $^{36}$Ca (black solid) and $^{37}$Ca (blue dotted). The single hit (thin) and add-back (thick) events are shown separately.

the single hit spectra of $^{36}$Ca this structure is enhanced, showing a shoulder at 3050 keV. For the add-back spectra of the $^{36}$Ca reaction channel a peak at 3014(17) keV is visible.

In Fig. 5.18 the MINIBALL Doppler corrected $\gamma$-ray spectra for the $^{37}$Ca secondary beam and the $^{36}$Ca reaction channel are shown. The spectra are distinguished between segment multiplicity one and two events. The segment multiplicity two case of the $^{36}$Ca gate shows a peak at 3017(18) keV. A strong peak at 200 keV is observed for the $^{37}$Ca segment multiplicity one spectrum. This peak corresponds to expected bremsstrahlung radiation from the secondary target. Its absence for the $^{36}$Ca gate is accounted for as an indication for a good mass separation.

The final excitation spectra of $^{36}$Ca are shown in Fig. 5.19 for all three $\gamma$-ray detector systems, with the Cluster detectors used only in the add-back mode and the MINIBALL detectors only for events with a segment multiplicity of two. The $2_1^+ \rightarrow 0_{g.s.}^+$ transition is observed at an energy of 3014(17) keV with an energy resolution of 4.3(6) % for the Cluster detectors and at 3017(18) keV with an energy resolution of 4.9(10) % for MINIBALL. These energy resolutions are close to the simulated values of 3.8 % and 4.5 %, respectively.

For the combined MINIBALL and Cluster Ge detectors the statistical error is determined to 15 keV. Including an error of 5 keV in the energy assignment for observed known high energy transitions the $2_1^+ \rightarrow 0_{g.s.}^+$ transition in $^{36}$Ca is determined to 3015(16) keV. The spin assignment is based on a comparison to the mirror nucleus and on shell model calcu-

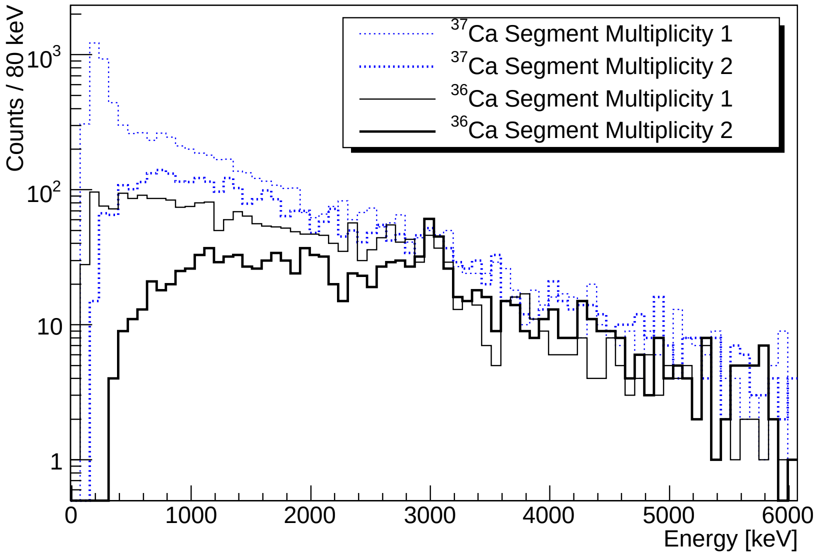

**Figure 5.18:** Doppler corrected $\gamma$-ray MINIBALL spectra with gates imposed on $^{36}$Ca (black solid) and $^{37}$Ca (blue dotted). The spectra for multiplicity one (thin) and multiplicity two (thick) events are shown separately.

lations which will be discussed in the next chapter. For the HECTOR array the $2_1^+ \rightarrow 0_{g.s.}^+$ transition in $^{36}$Ca is observed at 3020(30) keV. This is in good agreement with the value obtained from the Ge detectors. The error of 30 keV for the HECTOR array includes the statistical error of 20 keV from the fit and the error of 20 keV from the energy calibration (See Ch. 4.2.3), added in quadrature.

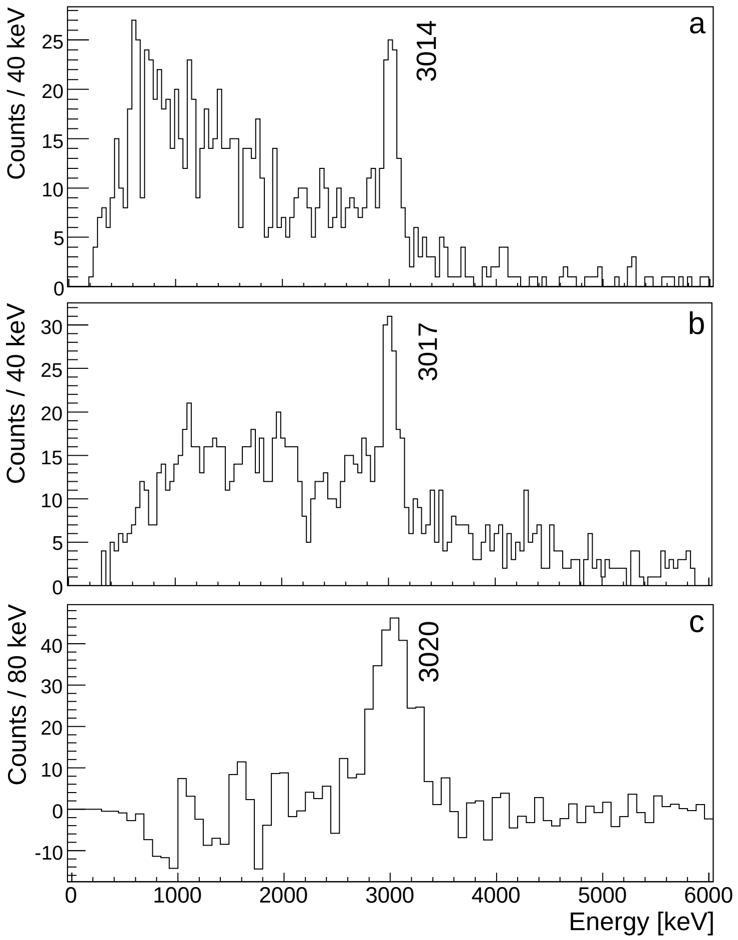

**Figure 5.19:** Doppler corrected $^{36}$Ca gated $\gamma$-ray spectra measured with the Cluster (a), MINIBALL (b), and HECTOR (c) detectors. For the HECTOR array the background was subtracted.

# 6 Shell Model Calculations and Discussion

The most important result of the described two step fragmentation experiment is the new value of the first excited $I^{\pi} = 2_1^+$ state in $^{36}$Ca. Beside the comparison of the absolute excitation energy value of $E(2_1^+) = 3015(16)$ keV with theoretical predictions of shell model calculations also the comparison with the mirror nucleus $^{36}$S, consisting of 16 protons and 20 neutrons, is of high interest with respect to isospin symmetry breaking effects in very neutron deficient nuclei. The comparison with the isospin $T = 2$ mirror nucleus $^{36}$S shows an experimental mirror energy difference of $\Delta E_M = E(^{36}\mathrm{Ca}) - E(^{36}\mathrm{S}) = 3015(16) - 3291 = -276(16)$ keV between the excitation energies of the two $I^{\pi} = 2_1^+$ states. For strict isospin symmetry the mirror energy difference should be zero. Small mirror energy differences are caused by the isospin breaking Coulomb interaction which is different for mirror partners. These differences are calculated to be of the order of tens of keV for *sd* shell nuclei with $Z = 8$ to $Z = 20$. The mirror energy difference value for the $^{36}$Ca–$^{36}$S pair is surprisingly large and about a factor of 5 – 10 larger than mirror energy differences $\Delta E_M$ observed for $T = 1$ states in the *sd* shell [15] and in the heavier $f_{7/2}$ shell [92, 93]. Even more surprising is that the Coulomb energy difference for the corresponding $T = 2$ states in $^{36}$Cl is only $\Delta E_C = E(^{36}\mathrm{Cl}) - E(^{36}\mathrm{S}) = -27(4)$ keV [94].

The experimental mirror energy differences $\Delta E_M$ of the known $I^{\pi} = 2_1^+$ states are summarised in Fig. 6.1 for the $1s0d$ shell and the adjacent $0p$ and $1p0f$ major shells. The Data shown in this figure are obtained from this work and Refs. [15, 93, 95, 96, 97, 98]. In general the isospin $T = 2$ mirror energy differences $\Delta E_M$ are larger than the $T = 1$ values, which may be due to the proton-rich partner lying closer to the dripline. The compilation shows that the $A = 36$ ($^{36}$Ca–$^{36}$S) and $A = 14$ ($^{14}$O–$^{14}$C) cases are obviously unique. In both cases the first excited $I^{\pi} = 2^+$ states of the proton-rich partners are already particle unbound and only the Coulomb barrier prevents fast proton decays.

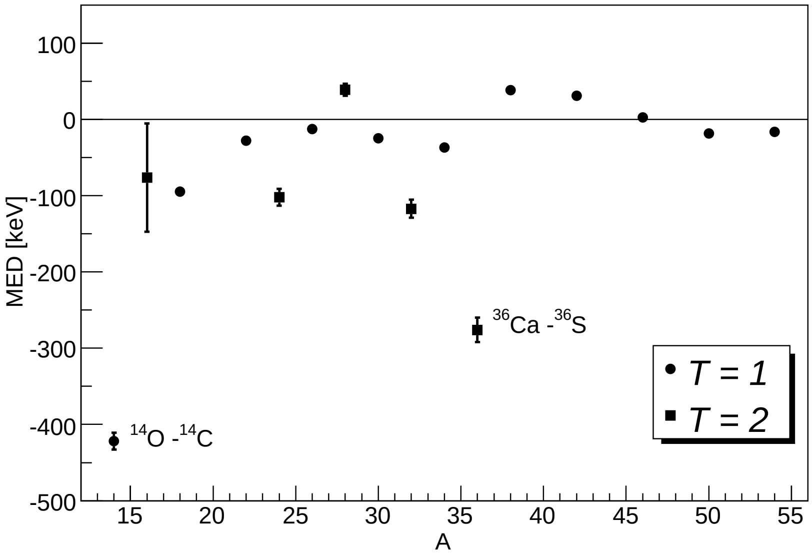

**Figure 6.1:** Experimental mirror energy differences ($\Delta E_M$) for the first $I^\pi = 2^+$ states of even-even isospin $T = 1$ (red circles) and $T = 2$ (blue squares) states from $^{14}$O–$^{14}$C to $^{54}$Ni–$^{54}$Fe. For references and details see text.

The large mirror energy difference $\Delta E_M$ certainly points to an effect due to shell structure and/or coupling to the continuum for the unbound state in the proton-rich partner ($S_p = 2.56(4)$ MeV for $^{36}$Ca and $S_p = 4.628$ MeV for $^{14}$O, respectively) and not to a Coulomb effect. This is supported by an inspection of the shell gap energies of the $A = 14$ and $A = 36$ mirror nuclei. The shell gap energies $\Delta_\pi$ and $\Delta_\nu$ are determined by the binding energy difference of a nucleus relative to its neighbouring isotopes and isotones, respectively:

$$\Delta_\nu(Z,N) = 2BE(Z,N) - BE(Z,N+1) - BE(Z,N-1) \tag{6.1}$$

$$\Delta_\pi(Z,N) = 2BE(Z,N) - BE(Z+1,N) - BE(Z-1,N). \tag{6.2}$$

They are given in Tab. 6.1 for the $A = 14$ ($^{14}$O–$^{14}$C) and $A = 36$ ($^{36}$Ca–$^{36}$S) mirror nuclei. For both pairs of mirror nuclei the proton rich partner exhibits the smaller subshell gap energy $\Delta_\nu$ relative to the subshell gap energy $\Delta_\pi$ of the neutron rich partner. Also the proton shell gap energy $\Delta_\pi$ in the proton rich partner is smaller than the corresponding neutron shell gap energy $\Delta_\nu$ of the neutron rich partner.

| Nucleus | $\Delta_\pi$ [MeV] | $\Delta_\nu$ [MeV] |
|---|---|---|
| $^{14}$O | 6.11(13) | 9.954(9) |
| $^{14}$C | 10.654 | 6.958 |
| $^{36}$Ca | 4.55(30) | 4.16(9) |
| $^{36}$S | 4.708(2)[a] | 5.585 |

---

[a] 4524(2) if Coulomb corrected.

**Table 6.1:** Proton and neutron subshell and shell gap energies $\Delta_{\pi,\nu}$ of the mirror nuclei $^{14}$O–$^{14}$C and $^{36}$Ca–$^{36}$S. The proton (neutron) gap energies $\Delta_\pi$ ($\Delta_\nu$) of the neutron rich nuclei $^{14}$C and $^{36}$S are larger than the corresponding neutron (proton) gap energies $\Delta_\nu$ ($\Delta_\pi$) of the proton rich nuclei $^{14}$O and $^{36}$Ca. The values are taken from Ref. [15].

## 6.1 Shell Model Calculations

In the recent past various shell model investigations for the neutron-rich *sd* shell region close to the "island of inversion" around $^{32}_{12}\mathrm{Mg}_{20}$ have been performed. They included excitations from the *sd* to the *pf* shell [36, 39, 40, 41, 42] and preserved full isospin symmetry. To investigate the mirror energy difference $\Delta E_M$ in the $A = 36$ mirror nuclei, the isospin symmetry has to be broken. In the hitherto first systematic attempt based on the USD interaction [99] the mirror energy differences $\Delta E_M$ were calculated for application to the astrophysical *rp* process [100]. In the $T = 2$ cases $A$ = 24, 32, and 36 the experimental results are largely underestimated by amounts of 70, 110, and 250 keV, respectively (see Fig. 6.4).

The USD interaction was derived for the *sd* model space. The parameters of the *sd* model space are the single-particle energies (SPE) $0d_{5/2}$, $1s_{1/2}$, and $0d_{3/2}$ and the two-body matrix elements (TBME) $\langle j_1, j_2|V|j_3, j_4\rangle_{JT}$, with $j_i \in (0d_{5/2}, 1s_{1/2}, 0d_{3/2})$, of the residual interaction Hamiltonian $H_{res}$. The energy eigenvalues $E_{J_i^\pi}$ of the Schrödinger equation for the residual Hamiltonian $H_{res}$ are functions of these parameters:

$$H_{res}\Psi_{J_i^\pi}(n) = E_{J_i^\pi}\Psi_{J_i^\pi}(n), \tag{6.3}$$

with $n$ being the number of valence nucleons between $^{16}$O and $^{40}$Ca. It is therefore possible to change the SPE and TBME in an iterative procedure by applying a least square fit of $E_{J_i^\pi}$ to experimental data until convergence is achieved. To reduce the computational effort instead of such a free fit in the *sd* shell a constrained fit of linear combinations of TBME

| Level | USD | USD*, USD$_1^m$ |
|---|---|---|
| $\pi 0d_{3/2}$ | +1647 | +4400 |
| $\pi 0d_{5/2}$ | -3948 | -600 |
| $\pi 1s_{1/2}$ | -3164 | -105 |
| $\nu 0d_{3/2}$ | +1647 | +942 |
| $\nu 0d_{5/2}$ | -3948 | -4143 |
| $\nu 1s_{1/2}$ | -3164 | -3272 |

**Table 6.2:** Single particle energies used in shell model calculations. The values are given in keV. For the original USD interaction the fitted isospin symmetric SPE are shown. In USD$^*$ the SPE are replaced by the experimental SPE of the $A = 17$, $T = 1/2$ mirror nuclei $^{17}$F and $^{17}$O.

was performed, resulting in the isospin symmetric USD interaction [99]. This interaction is the basis for the following shell model calculations.

As a shell model calculation is a complex mixture of systematic uncertainties due to model space, truncation, and interaction used the accuracy of a shell model calculation is difficult to estimate. In the case of the USD interaction, where the SPE and TBME were fitted to experimental data, the mean level deviation (MLD) can be used as a measure for the agreement between experiment and theory. The MLD is defined as [101]:

$$\mathrm{MLD} = \left[\frac{1}{n}\sum_i^n (E_i^{EX} - E_i^{SM})^2\right]^{1/2}, \tag{6.4}$$

with $n$ being the number of states compared. It is used in this work to judge the quality of modifications made to the USD interaction. The shell model calculations are performed with the code OXBASH [102].

In the first empirical approach to break the isospin symmetry in the *sd* shell the fitted isospin symmetric SPE from the original USD interaction are replaced by the experimental values of the $A = 17$, $T = 1/2$ mirror nuclei $^{17}$F and $^{17}$O. This interaction is referred to as USD$^*$. The SPE of the USD and USD$^*$ interactions are given in Tab. 6.2. The one proton separation energy in $^{17}$F is $S_p = 600$ keV, while the corresponding one neutron separation energy in $^{17}$O is $S_n = 4143$ keV. The reduced excitation energy of the $0s_{1/2}$ level in $^{17}$F of only 495 keV compared to its mirror nucleus $^{17}$O of 870 keV can be understood in terms of a Coulomb energy reduction of the loosely bound $s$ wave in $^{17}$F. Due to the lack of a centrifugal potential the repulsive Coulomb energy is reduced for a spatially extended

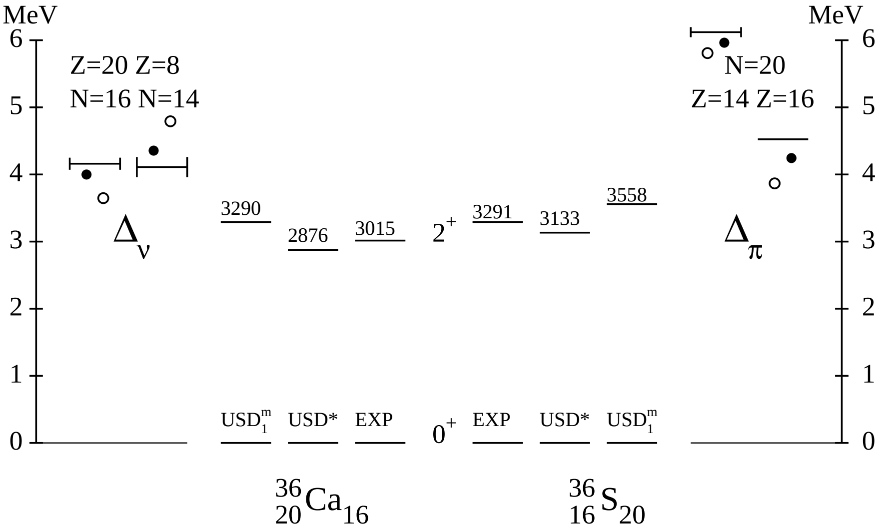

**Figure 6.2:** Experimental $^{36}$Ca and $^{36}$S (partial) level schemes in comparison to shell model calculations. Experimental single-particle energies from the $A = 17$, $T = 1/2$ mirror nuclei $^{17}$F and $^{17}$O are used for the USD interaction [103] (USD$^*$) and a monopole modified USD interaction based on Ref. [36] (USD$_1^m$ see text). The $1s0d$ shell model space subshell gaps $\Delta_{\pi,\nu}$ for $N = 14$ ($^{22}$O ), $N = 16$ ($^{36}$Ca), $Z = 14$ ($^{34}$Si) and $Z = 16$ ($^{36}$S) are shown as lines with error bars and compared to the corresponding shell model values as indicated by open (USD$^*$) and filled (USD$_1^m$) circles.

$s$ wave nucleon in $^{17}$F compared to the $d$ wave, resulting in the so-called Thomas-Ehrman shift [104, 105].

The use of the experimental $A = 17$, $T = 1/2$ SPE in the USD$^*$ interaction turns out to be the most crucial step in order to reproduce the large mirror energy difference $\Delta E_M$ of the first excited $2^+$ states in the $^{36}$Ca–$^{36}$S pair. No change is applied to the TBME of the USD$^*$ interaction relative to the original USD. Thus, the isospin symmetry in the TBME is preserved. For $^{36}$Ca the $2_1^+$ level lies at 2876 keV and for $^{36}$S the $2_1^+$ level lies at 3133 keV. This results in a mirror energy difference of $\Delta E_M = -257$ keV and is close to the experimental observation of $\Delta E_M = -276(16)$ keV. The subshell gaps $\Delta_\nu$ of $^{36}$Ca and $^{22}$O and $\Delta_\pi$ of $^{34}$Si and $^{36}$S are, however, not well reproduced, as can be seen in Fig. 6.2 and Tab. 6.3. The USD$^*$ interaction underestimates the subshell gap $\Delta_\nu$ of $^{36}$Ca by 513(90) keV and therefore the $I^\pi = 2_1^+$ excitation energy in $^{36}$Ca. The same applies for the mirror nucleus, i.e. the subshell gap $\Delta_\pi$ is underestimated by 657(2) keV and therefore the $I^\pi = 2_1^+$ excitation energy in $^{36}$S is too low. To get a picture of the quality of the USD$^*$ interaction at the boundaries of the $sd$ model space ($Z = 8, 20$ and $N = 20$), the USD$^*$

interaction can be compared to experimental data. Of particular interest are the $I^\pi = 2_1^+$ excitation energies and gap energies $\Delta_{\pi,\nu}$ of subshell closure nuclei and the $^{40}$Ca single-hole energies in $^{39}$Ca and $^{39}$K [106, 107]. The comparison is summarised in Tab. 6.3 and yields a mean level deviation of MLD = 422 keV for the USD$^*$ interaction, while the USD interaction yields MLD = 440 keV for the same data set.

To improve the large deviations observed for the subshell gap energies $\Delta_{\pi,\nu}$ with the USD$^*$ interaction, the monopole part of the TBME in the USD interaction can be modified. As a starting point the *sd* shell part modifications by by Utsuno *et al.* [36] are taken. These were made in Ref. [36] to make the nucleus $^{26}$O unbound against the two-neutron decay ($S_{2n} \leq 0$) in order to be in agreement with the experimental evidence [108, 109]. The pairing matrix element corrections of the *sd* shell applied in Ref. [36] are not used, since they were only utilised to include the $pf$ shell into the model space and to correct for effects of the $pf$ shell that are implicitly contained in the USD interaction. The SPE are again taken from the $A = 17$, $T = 1/2$ mirror nuclei $^{17}$F and $^{17}$O. To get a better agreement with the shell gap energy $\Delta_\nu$ in $^{22}$O and the shell gap energy $\Delta_\pi$ in $^{34}$Si, respectively, additional monopole corrections are applied. The total monopole modifications relative to the USD interaction are:

$$\delta V^{T=1,0}_{d_{5/2},d_{3/2}} = +0.20, -0.60\,\text{MeV} \tag{6.5}$$

$$\delta V^{T=1,0}_{d_{5/2},s_{1/2}} = -0.10, +0.10\,\text{MeV}. \tag{6.6}$$

This interaction keeps the isospin symmetry of the TBME and is hereafter referred to as USD$^m_1$. With this interaction $I^\pi = 2_1^+$ excitation energies of 3290 keV for $^{36}$Ca and of 3558 keV for $^{36}$Ca are obtained, yielding a mirror energy difference of $\Delta E_M = -268$ keV. The experimental data given in Tab. 6.3 are reproduced by the USD$^m_1$ interaction with a mean level deviation of MLD = 275 keV. In particular the subshell gaps given in this table are better reproduced with the USD$^m_1$ interaction than with USD$^*$, as shown in Fig. 6.2.

The striking result is that for both interactions, USD$^*$ and USD$^m_1$, the use of the experimental SPE from the $A = 17$, $T = 1/2$ mirror nuclei $^{17}$F and $^{17}$O almost fully accounts for the experimental mirror energy difference $\Delta E_M$ of the $I^\pi = 2_1^+$ state in the mirror nuclei . The mirror energy differences obtained from the USD$^m_1$ interaction ($\Delta E_M$ = –268 keV) and from the USD$^*$ interaction ($\Delta E_M$USD$^*$ = –257 keV) are in good agreement with the experimental mirror energy difference ($\Delta E_M$ = –276(16) keV). It can there-

| State | | Experiment | USD | USD* | USD$_1^m$ | USD$_2^m$ | USD$_3^m$ |
|---|---|---|---|---|---|---|---|
| | $3/2^+_{g.s}$ | 0 | 0 | 0 | 0 | 0 | 0 |
| $^{39}$Ca | $1/2^+_1$ | 2650 | 2731 | 2134 | 2610 | 2611 | 2610 |
| | $5/2^+_1$ | 6610 | 7418 | 6909 | 7068 | 7068 | 6168 |
| | $3/2^+_{g.s.}$ | 0 | 0 | 0 | 0 | 0 | 0 |
| $^{39}$K | $1/2^+_1$ | 2730 | 2731 | 2426 | 2901 | 2901 | 2901 |
| | $5/2^+_1$ | 6460 | 7418 | 6824 | 6983 | 6660 | 7283 |
| $^{36}$Ca | $2^+_1$ | 3015(16) | 3406 | 2876 | 3290 | 3290 | 3293 |
| $^{36}$S | $2^+_1$ | 3291 | 3406 | 3133 | 3558 | 3555 | 3558 |
| $^{34}$Si | $2^+$ | 3328/5041[a] | 4889 | 4597 | 4843 | 4524 | 5137 |
| $^{22}$O | $2^+_1$ | 3199(8) | 3376 | 3435 | 3067 | 3067 | 2477 |
| $^{24}$O | $2^+_1$ | $\geq$3600 | 4180 | 3650 | 5139 | 5139 | 5128 |
| $^{36}$Ca | $\Delta_\nu$ | 4160(90) | 4094 | 3647 | 3999 | 4001 | 4032 |
| $^{36}$S | $\Delta_\pi$ | 4524(2)[b] | 4094 | 3867 | 4244 | 4249 | 4237 |
| $^{22}$O | $\Delta_\nu$ | 4110(150) | 4699 | 4792 | 4355 | 4355 | 4122 |
| $^{34}$Si | $\Delta_\pi$ | 6120(75)[c] | 6068 | 5808 | 5963 | 5659 | 6241 |
| MLD (with $^{34}$Si $2^+_2$) | | | 440 | 422 | 275 | 311 | 362 |
| MLD (without $^{34}$Si $2^+_2$) | | | 458 | 420 | 281 | 289 | 377 |

---

[a] The level at 5041 keV has been observed in Ref. [110].

[b] 4709(2) if not Coulomb corrected.

[c] 6526(75) if not Coulomb corrected.

**Table 6.3:** Experimental level energies and gaps in comparison to shell model calculations using the USD interaction and different modifications. The experimental single hole states in $^{39}$Ca are obtained from a $^{40}$Ca(p,d) reaction [107] and the experimental single hole states in $^{39}$K are obtained from a $^{40}$Ca(d,$^3$He) reaction [106]. Special carefulness is required for the $2^+_1$ state of $^{34}$Si at 3328 keV which does not belong to the *sd* model space (See Ref. [36]).

fore be concluded that further Coulomb corrections beyond one-body contributions from the use of the experimental SPE from the $A = 17$, $T = 1/2$ mirror nuclei are negligible. In the nucleus $^{36}$Cl the two lowest isospin $T = 2$ states have been observed at 4300(1) keV for a $I^\pi = 0^+$ state and at 7564(4) keV for a $I^\pi = 2^+$ state [94]. Thus, the Coulomb energy difference of the observed isospin $T = 2$ states in $^{36}$Cl compared to $^{36}$S is $\Delta E_C = E(^{36}\mathrm{Cl}) - E(^{36}\mathrm{S}) = 3264(4) - 3291$ keV = –27(4) keV. With the USD$_1^m$ interaction the corresponding Coulomb energy difference for the same states is calculated and yields $\Delta E_C = -51$ keV. This deviation of several tens of keV is expected as no isospin breaking Coulomb correction has been applied to the TBME. It proves that the isospin projection number $T_z$ dependence for isospin $T = 2$ states in $A = 36$ nuclei is accounted for in the $\mathrm{USD}^m_1$ interaction. Furthermore, apart from the mirror energy difference $\Delta E_M$ and the sub-shell gaps $\Delta_\pi$ in $^{36}$Ca and $\Delta_\pi$ in $^{36}$S, which are robustly fixed by the $A = 17$, $T = 1/2$ SPE of the mirror nuclei $^{17}$F and $^{17}$O, the evolution of shell structure for the proton-rich ($^{36}$Ca) and the neutron-rich ($^{36}$S) partners is completely determined by the isospin symmetric two-body interaction, as expected for monopole driven shell structure [44, 43, 111].

## 6.2 Isospin Symmetry of $T = 1,2$ Nuclei in the *sd* Shell

The experimental large value of the mirror energy difference $\Delta E_M(2^+_1) = -276(16)$ keV for the isospin $T = 2$, $^{36}$Ca–$^{36}$S mirror pair is well reproduced with the USD$^*$ and $\mathrm{USD}^m_1$ interactions. This suggests a comparison for all experimentally known isospin $T = 1,2$ mirror energy differences of $2^+_1$ states in the *sd* shell. The results of the shell model calculations are given in Tab. 6.5. The mirror energy differences obtained for USD$^*$ and $\mathrm{USD}^m_1$ differ less than 25 keV from each other for all pairs of mirror nuclei in the *sd* shell. Now the deviations between the experimental mirror energy differences $\Delta E_M(2^+_1)$ and the results obtained from the $\mathrm{USD}^m_1$ interaction are discussed. A good agreement within 40 keV is found for isospin $T = 1,2$ mirror nuclei with the masses $A = 22, 26, 28, 34, 36$ and 38. The deviation of several tens of keV is expected due to the neglect of Coulomb corrections in the TBME. Large discrepancies between the experimental mirror energy difference $\Delta E_M(2^+_1)$ and the results from the $\mathrm{USD}^m_1$ interaction are found for $A = 18$ (63 keV), $A = 24$ (53(10) keV), $A = 30$ (105 keV), and $A = 32$ (215(12) keV). The calculation of Coulomb shifts in Ref. [100] fails to reproduce the experimental values except for $A = 28$, as shown in Fig. 6.4 together with the results obtained from the $\mathrm{USD}^m_1$ interaction. An empirical Coulomb correction applied to the proton $d_{5/2}$ and $d_{3/2}$ $J = 2,4$ TBME improves agreement at the beginning and end of shell but does not cure the $A = 24, 30, 32$ discrepancy. This and the inspection of the wave functions for the corresponding pairs of mirror nuclei suggest that the deviations are of structural origin.

An isospin symmetric monopole correction will not influence the mirror energy difference $\Delta E_M$. Moreover, due to the symmetry of the model space in protons and neutrons, any isospin asymmetric modification (which necessarily changes only the isospin $T = 1$ TBME) that shifts a proton (neutron) SPE in the lower half of the shell will have the same effect in the upper half, however with the difference that the corresponding nuclei lie on dif-

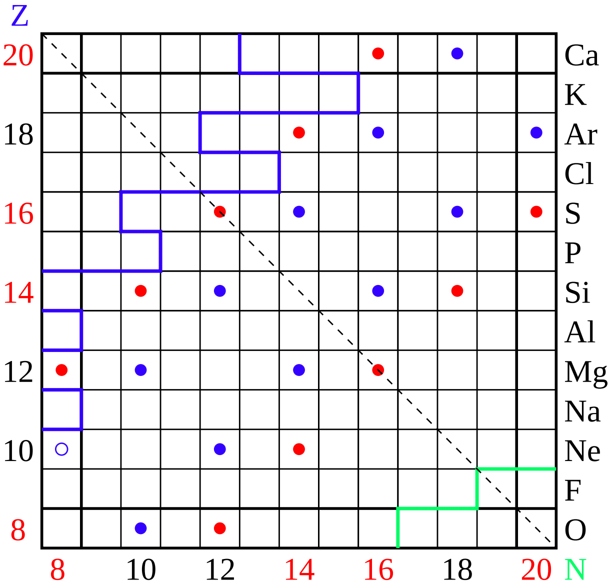

**Figure 6.3:** Isospin $T = 1,2$ nuclei in the *sd* shell. The isospin $T = 1$ ($T = 2$) nuclei are shown by the blue (red) points. The dashed line separates the two regions of the *sd* shell where different empirical ad hoc corrections are applied (See text for details). The blue (green) solid line shows the proton (neutron) drip-line.

ferent sides of the $N = Z$ line. Therefore, any mirror energy difference $\Delta E_M$ improvement in the upper *sd* shell ($A = 30,32$) will inevitably deteriorate the agreement in the lower shell ($A = 18 - 24$) and vice versa. The midshell mirror pair $A = 28$, however, which exhibits the only $T = 2$ positive $\Delta E_M$, will remain virtually unchanged. This value was recently measured [98] and is well reproduced in all approaches.

To get a better insight in the underlying structure, different empirical ad hoc corrections are made to the USD$_1^m$ interaction in two regions of the *sd* shell. The two regions are shown in Fig. 6.3. The first region is bordered by the $Z = 8$, $N = 8$ and the $A = 28$ isobar lines. The second region is bordered by the $Z = 20$, $N = 20$ and the $A = 28$ isobar lines.

- In the lower mass triangle $A = 16 - 28$ the $\pi 0d_{5/2}$ SPE are increased by 200 keV. In addition, the proton $0d_{5/2}^2$ TBME are quenched by 5 % to improve the USD$_1^m$ (and USD) agreement for $^{18}$Ne. The modifications result in a reduction of the proton gap $\Delta_\pi$ = 4.035 MeV in $^{22}$Si of 0.32 MeV relative to its mirror neutron gap $\Delta_\nu$ = 4.355 MeV in $^{22}$O. The interaction is referred to as USD$_2^m$.

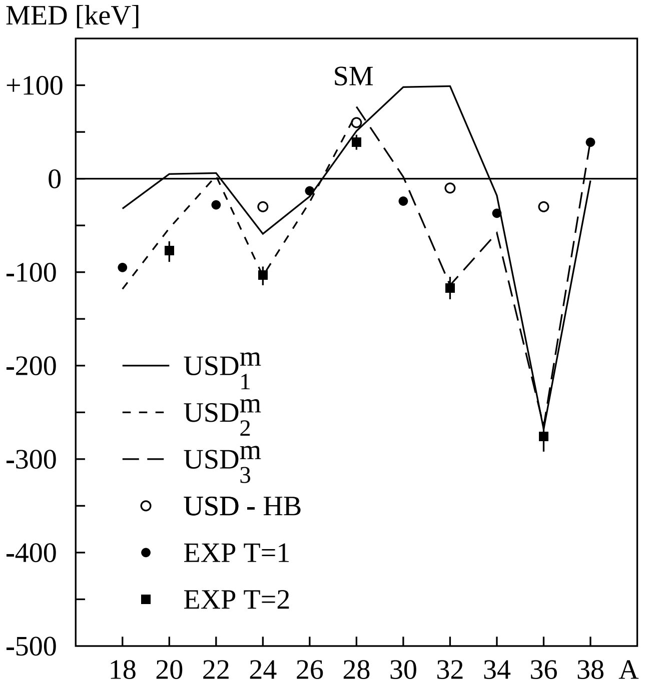

**Figure 6.4:** Experimental mirror energy differences for the first $I^\pi = 2^+$ states of even-even $T = 1$ (filled circles) and $T = 2$ (filled squares) *sd* shell mirror nuclei in comparison to shell model results of Ref. [100] (open circles) and the present work (USD$_1^m$) (full line). USD$_2^m$ (short dashed) corresponds to a reduced $Z = 14$ gap in the lower *sd* shell ($A \leq 28$). USD$_3^m$ (long dashed) corresponds to a increased $Z = 14$ gap and a reduced $N = 14$ gap in the upper *sd* shell ($A \geq 28$). For details see text.

- In the higher mass triangle $A = 28 - 40$ the $\pi 0d_{5/2}$ SPE are reduced by 300 keV and the $\nu 0d_{5/2}$ SPE are increased by 900 keV to further improve the agreement shown in Fig. 6.2. The modifications result in a reduction of 0.743 MeV of the $^{34}$Ca neutron gap ($\Delta_\nu$ = 5.498 MeV) relative to the $^{34}$Si proton gap ($\Delta_\pi$ = 6.241 MeV). Note that the $\Delta E_M$ are only sensitive to the gap difference. This interaction is referred to as USD$_3^m$.

The changes applied to the SPE are summarised in Tab. 6.4. The results are shown in Fig. 6.4 by short and long dashed lines for the lower and upper shell, respectively, and summarised in Tab. 6.5. The excellent agreement proves that the mirror energy difference $\Delta E_M$ are sensitive to the experimentally unknown proton gap $\Delta_\pi$ in $^{22}$Si and neutron gap $\Delta_\nu$ in $^{34}$Ca. Thus, the mirror energy difference $\Delta E_M$ is a usefull probe for shell structure in experimentally inaccessible regions. In the present approach the mirror energy difference

| Level | USD$_1^m$ | USD$_2^m$ | USD$_3^m$ |
|---|---|---|---|
| $\pi 0d_{3/2}$ | +4400 | +4400 | +4400 |
| $\pi 0d_{5/2}$ | -600 | -400 | -900 |
| $\pi 1s_{1/2}$ | -105 | -105 | -105 |
| $\nu 0d_{3/2}$ | +942 | +942 | +942 |
| $\nu 0d_{5/2}$ | -4143 | -4143 | -3243 |
| $\nu 1s_{1/2}$ | -3272 | -3272 | -3272 |

**Table 6.4:** Single particle energies used in the interactions USD$^m_{1,2,3}$. The values are given in keV. In USD$_1^m$ the SPE are taken from the experimental values of the $A = 17$, $T = 1/2$ mirror nuclei $^{17}$F and $^{17}$O. In USD$_2^m$ and USD$_3^m$ the SPE are adjusted to reproduce experimental levels in the lower and upper part of the shell, respectively. See text for details.

for the $^{20}$Mg–$^{20}$O pair is predicted to be $\Delta E_M$(USD$_2^m$) = -53 keV, which was very recently confirmed experimentally [112].

The substantial reduction of the neutron gap in $^{34}$Ca is corroborated by the experimental evidence in its isotone $^{32}$Ar of a reduced $\nu 0d_{5/2}$ occupation seen in neutron knockout reactions [113]. The origin of the reduction must be sought in the approaching dripline and gradual coupling to the continuum. The assumption of a constant ad hoc shift of the SPE in the upper (lower) *sd* shell is therefore only a crude approach. The quenching of the $d^2_{5/2}$ interaction in the lower *sd* shell, needed to reproduce the $\Delta E_M$, can be taken as first evidence for the reduced overlap of the protons involved due to coupling to the continuum.

| Mirror Pair | Exp. | USD* | $\mathrm{USD}_1^m$ | $\mathrm{USD}_2^m$ | $\mathrm{USD}_3^m$ |
|---|---|---|---|---|---|
| $^{18}$Ne–$^{18}$O | -95 | -25 | -32 | -118 | +25 |
| $^{20}$Mg–$^{20}$O | -77(10) | +1 | +5 | -53 | -74 |
| $^{22}$Mg–$^{22}$Ne | -28 | +5 | +6 | +3 | -32 |
| $^{24}$Si–$^{24}$Ne | -112(10) | -45 | -59 | -104 | +169 |
| $^{26}$Si–$^{26}$Mg | -13 | -17 | -19 | -24 | +90 |
| $^{28}$S–$^{28}$Mg | +39(8) | +27 | +51 | +70 | +77 |
| $^{30}$S–$^{30}$Si | -7 | +78 | +98 | +121 | +2 |
| $^{32}$Ar–$^{32}$Si | -117(12) | +82 | +98 | +155 | -114 |
| $^{34}$Ar–$^{34}$S | -37 | -22 | -18 | -10 | -58 |
| $^{36}$Ca–$^{36}$S | -276(16) | -257 | -268 | -265 | -265 |
| $^{38}$Ca–$^{38}$Ar | +39(5) | -3 | -2 | -10 | +40 |

**Table 6.5:** Calculated mirror energy differences $\Delta E_M$ of $2_1^+$ levels in $T = 1, 2$ nuclei of the *sd* shell for modified USD interactions. The experimental $\Delta E_M$ values are from this work and Ref. [15, 96, 97, 98, 112]. For further details see text.

# 7 Lifetime Measurements in Fragmentation Reactions

For fragments reaching the secondary target at the final focal plane of the FRS, peripheral reactions can be exploited for in-beam $\gamma$-ray spectroscopy in order to gain new nuclear structure information. A secondary target of a high $Z$ value, like Au or Pb, enables relativistic Coulomb excitations of the secondary beam. Alternatively, fragmentation reactions are best induced with a secondary target composed of low $Z$ values, like Be or C, to excite states in exotic nuclei. For the measurement of the $2^+_1 \rightarrow 0^+_{g.s.}$ transition energy of $^{36}$Ca this technique has been pioneered for secondary beam energies available with the FRS.

The target choice depends crucially on the interesting nuclear structure information: In the case of relativistic Coulomb excitation the excitation strengths of low spin states, i.e. $B(E2; 2^+_1 \rightarrow 0^+_{g.s.})$ values can be determined. Fragmentation reactions are better suited for the transfer of more angular momentum and higher excitation energies, so that new levels can be identified.

For the investigation of radioactive nuclei, the fragmentation reaction cross-section can compete with Coulomb excitation cross-sections and may yield higher count rates for the transition of interest. This is demonstrated in Tab. 7.1 for excitations in $^{36}$Ca. The two-step fragmentation ($^{40}\mathrm{Ca} \rightarrow {}^{37}\mathrm{Ca} \rightarrow {}^{36}\mathrm{Ca}^*$) yields an order of magnitude higher event rate than a fragmentation followed by a Coulomb excitation ($^{40}\mathrm{Ca} \rightarrow {}^{36}\mathrm{Ca} \rightarrow {}^{36}\mathrm{Ca}^*$).

The excitation strength is potentially accessible in fragmentation reactions via the $\gamma$-ray line shape and the dependence on the lifetime of the excited state ($\tau \sim B(E2)^{-1}$), as will be shown in this chapter. The interplay between the $\gamma$-ray line shape and the lifetime is closely connected to the experimental setup. The lifetime of an excited state has an influence on the fragment velocity and the decay position at the moment of $\gamma$-ray emission. This affects the Doppler corrected energy $E_{\gamma 0}$ of Eq. 4.7. Therefore, at first the lifetime dependence of the

| Primary Fragment | Fragmentation Cross Section [b] | $N_T$ [cm$^{-2}$] | Reaction Cross Section [b] | Event rate [s$^{-1}$] |
|---|---|---|---|---|
| $^{37}$Ca | 3.9*10$^{-5}$ | 6.7*10$^{22}$ (Be) | 1.8*10$^{-3}$ (fragmentation) | 0.32 |
| $^{36}$Ca | 1.4*10$^{-6}$ | 3.0*10$^{21}$ (Au) | 0.1 (Coulomb excitation) | 0.03 |

**Table 7.1:** Calculated reaction rates for secondary fragmentation ($^{37}$Ca + $^{9}$Be(1g/cm$^2$) $\rightarrow$ $^{36}$Ca$^*$) and Coulomb excitation ($^{36}$Ca + $^{197}$Au(1g/cm$^2$) $\rightarrow$ $^{36}$Ca$^*$) based on EPAX calculations. The number of secondary target nuclei is given by $N_T$. For the primary fragmentation a $^{40}$Ca ($10^9$ [s$^{-1}$]) beam impinges on a $^9$Be target (1g/cm$^{-2}$). Transmission losses of the FRS are not included.

velocity position and decay position is discussed. Afterwards, its application for RISING measurements with relativistic beams will be emphasised and experimental results of $^{34}$Cl and $^{36}$K will be discussed. Finally, lifetime effects on the line shapes will be presented.

## 7.1 Lifetime Dependence of Velocity Distribution and Decay Position

Experiments performed with secondary unstable beams may suffer from low beam intensities and low count rates. At relativistic beam velocities this can be partially counterbalanced by using thick secondary targets. This implies a considerable time of flight through the target of several ps, e.g. 23 ps for the $^{37}$Ca secondary beam striking at 195.7 $A$ MeV on a 700 mg/cm$^2$ $^9$Be target. For short-lived states in the pico-second range the particles may decay within the target during the slowing down process. Therefore, the velocity distribution of the fragments at the time of $\gamma$-ray emission might be spread out up to $\Delta\beta \approx 5$ %. At the same time the $\gamma$-ray emission takes place at different positions along the fragments flight path, which augments the uncertainty $\Delta\vartheta_\gamma$.

As the fragments are scattered under very small angles (Z-axis along 0°), the Cluster detectors in the forward hemisphere are only sensitive to the velocity distribution. For the MINIBALL detectors, which are positioned at angles perpendicular to the beam axis, the various Z-positions of the $\gamma$-ray emission points lead to a change of the $\gamma$-ray emission angle $\vartheta_\gamma$. These effects hamper the precise Doppler correction. However, if the unshifted transition energy is known from previous measurements, a lifetime information can be deduced.

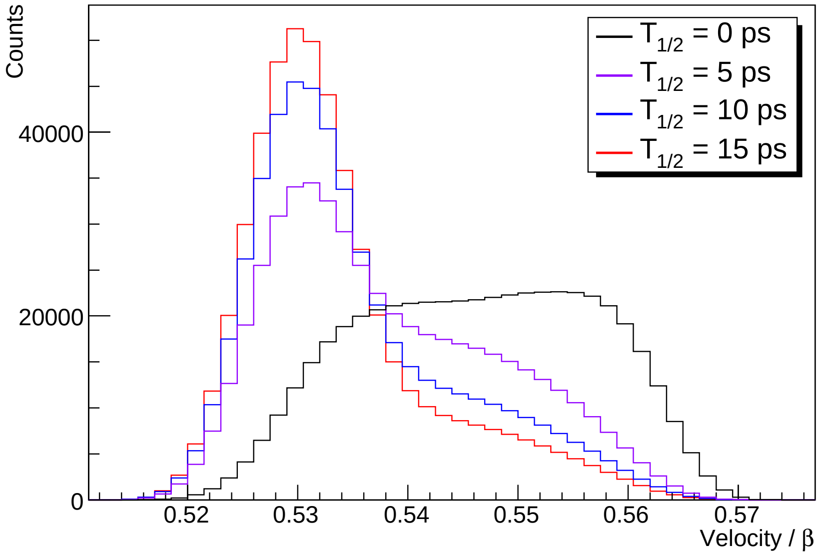

**Figure 7.1:** Simulated velocity ($\beta$) distributions for $^{36}$K assuming different halflives of an excited state. The velocity value at the moment of decay is shown. See text for details.

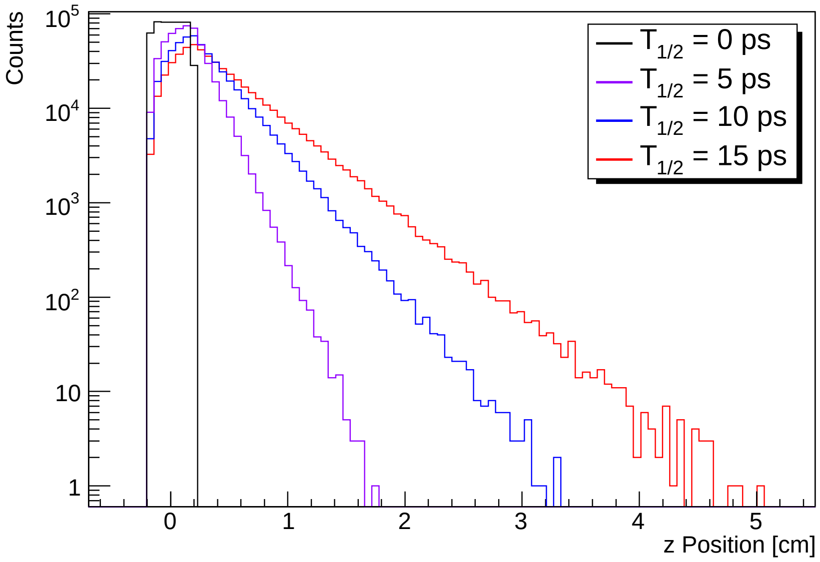

**Figure 7.2:** Simulated decay distributions of the emission point along the beam axis for $^{36}$K assuming different halflives of an excited state. See text for details.

Fig. 7.1 and Fig. 7.2 show the decay distributions as a function of both parameters: The fragment velocity $\beta$ and the Z-position of the $\gamma$-ray emission. The spectra are based on GEANT4 simulations of a $^{37}$Ca secondary beam with an energy of 195.7 *A* MeV striking on the 700 mg/cm$^2$ $^9$Be target, as it is used in the experiment. The resulting Z-positions along the beam axis and $\beta$ values at the point and moment of decay are shown for the 1p-removal reaction towards $^{36}$K. The calculations are done for four halflife values of 0, 5, 10, and 15 ps, respectively. It is assumed that the reaction cross-sections do not depend on the beam energy.

A nuclear state with a virtual 0 ps halflife exhibits a very broad $\beta$ distribution because the decay occurs in the target at the moment of reaction and production time. As the lifetime of an excited state grows its decay shifts more and more to times when the heavy ion has already passed the full target. As a consequence, the width of the $\beta$ distribution reduces for long lifetimes. For the position distribution at the moment of decay the situation is the complete opposite. For a short halflife the point of decay is restricted to the target position, while for long halflives the decay is spread over several cm.

Depending on the lifetime the mean values of the velocity and Z-position distribution, $<\beta>$ and $<Z>$, are shifted (which are the main characteristics of the lifetime measurement). Fig. 7.3 shows for the two fragmentation products $^{36}$K and $^{34}$Cl the $<\beta>$ shift as a function of the halflife, while Fig. 7.4 depicts the dependence of the $<Z>$ position. The difference in the $<\beta>$ curve for the two fragmentation products in Fig. 7.3 is caused by the specific energy loss which scales with $Z^2$ (See Eq. 3.11). A small difference originates

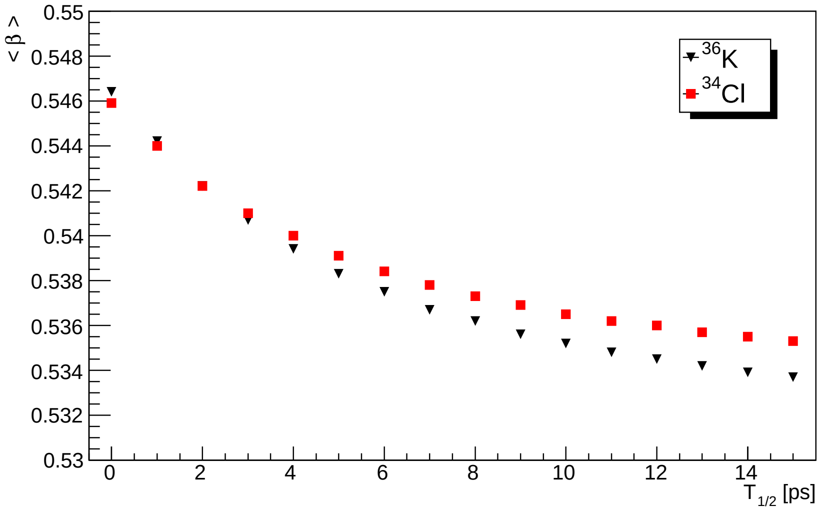

**Figure 7.3:** Simulated mean $<\beta>$ velocity for $^{36}$K and $^{34}$Cl assuming different halflives of an excited state. See text for details.

from the ablation process, causing lighter fragmentation products to have smaller $\beta$ values, which is visible at very short halflives.

In the following sections the lifetime effects will be studied for excited states in $^{34}$Cl and $^{36}$K.

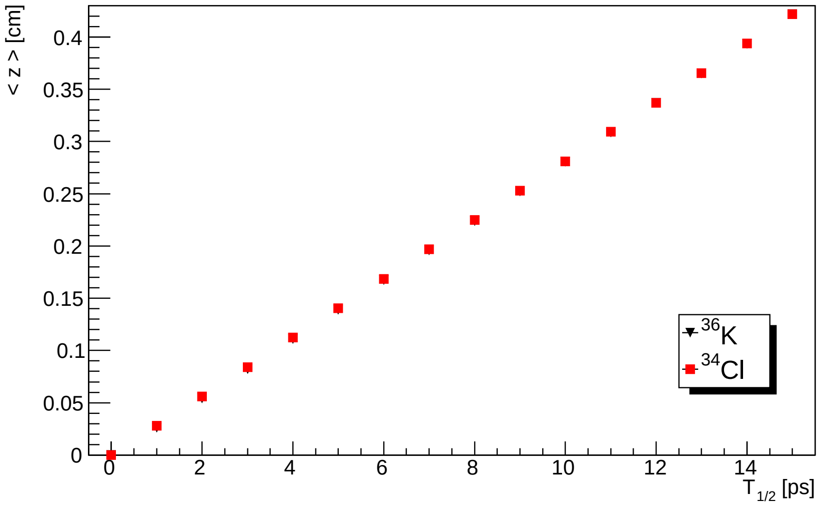

**Figure 7.4:** Simulated mean $< Z >$ position for $^{36}$K and $^{34}$Cl assuming different halflives of an excited state. See text for details.

## 7.2 Lifetimes in $^{34}$Cl Measured by Peak Shifts

The observed $\gamma$-ray spectra of chlorine fragmentation products are displayed in Fig. 7.5 for the Cluster array and in Fig. 7.6 for the MINIBALL detectors. The partial level scheme corresponding to the observed decays of $^{34}$Cl is displayed in Fig. 7.7.

The spectra are Doppler corrected with a velocity of $\beta = 0.5389$ that corresponds to the halflife of 5.2(3) ps for the excited $1_1^+$ level of $^{34}$Cl decaying into the $0^+$ ground state by emitting a 461 keV $\gamma$-ray [15]. The decay is, however, disturbed by the feeding of a higher lying $2_1^+$ state with a halflife of 13.7(9) ps. This feeding state has a branching into the $1_1^+$ state and into the $1_2^+$ state. The latter state has a halflife of 9.1(6) ps and decays by a 666.5 keV $\gamma$-transition into the ground state [15]. The $1_1^+ \rightarrow 0_{g.s.}^+$ and $1_2^+ \rightarrow 0_{g.s.}^+$ decays are well observed in both detector systems and their halflives in the ps-range allow for

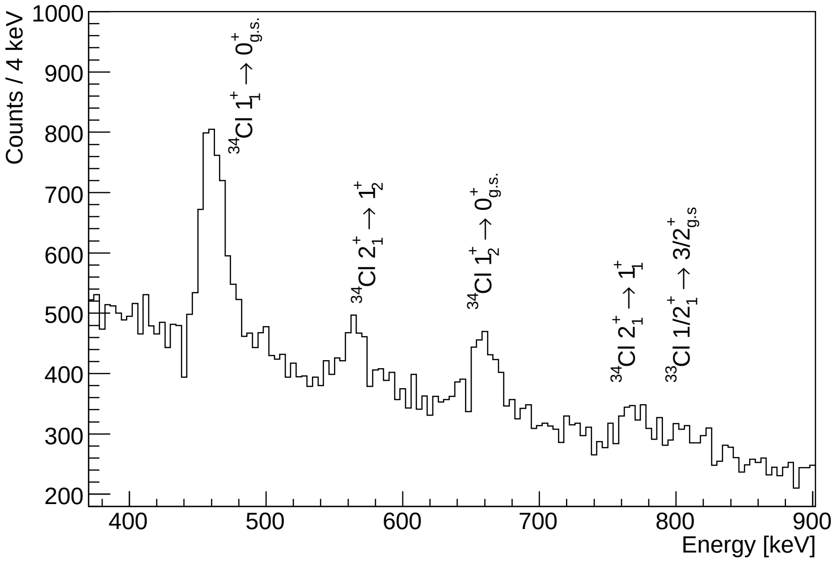

**Figure 7.5:** Doppler corrected Cluster $\gamma$-ray spectrum for the $^{33,34}$Cl reaction channels.

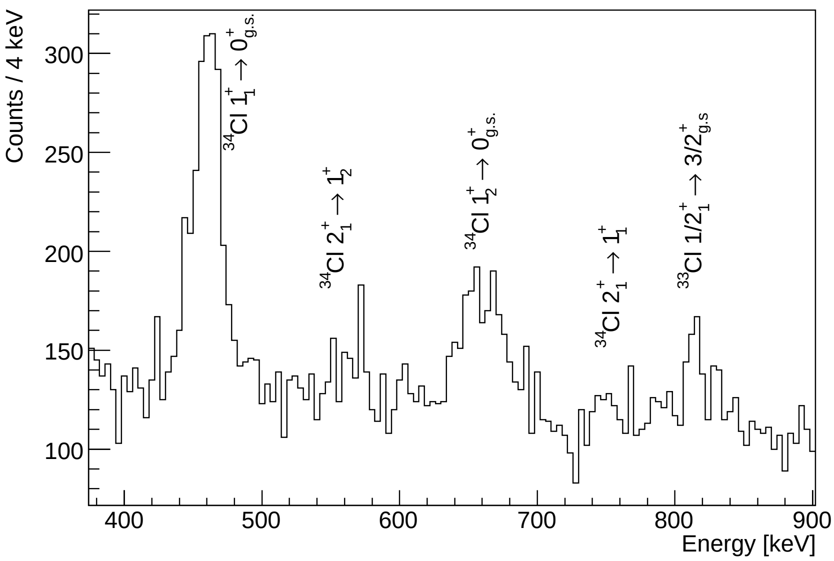

**Figure 7.6:** Doppler corrected MINIBALL $\gamma$-ray spectrum for the $^{33,34}$Cl reaction channels.

an investigation of the lifetime dependence for peak positions measured after applying a Doppler correction.

The feeding from the $2_1^+$ state into the $1_1^+$ and $1_2^+$ states has to be considered. The measured peak intensities of a combined Cluster and MINIBALL array are given in Tab. 7.2.

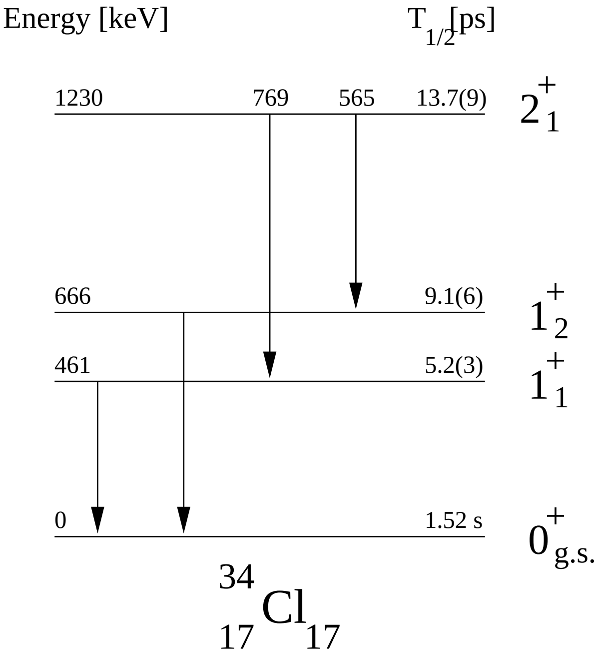

**Figure 7.7:** Partial level scheme of observed lines in $^{34}$Cl. The data are taken from Ref. [15].

From these intensities the the feeding from the $2_1^+$ state is determined to 15(4) % for the $1_1^+$ state and 33(10) % for the $1_2^+$ state. The different efficiencies for the observed $\gamma$-ray transitions are simulated and corrected for in the feeding determination. With the feeding the effective halflives increase to 7.3(6) ps for the $1_1^+$ state and to 13.8(15) ps for the $1_2^+$ state.

| Transition | Literature Energy | Fitted Area | Simulated Efficiency |
|---|---|---|---|
| $1_1^+ \rightarrow 0_{g.s.}^+$ | 461.00(4) | 2947 ± 166 | 1 |
| $2_1^+ \rightarrow 1_2^+$ | 564.72(5) | 515 ± 148 | 0.97 |
| $1_2^+ \rightarrow 0_{g.s.}^+$ | 665.55(5) | 1366 ± 176 | 0.93 |
| $2_1^+ \rightarrow 1_1^+$ | 769.27(5) | 348 ± 185 | 0.89 |

**Table 7.2:** Measured peak intensities in $^{34}$Cl for the combined Cluster and MINIBALL spectra. The intensities are deduced from a fit of a Gaussian distribution on top of a linear background. The simulated photopeak efficiency $\varepsilon_{peak}$ is normalised to the $1_1^+ \rightarrow 0_{g.s.}^+$ decay.

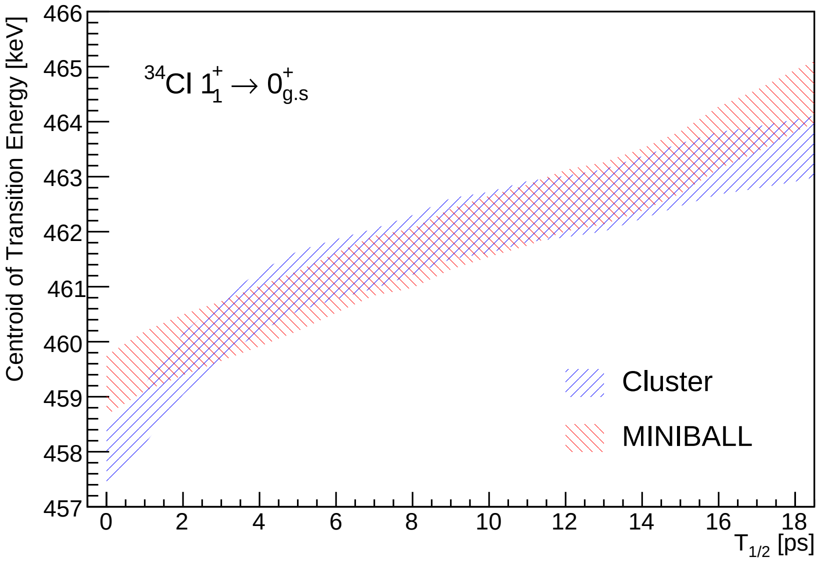

**Figure 7.8:** Doppler corrected $\gamma$-ray energy measured for the $1_1^+ \rightarrow 0_{g.s.}^+$ transition in $^{34}$Cl as a function of the halflife. The hatched area marks an error of $\pm\sigma$ in the energy assignment.

To investigate the lifetime effects, a series of Doppler shift corrections has to be performed for different $<\beta>$ velocities and $\gamma$-emission angles for halflives ranging from 0 to 20 ps. The $\gamma$-emission angles are calculated from the position of the $\gamma$-emission along the Z-axis ($<Z>$), from the heavy ion positions measured in the Si detectors after the target and CATE, and from the Ge detector positions.

As a result different Doppler corrected $\gamma$-ray energies are obtained for the $1_1^+ \rightarrow 0_{g.s.}^+$ decay as a function of the halflife as shown in Fig. 7.8. The hatched area marks the energy of the peak positions with an error band of $\pm\sigma$ as a function of the halflife. The 461.0 keV energy line is intersected for halflives of $5^{+2.0}_{-1.5}$ ps in the case of the Cluster detector and 6(2) ps for the MINIBALL array. This is close to the effective halflife of 7.3(6) ps that includes the observed feeding.

Noteworthy is the curvature of the measured Doppler corrected $\gamma$-ray energy as a function of the nuclear state halflife. The MINIBALL detectors are placed very close to the target at angles which are in the moving frame of the nucleus close to 90°. Therefore, only the different $<Z>$ values are accountable for the peak shift, while the influence of different $<\beta>$ values are marginal. The shift of the measured Doppler corrected $\gamma$-ray energy is, therefore, well described by a straight line as the $<Z>$ values (Fig. 7.4). This

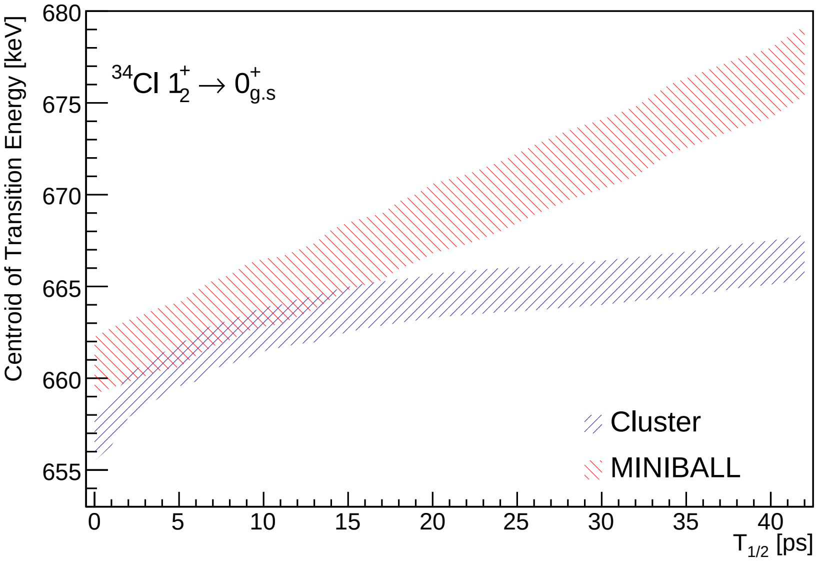

**Figure 7.9:** Doppler corrected $\gamma$-ray energy measured for the $1^+_2 \rightarrow 0^+_{g.s.}$ transition in $^{34}$Cl as a function of the halflife. The hatched area marks an error of $\pm\sigma$ in the energy assignment.

has the consequence that the MINIBALL detectors are sensitive to measure lifetimes also for higher values than 20 ps and lifetimes up to several hundred ps should be measurable. However, too long halflives have an influence on the energy resolution which will deteriorate.

Contrary to that, the Cluster detectors are mounted far away from the target at forward angles. Here, the Doppler corrected $\gamma$-ray energy is only changed by the different mean $\beta$-velocities. Thus, as for the $<\beta>$-velocity dependence (Fig. 7.3), the peak shift of the Cluster detectors will have the highest slope for very short halflives.

As a second example Fig. 7.9 depicts the Doppler corrected $\gamma$-ray energy of the $1^+_2 \rightarrow 0^+_{g.s.}$ decay as a function of the halflife. The peak positions of the MINIBALL array crosses the 665.55 keV line for a halflife of 13(5) ps, which is in agreement with the effective halflife of 13.8(15) ps that includes the observed feeding from the $2^+_1$ state. The peak positions of the Cluster array intersects the 665.55 keV line for a halflife of $32^{+10}_{-14}$ ps. For the given secondary beam energy and target thickness the Cluster detectors are not as sensitive to lifetime effects in this region as the MINIBALL array, as is seen by the different slopes of the two curves.

## 7.3 Lifetimes in $^{36}$K Measured by Peak Shifts

The cross-section ratio $\frac{\sigma^{36}K}{\sigma^{35}K} = 20$ is calculated for the one proton removal channel into potassium isotopes with the EPAX code. Therefore, mainly excitations of $^{36}$K are expected for the Doppler corrected $\gamma$-ray spectra obtained from potassium fragments. $^{36}$K has a known low-lying level at 800(15) keV [114]. This is the strongest observed $\gamma$-ray line for the Doppler corrected $\gamma$-ray spectra of the Cluster and MINIBALL detectors displayed in Fig. 7.10 and Fig. 7.11, respectively. From its mirror nucleus $^{36}$Cl (see Fig. 7.14) and shell model calculations using USD$^m_1$ it is expected that this is the $3^+_1 \rightarrow 2^+_{g.s.}$ transition.

The $3^+_1 \rightarrow 2^+_{g.s.}$ transition in $^{36}$Cl decays with an energy of 788.442(6) keV and a halflife of 13.8(12) ps [15]. Hence, also for the 800(15) keV state in $^{36}$K a halflife of several pico-seconds is expected. The error of 15 keV determined by Ref. [114] for this state has of course an influence on the lifetime determination. The Doppler corrected $\gamma$-ray energies are determined for assumed halflives in the range 0 to 20 ps. This is shown in Fig. 7.12. The hatched areas of the Cluster and MINIBALL arrays merge for an energy of 810(2) keV, while they diverge for lower and higher $\gamma$-ray energies. The present transition energy corresponds to a halflife of $8^{+5}_{-4}$ ps. This means that also for initially inexactly and unknown transition energies an effective lifetime can be deduced, since both curves have

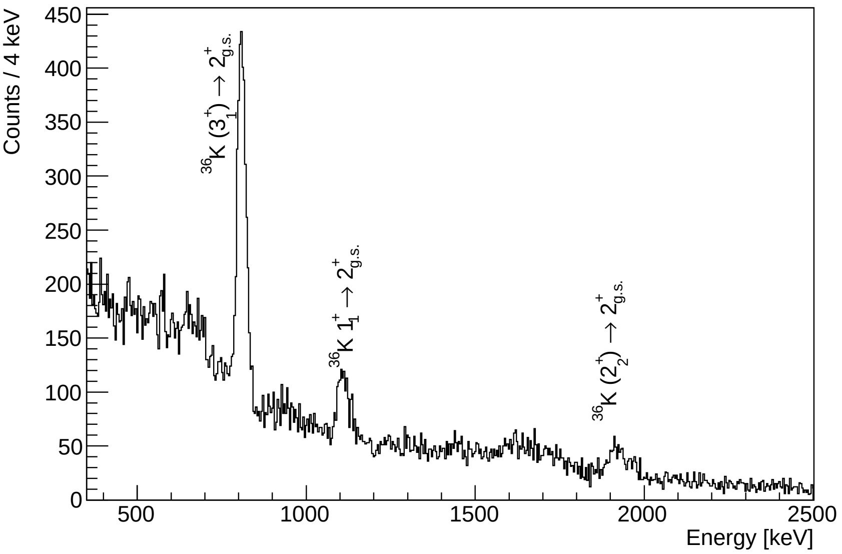

**Figure 7.10:** Doppler corrected Cluster $\gamma$-ray spectrum for the $^{36}$K reaction channel.

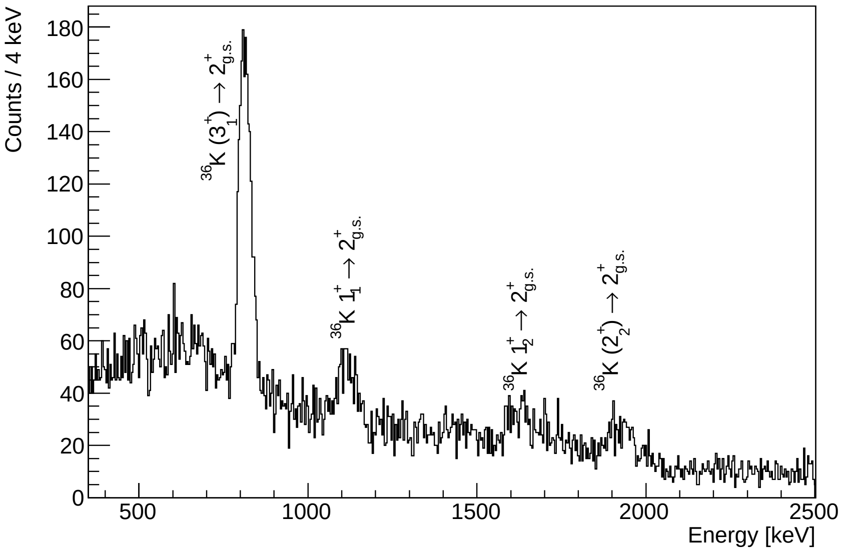

**Figure 7.11:** Doppler corrected MINIBALL $\gamma$-ray spectrum for the $^{36}$K reaction channel.

different slopes and the intersection point is at the correct transition energy and therefore at the corresponding lifetime of a de-exciting state.

In addition, the $1^+_1 \rightarrow 2^+_{g.s.}$ decay with a known energy of 1112.8(4) keV [115] is observed in the Doppler corrected $\gamma$-ray spectra of Fig. 7.10 and Fig. 7.11. In the mirror nucleus $^{36}$Cl this state decays with an energy of 1164.9 keV and a halflife of 6.4(4) ps [15]. Thus, for $^{36}$K a comparable halflife is expected. The Doppler corrected $\gamma$-ray energies are plotted in Fig. 7.13 as a function of the halflife. The Cluster detectors intersect the 1112.8 keV line with a halflife of $7^{+3}_{-2}$ ps. Due to the bigger error in the MINIBALL array only the lower edge of the hatched area crosses the 1112.8 keV line for a halflife of 9 ps.

A further decay in $^{36}$K is observed at an energy of 1914(4) keV for the Cluster and at 1915(6) keV for the MINIBALL detectors. This decay might correspond to the level already observed at 1890(20) keV [114]. In the mirror nucleus $^{36}$Cl the $2^+_2 \rightarrow 2^+_{g.s.}$ transition decays at an energy of 1959.412(5) keV and a halflife of 44(2) fs [15]. The assignment of a $2^+_2 \rightarrow 2^+_{g.s.}$ decay for the observed transition at 1915(5) keV for the combined MINIBALL and Cluster detectors is supported by shell model calculations using the USD$^m_1$ interaction. The complete observed level scheme of $^{36}$K is shown in Fig. 7.14 together with its mirror nucleus and results for shell model calculations using USD$^m_1$.

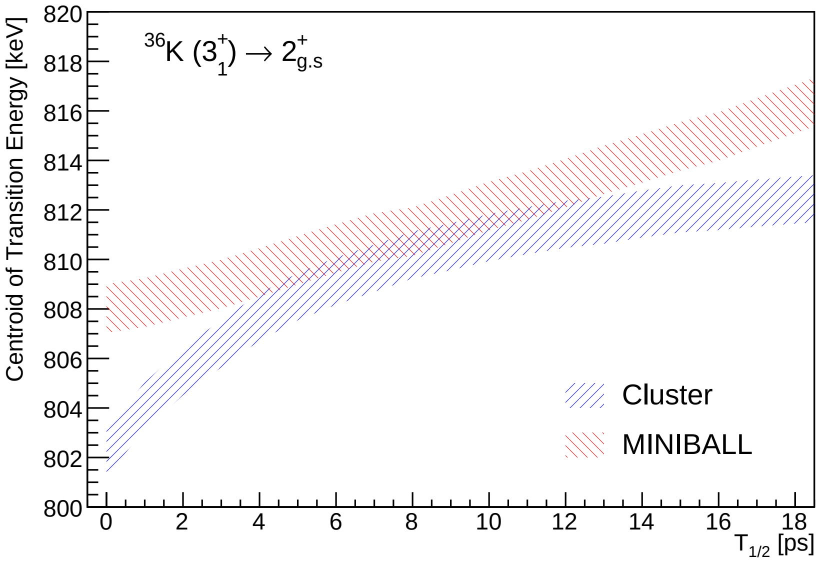

**Figure 7.12:** Doppler corrected $\gamma$-ray energy measured for the $(3_1^+) \rightarrow 2^+_{g.s.}$ transition in $^{36}$K as a function of the halflife. The hatched area marks an error of $\pm\sigma$ in the energy assignment.

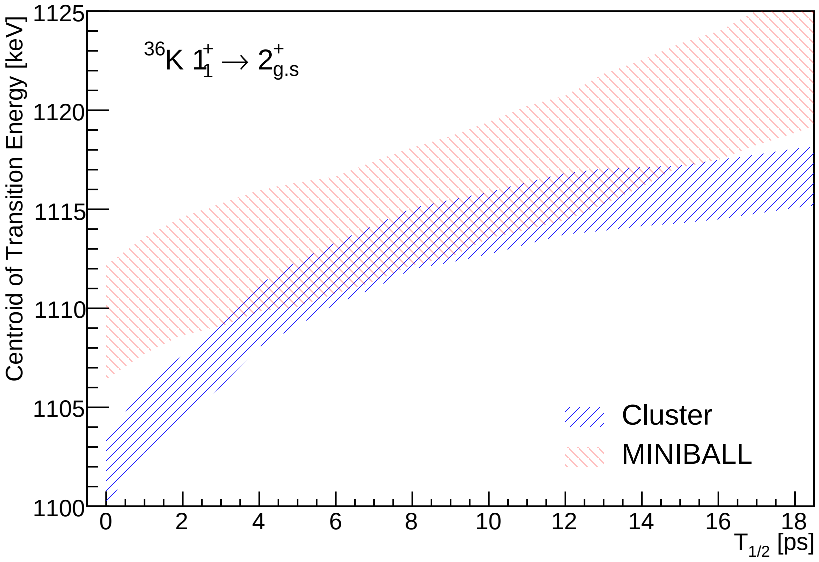

**Figure 7.13:** Doppler corrected $\gamma$-ray energy measured for the $1_1^+ \rightarrow 2^+_{g.s.}$ transition in $^{36}$K as a function of the halflife. The hatched area marks an error of $\pm\sigma$ in the energy assignment.

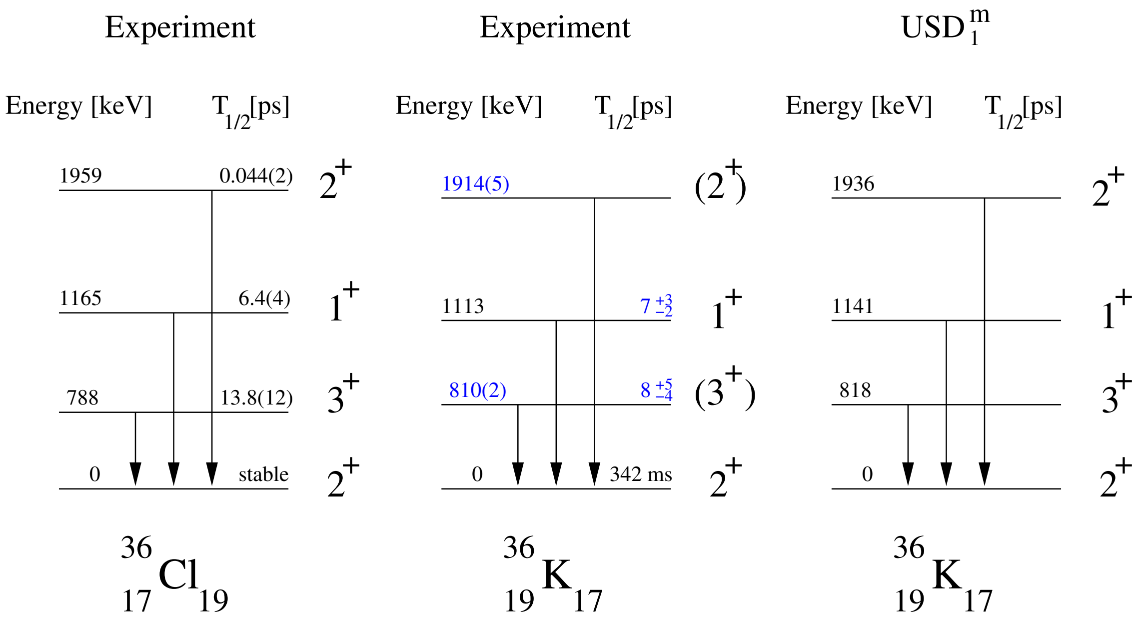

**Figure 7.14:** Observed level scheme of $^{36}$K (centre) in comparison with its mirror nucleus $^{36}$Cl (left) and shell model calculations using USD$_1^m$ (right). Results for energy transitions and halflives deduced from the present work are marked in blue. Known transition energies are taken from Ref. [15, 115].

## 7.4 Lifetime Effects on the Line Shape

The observed $\gamma$-ray spectra of $^{34}$Cl and $^{36}$K have an almost gaussian shape although the corresponding $\beta$-distribution has a very asymmetric tail towards higher values, as shown in Fig. 7.1. For a $^{37}$Ca beam with an incident energy of 195.7 $A$ MeV impinging on a 700 mg$^2$ $^9$Be target the opening angle of the detectors is the dominant factor for the $\gamma$-ray energy resolution and consequently also for the line shape. In order to enhance the effects on the line shape caused by the lifetime one has either to reduce the velocity or a thicker secondary target has to be inserted. Thus, several simulations are performed to demonstrate how crucial the choice of the beam energy and target thickness is. These simulations, shown in Fig. 7.15 for the Cluster detectors, deal with the decay of the $(3_1^+) \rightarrow 2_{g.s.}^+$ transition in $^{36}$K, produced in the fragmentation of $^{37}$Ca at a beam energy of 150 $A$ MeV, target thicknesses of 500 and 1000 mg/cm$^2$, and halflives of 0, 5, 10, and 15 ps, respectively.

For a target thickness of 500 mg/cm$^2$ the lifetime has only a negligible influence on the line shape. In all four simulated cases the curve possesses a gaussian shape. A slight increase of energy resolution from 3.2 % to 3.1 % is observed when going from short to longer halflives, as is expected due to the smaller $\beta$-spread. The situation changes dramatically for the 1000 mg/cm$^2$ target. Firstly, the use of the thick target deteriorates the energy resolution which is now 7 % for the 0 ps halflife spectrum. The striking result for the Cluster detectors is, however, that the observed $\gamma$-ray spectra resemble the $\beta$-curves shown in Fig. 7.1, implying that the $\beta$-uncertainty is the main cause for the line shape. Thus, as the Doppler corrections are performed with the mean $< \beta >$-velocity corresponding to the respective halflives, the centroids of the distributions remain at 810 keV for all halflives. However, with increasing halflife a narrow maximum below 810 keV emerges. Hence, if this effect is visible in experimental spectra, the line shape can be compared to simulated values and the lifetime of the excited state can be extracted.

As the dominant factor for the line shape is the $\beta$-distribution it will be most pronounced for detectors positioned at extreme forward and backward angles. For the MINIBALL detectors, which are positioned almost perpendicular to the beam direction, the line shape is hardly influenced by changing the target thickness, as shown in Fig. 7.16. For the 1000 mg/cm$^2$ target the $\gamma$-ray energy resolution of 5.2 % is slightly worse than for the 500 mg/cm$^2$ of 4.4 %. The opening angles of the MINIBALL detectors are still dominat-

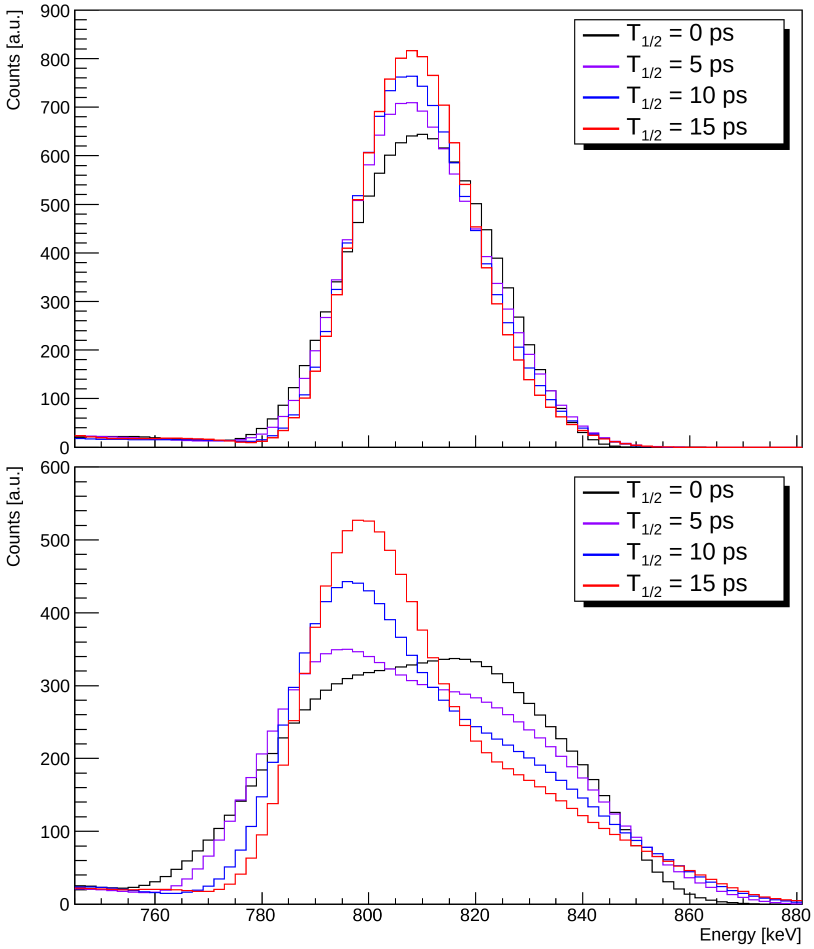

**Figure 7.15:** Simulations of the Cluster $\gamma$-ray line shape for the $(3_1^+) \rightarrow 2_{g.s.}^+$ transition in $^{36}$K and target thicknesses of 500 mg/cm$^2$ (upper panel) as well as 1000 mg/cm$^2$ (lower panel) at a beam energy of 150 $A$ MeV.

ing the line shape and therefore the distribution remains virtually unchanged for different halflives.

In summary, it has been shown that determinations of transition energies in relativistic two-step fragmentation experiments need to consider lifetime effects, since the mean velocity $<\beta>$ and the decay position $<Z>$ along the beam direction depend on the lifetime. If the transition energy is known, the lifetime of the initial state can be obtained by applying Doppler corrections that include these effects. The adjusted $\gamma$-ray energy has to match the literature value, which also defines the corresponding lifetime of the initial state. For unknown transition energies lifetime values are obtained by comparing the peak

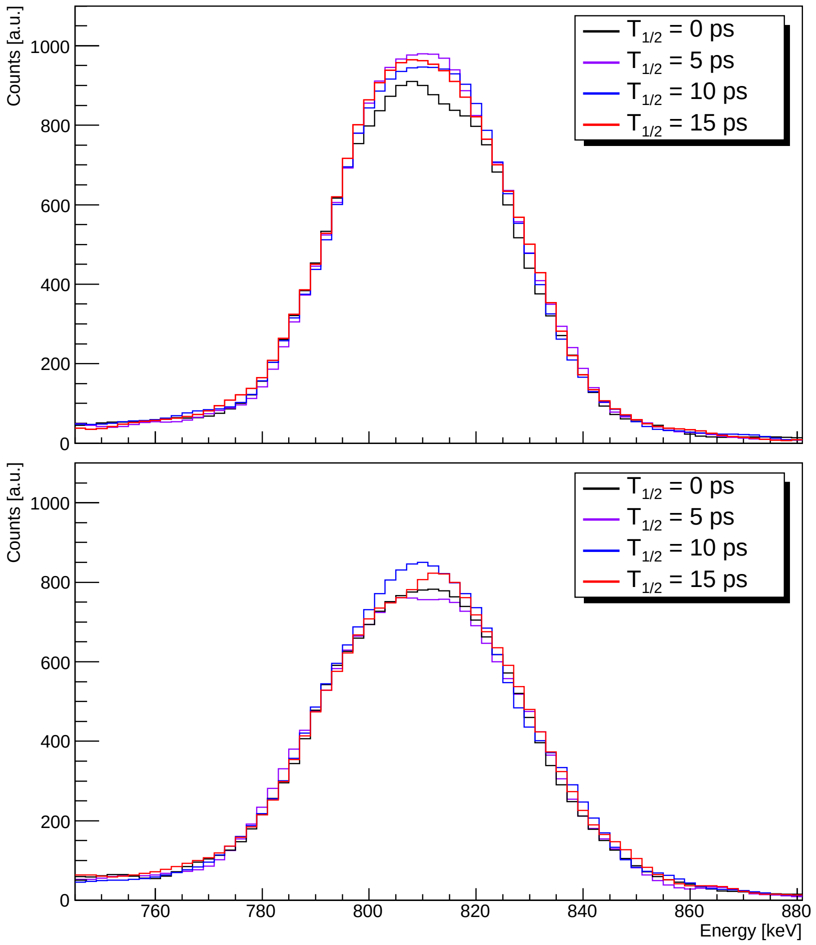

**Figure 7.16:** Simulations of the MINIBALL $\gamma$-ray line shape for the $(3_1^+) \rightarrow 2_{g.s.}^+$ transition in $^{36}$K and target thicknesses of 500 mg/cm$^2$ (upper panel) as well as 1000 mg/cm$^2$ (lower panel) at a beam energy of 150 $A$ MeV.

shifts for $\gamma$-ray detectors at different $\vartheta_\gamma$ angles. Since the Doppler corrected $\gamma$-ray energies as a function of halflife have different slopes, the intersection point leads to the correct transition energy and lifetime. From an analysis of the $\gamma$-ray lineshape the lifetime of a state can be determined. This requires, however, that lifetime effects are large compared to other effects, as the detector opening angle. With the advent of new position sensitive $\gamma$-ray detectors as the AGATA array [116] relativistic two-step fragmentation experiments will almost automatically provide the lifetime of excited states.

# 8 Summary

In the presented work all aspects of an experiment utilising in-beam $\gamma$-ray spectroscopy of two step fragmentation reactions at relativistic energies have been discussed. The aim of the experiment was to investigate that the $N = 14(16)$ shell stabilisation in $Z = 8$ oxygen isotopes and the $N = 20$ shell quenching in $^{32}$Mg are symmetric with respect to the isospin projection quantum number $T_z$. Of special interest was the excitation energy of the $2^+_1 \rightarrow 0^+_{g.s.}$ decay in the very neutron deficient $^{36}$Ca.

As the fragment separator FRS enables unprecedented secondary beam energies for in-beam $\gamma$-ray spectroscopy of up to 1 GeV/u, large Doppler effects are involved in the $\gamma$-ray detection. Therefore, the performance of the RISING array was investigated by means of Monte Carlo simulations. The simulations revealed the dependence between chosen target thickness, beam velocity, and the resulting $\gamma$-ray detector response. Furthermore, it was proved that the lifetime of an excited state cannot be neglected in the determination of the de-excitation $\gamma$-ray energies.

In the experiment new $\gamma$-ray decays were found in the neutron deficient $^{36}$Ca and $^{36}$K. For the $2^+_1 \rightarrow 0^+_{g.s.}$ decay in $^{36}$Ca an excitation energy of 3015(16) keV was found. The comparison with the corresponding excitation energy in $^{36}$S yielded a mirror energy difference for the $2^+_1 \rightarrow 0^+_{g.s.}$ decay of $\Delta E_M = -276(16)$ keV.

In order to understand the large $\Delta E_M$ value, shell model calculations have been performed using isospin symmetric USD based interactions and the experimental proton and neutron SPE energies from the the $A = 17$, $T = 1/2$ mirror nuclei. The result of these calculations showed that the extremely large mirror energy difference is reproduced using these experimental SPE, which account empirically for the one-body part of Thomas-Ehrman and/or Coulomb effects. The results are consistent with a monopole driven shell structure scenario and the expectation that Ca isotopes below $N = 16$ develop another “island of inversion”. Furthermore, shell model calculations were performed for all $I^\pi = 2^+_1$ states of the $T = 1$ and $T = 2$ mirror nuclei in the *sd* shell. To be consistent with the experimental mirror energy differences, ad hoc corrections to the experimental SPE were required. They resulted in a reduction of the proton gap $\Delta_\pi$ in $^{22}$O and of the neutron gap $\Delta_\nu$ in $^{34}$Ca relative to the corresponding gaps in the mirror nuclei, making the mirror energy difference $\Delta E_M$ a useful probe for shell structure investigations in experimentally inaccessible regions.

In future in-beam $\gamma$-ray spectroscopy experiments employing the two-step fragmentation technique at relativistic energies the particle identification after the secondary target needs to be improved. This can be achieved by implementing a time-of-flight measurement and by using Si strip detectors as is proposed for the LYCCA [117] array. A large progress in the $\gamma$-ray detection at relativistic energies is expected from the AGATA array [116]. This $4\pi$ $\gamma$-spectrometer will consist of 180 36-fold segmented Ge crystals. A $\gamma$-ray detection efficiency of $\varepsilon_{peak}$ = 50 % and an energy resolution of better than 0.5 % are expected from the AGATA array for $E_{\gamma 0}$ = 1 MeV $\gamma$-rays emitted at 100 MeV/u. This has to be compared with an efficiency of $\varepsilon_{peak}$ = 6 % and an energy resolution of 2.5 % for the combined Cluster and MINIBALL detectors used in the RISING array. The AGATA array will therefore allow for nuclear structures studies of exotic nuclei that are presently beyond reach.

# A $\gamma$-Ray Efficiency and Energy Resolution of the RISING Setup at 150 and 200 $A$ MeV

The $\gamma$-ray efficiency and the energy resolution of the RISING Fast Beam setup is also simulated for heavy ion energies of 150 and 200 $A$ MeV while varying the $\gamma$-ray energies between 250 and 3000 keV. The results are shown in the following figures.

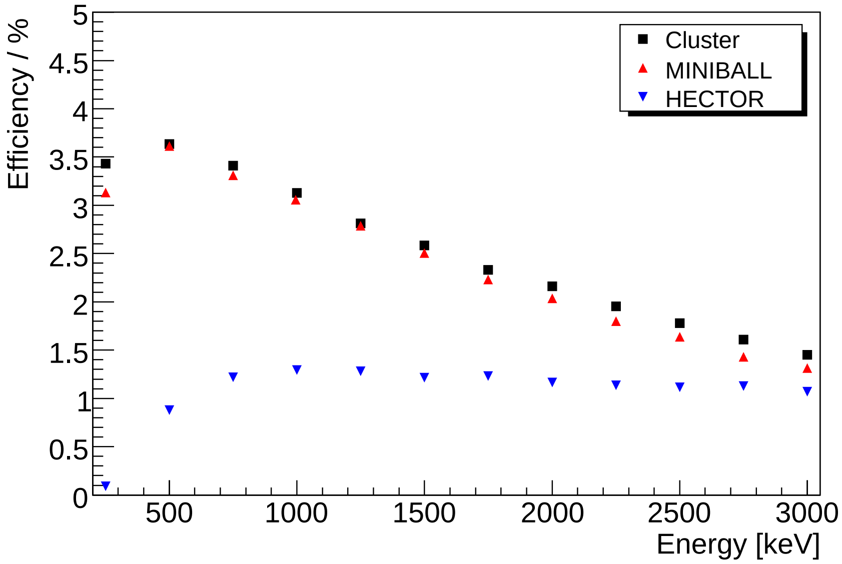

**Figure A.1:** Simulated $\gamma$-ray efficiency $\varepsilon_{peak}$ at a beam energy of 150 $A$ MeV for the three RISING $\gamma$-ray detector systems.

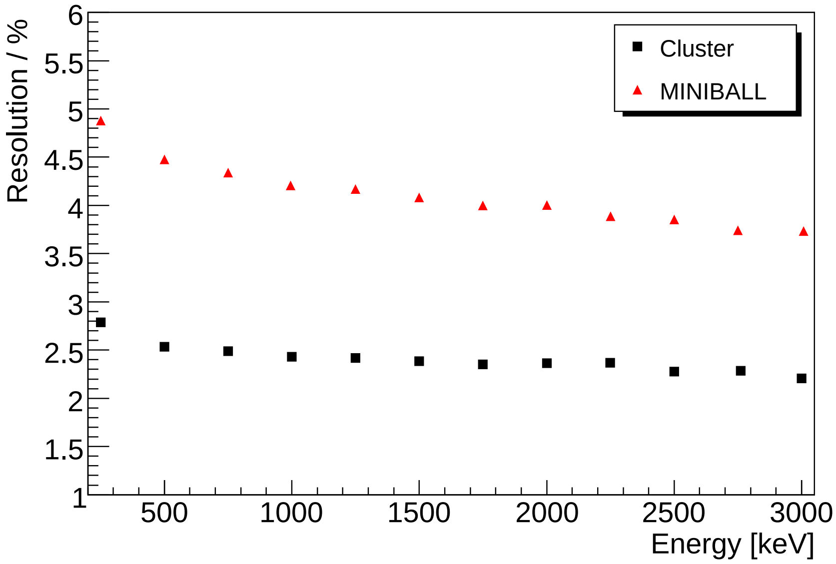

**Figure A.2:** Simulated energy resolution at a beam energy of 150 *A* MeV for the RISING Ge detector systems.

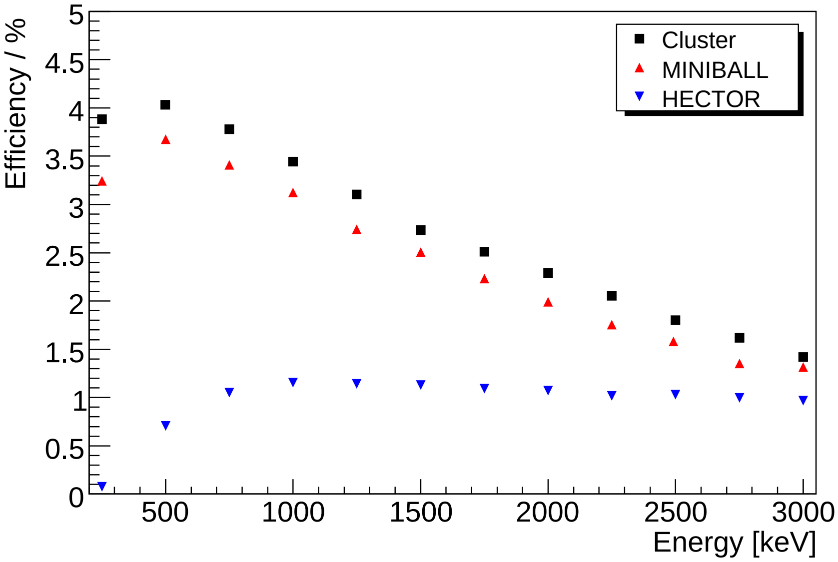

**Figure A.3:** Simulated $\gamma$-ray efficiency $\varepsilon_{peak}$ at a beam energy of 200 *A* MeV for the three RISING $\gamma$-ray detector systems.

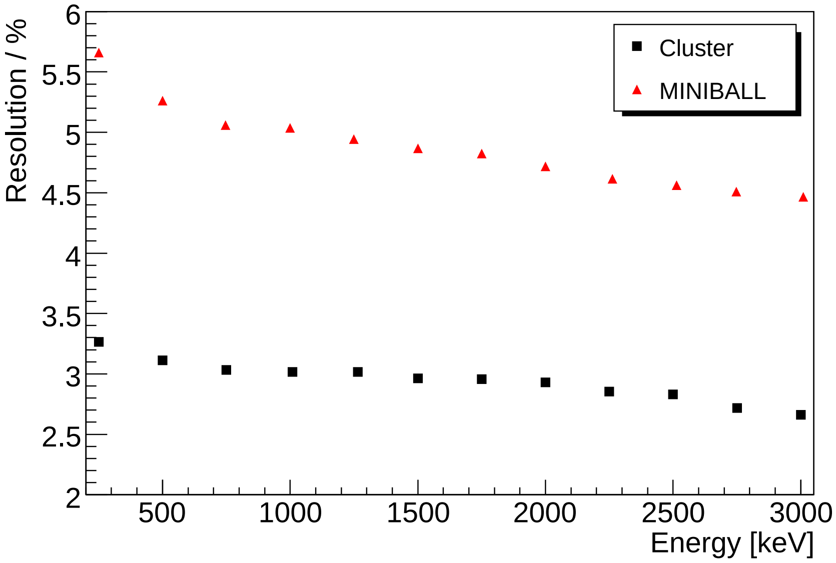

**Figure A.4:** Simulated energy resolution at a beam energy of 200 *A* MeV for the RISING Ge detector systems.

# B Simulations of the RISING $\gamma$-Ray Efficiency in the Stopped Beam Configuration

Alternatively to impinging heavy ions on a secondary target when they reach the final focal plane of the FRS they can also be implanted into a stopper. Thereby, the $\gamma$-ray decays of isomeric states produced in the primary target can be studied. If an active stopper is used, $\gamma$-rays can also be related to the $\beta$-decay of exotic nuclei. Naturally, the RISING setup has to be optimised for these experiments. As there are no Doppler effects to be considered the sole goal is to achieve the highest possible $\gamma$-ray efficiency without losing the high granularity of the 15 Cluster detectors. This is necessary to minimise the loss of $\gamma$-ray efficiency due to the "prompt flash" caused by atomic radiation and nuclear reactions [118]. Therefore, the Cluster detectors are positioned in three rings at angles of $51^\circ$, $90^\circ$, and $129^\circ$ at distances of only 20 cm for the ring at $90^\circ$ and 22 cm for the other two rings from the centre of the stopper. This configuration is drawn schematically in Fig. B.1.

Also for this setup $\gamma$-ray detection efficiency simulations are performed. Here, only the efficiency values for a point-like source sitting in the centre of the stopper are given and losses due to the stopper thickness are neglected. The simulations have, however, the option to chose between different stopper materials and thicknesses and to change the implantation position, spatial width, and depth. It is also possible to place other absorber materials as Pb, Sn, and Al front of the Cluster detectors, but this option is not used for the efficiency simulations shown in Fig. B.2. To have a good possibility of comparison with a measured efficiency, the simulations are made for energies of often used calibration sources as $^{60}$Co, $^{137}$Cs, $^{152}$Eu, and $^{133}$Ba. In addition, energies of 2000, 2500, and 3000 keV are simulated. For the add-back only intra-crystal events are accepted and, as only one $\gamma$-ray energy is simulated at a time, the Cluster multiplicity is required to be equal to

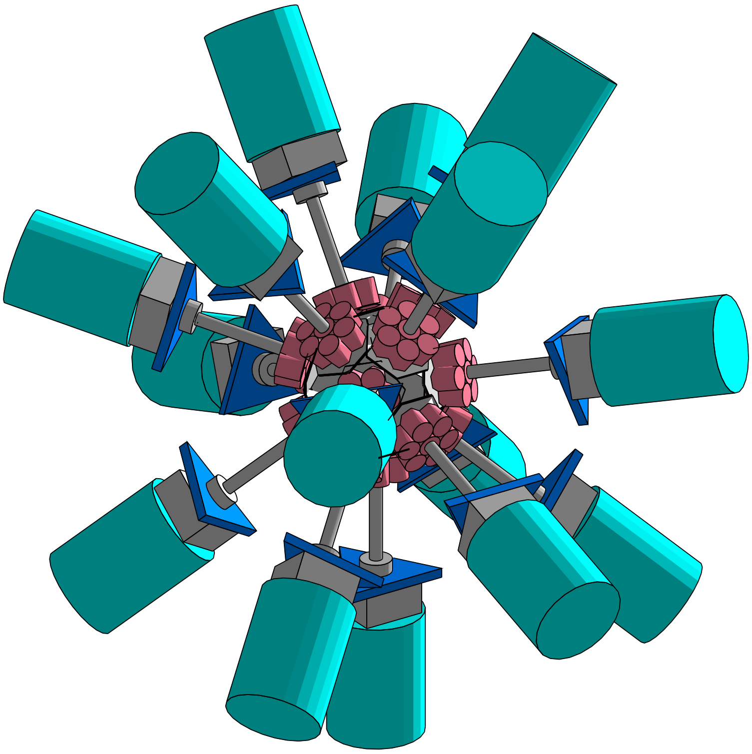

**Figure B.1:** Schematic layout of the RISING Stopped Beam setup. The detectors are positioned in three rings at distances between 20 and 22 cm from the centre of the stopper.

one. Furthermore, for simplicity, the energy resolution is set to be 2.5 keV for a $\gamma$-ray of 1332.5 keV and scaled linearly.

The efficiency simulations yields a value of 11% for singles hit events at an energy of 1332.5 keV. Including the add-back case an efficiency of 16.7% is obtained. As the detectors are packed very densely, one can also investigate how often the $\gamma$-rays scattered between different Clusters. This is shown together with the multiplicity of the individual crystals in Fig. B.3. It is observed that if the $\gamma$-ray is detected in more than one crystal, it scatters mostly within the same detector. Therefore, add-back procedures that take into account these events have a high impact on the efficiency, while only few events are gained from events that scattered between two Cluster detectors.

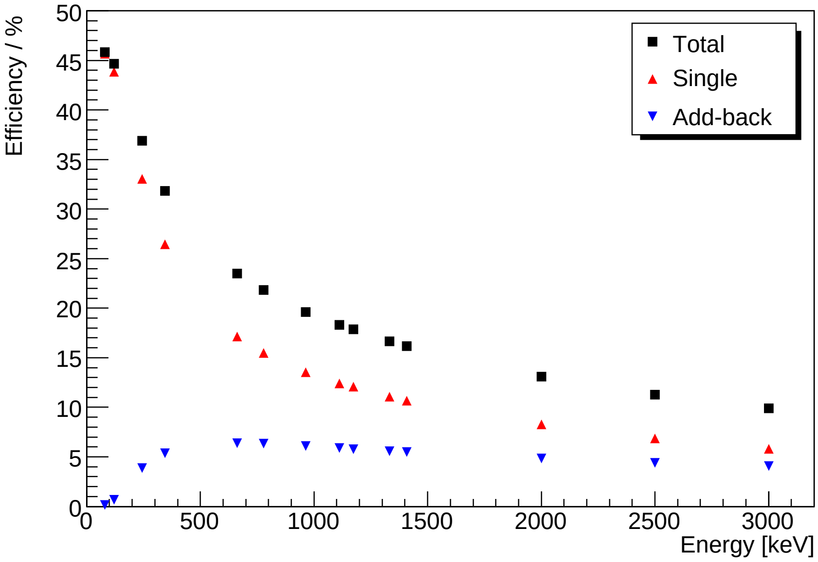

**Figure B.2:** Simulated $\gamma$-ray efficiency $\varepsilon_{peak}$ of the RISING Stopped Beam setup at $\gamma$-ray energies between 80 and 3000 keV. The total efficiency is the sum of the add-back and singles efficiency.

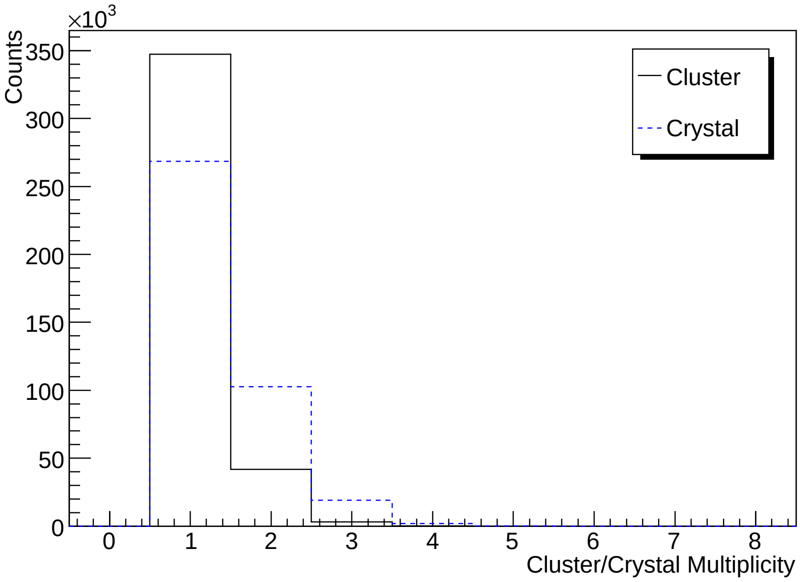

**Figure B.3:** Simulated crystal and Cluster multiplicity of the RISING Stopped Beam setup for a $\gamma$-ray of 1332.5 keV.

# Bibliography

[1] A. Bohr and B.R. Mottelson, Nuclear Structure Vol. 1: Single-Particle Motion, World Scientific Publishing Co. Pte. Ltd. (1998).

[2] T. Glasmacher, Ann. Rev. Nucl. Part. Sci. 48 (1998) 1.

[3] F. Azaiez, AIP Conf. Proc. 481 (1998) 243.

[4] H. Wollersheim *et al.*, Nucl. Instr. Meth. A 537 (2005) 357.

[5] H. Geissel *et al.*, Nucl. Instr. Meth. B 70 (1992) 286.

[6] R. Lozeva *et al.*, Nucl. Instr. Meth. A 562 (2006) 298.

[7] M.G. Mayer, Phys. Rev. 74 (1948) 235.

[8] E. Feenberg, Phys. Rev. 75 (1949) 320.

[9] O. Haxel, J.H.D. Jensen and H.E. Suess, Phys. Rev. 75 (1949) 1766.

[10] M.G. Mayer, Phys. Rev. 75 (1949) 1969.

[11] M.G. Mayer, Phys. Rev. 78 (1950) 22.

[12] M.G. Mayer and J.H.D. Jensen, Elementary Theory of Nuclear Shell Structure, Wiley, New York (1955) 58.

[13] S. Hofmann and G. Münzenberg, Rev. Mod. Phys. 72 (2000) 733.

[14] H. Grawe and M. Lewitowicz, Nucl. Phys. A 693 (2001) 116.

[15] Evaluated Nuclear Structure Data File,
`http://www.nndc.bnl.gov/ensdf/`.

[16] Z. Elekes *et al.*, Phys. Rev. C 73 (2006) 044314.

[17] W. Greiner and J. Maruhn, Kernmodelle, Verlag Harri Deutsch, Frankfurt am Main (1995).

[18] V.F. Weisskopf, Phys. Rev. 83 (1951) 1073.

[19] R. Hofstadter, Ann. Rev. Nucl. Sci. 7 (1957) 231.

[20] R.D. Woods and D.S. Saxon, Phys. Rev. 95 (1954) 577.

[21] B.A. Brown, Prog. Part. Nucl. Phys. 47 (2001) 517.

[22] T. Otsuka *et al.*, Prog. Part. Nucl. Phys. 47 (2001) 319.

[23] J.Sinatkas *et al.*, J. Phys. G 18 (1992) 1377 and 1401.

[24] P. Möller, J.R. Nix, K.-L. Kratz, At. Data Nucl. Data Tab. 66 (1997) 131.

[25] K.A. Brückner, Phys. Rev. 97 (1995) 1353.

[26] M. Hjorth-Jensen, T.T.S. Kuo, and E. Osnes, Phys. Rep. 261 (1995) 125.

[27] B.H. Wildenthal, Prog. Part. Nucl. Phys. 11 (1984) 5.

[28] E.K. Warburton, J.A. Becker, and B.A. Brown, Phys. Rev. C 41 (1990) 1147.

[29] D. Guillemaud-Mueller *et al.*, Nucl. Phys. A 426 (1984).

[30] T. Motobayashi *et al.*, Phys. Lett. B 346 (1995) 9.

[31] B.V. Pritychenko *et al.*, Phys. Lett. B 461 (199) 322.

[32] V. Chisté *et al.*, Phys. Lett. B 514 (2001) 233.

[33] M. Belleguic *et al.*, Nucl. Phys. A 682 (2001) 163c.

[34] P.G. Thirolf *et al.*, Phys. Lett. B 485 (2000) 16.

[35] M. Stanoiu *et al.*, Phys. Rev. C 69 (2004) 034312.

[36] Y. Utsuno *et al.*, Phys. Rev. C 60 (1999) 054315.

[37] A. Poves and A. Zuker, Phys. Rep. 70 (1981) 235.

[38] T. Otsuka *et al.*, Phys. Rev. Lett. 87 (2001) 082502.

[39] A. Poves and J. Retamosa, Phys. Lett. B 184 (1987) 311.

[40] A. Poves and J. Retamosa, Nucl. Phys. A 571 (1994) 221.

[41] E. Caurier *et al.*, Phys. Rev. C 58 (1998) 2033.

[42] E. Caurier *et al.*, Nucl. Phys. A 693 (2001) 374.

[43] H. Grawe *et al.*, Eur. Phys. J. A 25 (2005) 357.

[44] H. Grawe, Act. Phys. Pol. B 34 (2003) 2267.

[45] `http://www-inj.gsi.de/`.

[46] `http://www.gsi.de/beschleuniger/sis18/sis.html`.

[47] A.S. Goldhaber, Phys. Lett. B 53 (1974) 306.

[48] J.J. Gaimard and K.H. Schmidt, Nucl. Phys. A 531 (1991) 709.

[49] D.J. Morrissey, Phys. Rev. C 39 (1989) 460.

[50] W.A. Friedman, Phys. Rev. C 27 (1983) 569.

[51] O. Tarasov, Nucl. Phys. A 734 (2004) 536.

[52] V. Borrel *et al.*, Z. Phys. A 314 (1983) 191.

[53] F. Rami *et al.*, Nucl. Phys. A (1985) 349.

[54] K. Sümmerer *et al.*, Phys. Rev. C 42 (1990) 2546.

[55] K. Sümmerer and B. Blank, Phys. Rev. C 61 (2000) 034607.

[56] H. Folger *et al.*, Nucl. Instr. Meth. A 303 (1991) 24.

[57] O. Tarasov and D. Bazin, Nucl. Phys. Meth. B 204 (2003) 174.

[58] `http://www-linux.gsi.de/~weick/mocadi/`.

[59] H. Stelzer, Nucl. Instr. Meth. A 310 (1991) 103.

[60] R. Schneider and A. Stolz, Technical Manual Ionisation Chamber MUSIC80 (2000).

[61] `http://www-linux.gsi.de/~weick/atima/`.

[62] G. Knoll, Radiation Detection and Measurement, John Wiley & Sons Inc., New York (1979).

[63] R. Lozeva, PhD Thesis, University of Sofia, Bulgaria (2005).

[64] D.J. Morrissey *et al.*, Nucl. Instr. Meth. B 204 (2003) 90.

[65] R. Anne and A.C. Mueller, Nucl. Instr. Meth. B 70 (1992) 276.

[66] T. Kubo *et al.*, Nucl. Instr. Meth. B 70 (1992) 309.

[67] J. Eberth *et al.*, Nucl. Instr. Meth. A 369 (1996) 135.

[68] J. Eberth *et al.*, Progr. Part. Nucl. Phys. 46 (2001) 389.

[69] A. Maj *et al.*, Nucl. Phys. A 571 (1994) 185.

[70] F. Camera, Ph.D. Thesis, University of Milano, Italy (1992).

[71] D. Pelte and D. Schwalm, In-beam Gamma-Ray Spectroscopy with Heavy Ions, North-Holland, Amsterdam, 1982.

[72] D. Schwalm *et al.*, Nucl. Phys. A 192 (1972) 449.

[73] J. Simpson Z. Phys. A 358 (1997) 139.

[74] W. Korten and S. Lunardi, Achievements with the Euroball spectrometer 1997 – 2003 (2003).

[75] M. Wilhelm *et al.*, Nucl. Instr. Meth. A 381 (1996) 462.

[76] I. Lazarus *et al.*, IEEE Trans. on Nucl. Sci. 39 (1992) 1352.

[77] X-Ray Instrumentation Associates (XIA), `http://www.nndc.bnl.gov/ensdf/`.

[78] M. Lauer, Ph.D. Thesis, University of Heidelberg, Germany (2004).

[79] C. Gund, Ph.D. Thesis, University of Heidelberg, Germany (2000).

[80] L. Palafox Gámir, Ph.D. Thesis, University of Heidelberg, Germany (1997).

[81] `http://root.cern.ch/`.

[82] S. Agostinelli *et al.*, Nucl. Instr. Meth. A 506 (2003) 250.

[83] K. Sümmerer *et al.*, Nucl. Phys. Meth. B 204 (2003) 278.

[84] H.G. Essel *et al.*, IEEE Trans. Nucl. Sci. NS-43 (1996) 132.

[85] H.G. Essel and N. Kurz, IEEE Trans. Nucl. Sci. NS-47 (2000) 337.

[86] J. Hofmann and N. Kurz, GSI Scientific Report (2002) 224.

[87] I. Lazarus, Overview of the Euroball Trigger System (1994), `http://npg.dl.ac.uk/documents/edoc333/edoc333.pdf`.

[88] J. Hofmann, N. Kurz, and M. Richter, VME Trigger Module.

[89] `http://www-w2k.gsi.de/go4/`.

[90] J. Grębosz, Comp. Phys. Com. 176 (2007) 251.

[91] A. Banu, PhD Thesis, University of Mainz, Germany (2005).

[92] S.M. Lenzi *et al.*, Phys. Rev. Lett. 87 (2001) 122501.

[93] A. Gadea *et al.*, Phys. Rev. Lett. 97 (2006) 152501.

[94] J. Vernotte *et al.*, Phys. Rev. C 13 (1976) 461.

[95] H. Schatz *et al.*, Phys. Rev. Lett. 79 (1997) 3845.

[96] P.D. Cottle *et al.*, Phys. Rev. Lett. 88 (2002) 172502.

[97] S. Kanno *et al.*, Progr. Theor. Phys. (Kyoto), Suppl. 146 (2002) 575.

[98] K. Yoneda *et al.*, Phys. Rev. C 74 (2006) 021303(R).

[99] B.H. Wildenthal *et al.*, Phys. Rev. C 4 (1971) 1266.

[100] H. Herndl *et al.*, Phys. Rev. C 52 (1995) 1078.

[101] R. Gross, A. Frenkel, Nucl. Phys. A 267 (1976) 85.

[102] B.A. Brown, A. Etchegoyen, W.D.M. Rae, Computer Code OXBASH, MSU-NSCL Report 524 (1988) and Report 1289 (2004).

[103] B.A. Brown and B.H. Wildenthal, Ann. Rev. of Nucl. Part. Sci. 38 (1988) 29.

[104] R.G. Thomas, Phys. Rev. 88 (1952) 1109.

[105] J.B. Ehrman, Phys. Rev. 81 (1951) 412.

[106] D.W. Devins *et al.*, Phys. Rev. C 24 (1981) 59.

[107] M. Matoba *et al.*, Phys. Rev. C 48 (1993) 95.

[108] D. Guillemaud-Mueller *et al.*, Phys. Rev. C 41 (1990) 937.

[109] M. Fauerbach *et al.*, Phys. Rev. C 53 (1996) 647.

[110] N. Iwasa *et al.*, Phys. Rev. C 65 (2003) 064315.

[111] H. Grawe, Springer Lect. Notes in Phys. 651 (2004) 33.

[112] A. Gade *et al.*, Phys. Rev. C 76 (2007), in print.

[113] A. Gade *et al.*, Phys. Rev. Lett. 93 (2004) 042501.

[114] T.G Dzubay *et al.*, Phys. Lett. B 33 (1970) 302.

[115] W. Trinder *et al.*, Nucl. Phys. A 620 (1997) 191.

[116] J. Gerl and W. Korten, Technical Proposal for an Advanced Gamma Tracking Array for the European Gamma Spectroscopy Community (2001).

[117] `http://wwwnsg.nuclear.lu.se/lycca/`.

[118] Zs. Podolyák *et al.*, Nucl. Phys. A 722 (2003) 273.

# Danksagung

An dieser Stelle habe ich endlich die Gelegenheit, denjenigen zu danken, die zum Gelingen dieser Arbeit beigetragen haben. Herzlich gedankt sei vor allem Herrn Prof. Dr. P. Reiter für die Vergabe des Themas, seine engagierte Betreuung und sein stetes Interesse am Fortgang der Arbeit. Bei Herrn Prof. Dr. J. Jolie bedanke ich mich für die Übernahme des Zweitgutachtens. Ein ganz besonderer Dank geht an Herrn Dr. H. Grawe für seine Hilfe und Erläuterungen bei so vielen physikalischen Problemen.

Für die Betreuung an der GSI bedanke ich mich bei Herrn Dr. J. Gerl und Herrn Priv. Doz. Dr. H.-J. Wollersheim, die mir in vielen anregenden Diskussionen neue Einblicke in das Arbeitsthema ermöglichten. Außerdem möchte ich ihnen für ihre Unterstützung beim Planen und Durchführen eines Coulomb-Anregungsexperiments danken. Bei den derzeitigen und ehemaligen Mitgliedern der lokalen RISING-Gruppe bedanke ich mich für das angenehme Arbeitsklima und ihre ständige Hilfsbereitschaft.

Bei allen Mitgliedern der RISING-Kollaboration bedanke ich mich für das Gelingen des Fragmentationsexperiments. Vor allem den Zuständigen für den mechanischen Aufbau des Experiments, den Herren Dipl.-Phys. I. Kojouharov und Dipl.-Ing. W. Prokopowicz, und für die Datenaufnahme, den Herren Dr. N. Kurz und Dipl.-Ing. H. Schaffner, sei an dieser Stelle gedankt. Darüber hinaus bedanke ich mich bei Frau Dr. M. Górska, Herrn Dr. Zs. Podolyák, Herrn Dr. F. Becker, Frau Dr. N. Saito und Frau Dipl.-Phys. L. Caceres für die gute Zusammenarbeit bei den Einstellungen des Fragment-Separators.

Herrn Dr. T. Saito danke ich für die Erläuterungen der GEANT-Simulationen und für viele fachliche Gespräche. Meinem Zimmergenossen, Herrn Dr. P. Bednarczyk, danke ich für das Erzeugen einer angenehmen Arbeitsatmosphäre durch die Schreibtischumstellung und die zahlreichen interessanten Unterhaltungen.

Nicht zuletzt geht ein großer Dank an meine Eltern und meine Freundin Marie, die durch ihre stete Unterstützung mir das Arbeiten sehr erleichtert haben.

# Erklärung

Ich versichere, dass ich die von mir vorgelegte Dissertation selbständig angefertigt, die benutzten Quellen und Hilfsmittel vollständig angegeben und die Stellen der Arbeit – einschließlich Tabellen, Karten und Abbildungen –, die anderen Werken im Wortlaut oder dem Sinn nach entnommen sind, in jedem Einzelfall als Entlehnung kenntlich gemacht habe; dass diese Dissertation keiner anderen Fakulät oder Universität zur Prüfung vorgelegen hat; dass sie – abgesehen von unten angegebenen Teilpublikationen – noch nicht veröffentlicht ist, sowie dass ich eine solche Veröffentlichung vor Abschluss des Promotionsverfahrens nicht vornehmen werde. Die Bestimmungen der Promotionsordnung sind mir bekannt. Die von mir vorgelegte Dissertation ist von Prof. Dr. Peter Reiter betreut worden. Nachfolgend genannte Teilpublikationen liegen vor:

P. Doornenbal, P. Reiter, H. Grawe, T. Otsuka, A. Al-Khatib, A. Banu, T. Beck, F. Becker, P. Bednarczyk, G. Benzoni, A. Bracco, A. Bürger, L. Caceres, F. Camera, S. Chmel, F.C.L. Crespi, H. Geissel, J. Gerl, M. Górska, J. Grebosz, H. Hübel, M. Kavatsyuk, O. Kavatsyuk, M. Kmiecik, I. Kojouharov, N. Kurz, R. Lozeva, A. Maj, S. Mandal, W. Meczynski, B. Million, Zs. Podolyak, A. Richard, N. Saito, T. Saito, H. Schaffner, M. Seidlitz, T. Striepling, Y. Utsuno, J. Walker, N. Warr, H. Weick, O. Wieland, M. Winkler, H.J. Wollersheim
The $T = 2$ mirrors $^{36}$Ca and $^{36}$S: A test for isospin symmetry of shell gaps at the driplines
Phys. Lett. B 647, 237 (2007)